Stress in thin films and coatings: Current status, challenges, and prospects

Grégory Abadias, Eric Chason, Eric Keckes, Marco Sebastiani, Gregory Thompson, Etienne Barthel, Gary Doll, Conal Murray, Chris Stoessel, Ludvik Martinu

Stress in thin films and coatings: Current status, challenges and prospects

G. Abadias[1*], E. Chason[2], J. Keckes[3], M. Sebastiani[4], G.B. Thompson[5]

E. Barthel[6], G.L. Doll[7], C.E. Murray[8], C.H. Stoessel[9], L. Martinu[10]

[1] *Institut Pprime, Département de Physique et Mécanique des Matériaux, UPR 3346, CNRS-Université de Poitiers-ENSMA, SP2MI, Téléport 2, F86962 Futuroscope-Chasseneuil, France*
E-mail : gregory.abadias@univ-poitiers.fr

[2] *School of Engineering, Brown University, Providence, Rhode Island 02912-9104, USA*
E-mail: eric_chason_phd@brown.edu

[3] *Department of Materials Physics, Montanuniversität Leoben and Erich Schmid Institute for Materials Science, Austrian Academy of Sciences, Leoben, Austria*
E-mail: jozef.keckes@gmail.com

[4] *University of Rome "ROMA TRE", Engineering Department, Via della Vasca Navale 79, Rome, Italy, E-Mail: marco.sebastiani@uniroma3.it*

[5] *Department of Metallurgical & Materials Engineering, The University of Alabama, PO Box 870202, Tuscaloosa, Alabama 35487-0202, USA*
E-mail: gthompson@eng.ua.edu

[6]*Laboratoire Sciences et Ingénierie de la Matière Molle, PSL Research University, ESPCI Paris, CNRS, et Sorbonne Universités, UPMC Univ Paris 06, F-75231 Paris Cedex 05, France, E-mail: etienne.barthel@espci.fr*

[7]*Mechanical Engineering Department, The University of Akron, Akron OH, 44325-0406*
E-mail: gd27@uakron.edu

[8]*IBM T.J. Watson Research Center, Yorktown Heights, NY 10598*
E-mail: conal@us.ibm.com

[9]*Eastman Chemical Co., 3788 Fabian Way, Palo Alto, CA94303, USA*
E-mail: cstoessel@eastman.com

[10]*Department of Engineering Physics, Polytechnique Montréal, Montreal, QC, Canada,*
E-mail: ludvik.martinu@polymtl.ca

* Corresponding author

Abstract

The issue of stress in thin films and functional coatings is a persistent problem in materials science and technology that has congregated many efforts, both from experimental and fundamental points of view, to get a better understanding on how to deal with, how to tailor and how to manage stress in many areas of applications. With miniaturization of device components, the quest for increasingly complex film architectures and multi-phase systems, and the continuous demands for enhanced performance, there is a need towards the reliable assessment of stress on a sub-micron scale from spatially-resolved techniques. Also, the stress evolution during film and coating synthesis using physical vapor deposition (PVD), chemical vapor deposition (CVD), plasma enhanced chemical vapor deposition (PECVD) and related processes is the result of many interrelated factors and competing stress sources, so that the task to provide a unified picture and a comprehensive model from the vast amount of stress data remains very challenging.

This article summarizes the recent advances, challenges and prospects of both fundamental and applied aspects of stress in thin films and engineering coatings and systems, based on recent achievements presented during the 2016 Stress Workshop entitled "Stress Evolution in Thin Films and Coatings: from Fundamental Understanding to Control". Evaluation methods, implying either wafer curvature, X-ray diffraction (XRD) or focused ion beam (FIB) removal techniques, are reviewed. Selected examples of stress evolution in elemental and alloyed systems, graded layers and multilayer-stacks, as well as amorphous films deposited using a variety of PVD and PECVD techniques are highlighted. Based on mechanisms uncovered from *in situ* and real-time diagnostics, a kinetic model is outlined that is capable of reproducing the dependence of intrinsic (growth) stress on grain size, growth rate and deposited energy. The problems and solutions related to stress in the context of optical coatings, inorganic coatings on plastic substrates, and tribological coatings for aerospace applications, are critically examined.

This review also suggests strategies to mitigate excessive stress levels from novel coating synthesis perspectives to microstructural design approaches, including the ability to empower crack-based fabrication processes, pathways leading to stress relaxation and compensation, as well as management of the film and coating growth conditions with respect to energetic ion bombardment. Future opportunities and challenges for stress engineering and stress modelling are considered and outlined.

Table of content

I. Introduction

The presence of stress in thin films and functional coatings constitutes a major concern in many technological applications as excessive residual stress levels can dramatically affect the performance, reliability and durability of material components and devices. Worst case scenarios lead to film cracking for layers subjected to tensile stress[1,2] or peeling off, buckling or blistering in the case of compressive stress.[3–6] Residual stress distributions can significantly impact the adhesion and the fracture toughness of thin films,[7–9] the ductility of bulk metallic glasses (BMG),[10] the performance of optoelectronic and aerospace components,[11] the thermo-mechanical behavior of stacks in Through Silicon Vias (TSV) 3D integrated devices,[12] the resonant frequency and lifetime of micro- and nano-electro-mechanical systems (MEMS and NEMS),[13] or cause the emergence of hillocks and whiskers in metal interconnects at the origin of short circuit failures,[14–17] to cite a few examples. Alternately, stress (or strain) can have beneficial influence on the physical properties of thin layers and nanostructures, e.g. conductivity,[18] dielectric permittivity,[19] piezoelectricity, magnetic anisotropy and magneto-elastic coupling,[20,21] or enhancement in charge carrier mobility in silicon-based semiconductor technology.[22] Therefore, there is significant motivation to understand the origin of stress in thin films as they can directly affect the design, processing and lifetime of advanced materials and components. Various research strategies to tailor and control the stress state are currently devised in diverse applications ranging from micro/optoelectronic devices, MEMS/NEMS (thermal sensors and actuators), optical components (lenses, mirrors, filters, etc..) to protective and functional coatings intended to impart thermal, mechanical, tribological, environmental, electrical, magnetic or biological functions. From a technological point of view, this has generated an intense research and innovation activity over the last decades related to the measurement of residual stresses, more recently including the determination of

intrinsic (growth) stress due to thin film deposition conditions, which has gained interest thanks to the potential offered by *in situ* and real-time diagnostics.[23]

Regardless of the technique of film preparation (physical or chemical vapor deposition (PVD/CVD), electrochemical deposition, etc) thin films can develop large intrinsic stresses in the course of their growth process. For many materials, the stress magnitude in thin layer forms and nanostructures can typically exceed the tensile strength of their respective bulk counterpart.[24,25] Indeed, the density of defects that are frozen into a film during deposition can be two orders of magnitude higher than that produced by the severest cold-work treatment of a bulk material.[26]

The concern about stress dates back over a century ago with the observation by Gore that "the inner and outer surfaces of electrodeposits were in unequal states of cohesive tension", causing the plate on which they were deposited to bend.[27] This led Stoney[28], some years later, to derive a relationship between the film stress and the amount of substrate bending, which can be readily quantified from the measurement of the substrate curvature, or equivalently, its deflection. Since the pioneer work of Stoney in the early 1900s, considerable work has been done, especially after 1960s with the achievement of high vacuum conditions during the PVD processes,[29–32] enabling one to separate the various parameters of film growth that influence the intrinsic film stress while minimizing the influence of impurity content due to chemical reactivity with residual gas components. Despite that many trends have been identified, in particular the common stress behaviors depending on material mobility,[33–37] the stress development during thin film growth exhibits complex dependences with respect to the growth rate, temperature, film microstructure and morphology, so that a complete and unifying picture of our understanding of stress has not yet been achieved. The situation gets even more intricate in the case of multicomponent systems, where alloying effects such as solute atom segregation[38,39] or phase transformation[40,41] may come into play. Deposition

processes in which the temporal and energetic profiles in terms of energy and fluxes of specific species (such as ions) can be manipulated[42–45] are opening new avenues for stress tailoring. This explains why stress is a hot topic amongst the materials science and engineering community, calling for more systematic testing grounds as well as new achievements gained from multiscale stress modeling.

From a more practical point of view, the reliable assessment of residual stresses on a micron, or sub-micron, scale is a strategic challenge for the robust design and reliability of a wide range of micro- and nano-systems. Protective thin films and coatings often possess complex gradients of phases, microstructure and residual stresses, which result from (i) intentionally varying deposition conditions, (ii) self-organization phenomena like competitive grain growth, diffusion along GBs and/or on the surface, (iii) post-deposition mechanical and thermal loads caused, for example, by friction between coating and machined surface, and (iv) the effect of the surrounding environment leading to gas or vapor sorption. Those gradients decisively influence the functional properties of thin films and coatings, such as hardness, toughness, oxidation resistance, wear behavior, adhesion and durability. Therefore, in order to optimize the functional properties, it is necessary to assess the depth variation of residual stresses with respect to the microstructure with nanoscale resolution. The evolution of the average in-plane stress can be measured by wafer curvature techniques during deposition, providing information on the stress profile throughout the film thickness.23 In recent years, several high-resolution residual stress measurement techniques have been implemented, such as micro-focus synchrotron X-ray diffraction (XRD),[46] holographic transmission electron microscopy (TEM),[47] micro-Raman spectroscopy,[48] and electron backscattered diffraction (EBSD)[49]. Unfortunately, most of these methods have limitations in terms of instrument accessibility, applicability to amorphous (or strongly textured) materials, perfect lattice rectification and to non-homogeneous stress states. Nonetheless, the measurement of residual

stress in sub-micron volumes is still a challenging task, especially in the case of strongly textured, complex multiphase, nano-crystalline or amorphous materials and films.

This article, which gathers contributions from several leading groups working in the field, encompasses a critical viewpoint on to-date state of knowledge on stress in thin films and coatings. It gives a non-exhaustive overview and a snapshot on the progress of *both* fundamental and applied research deployed in this field, based on recent outcomes presented during the Stress Workshop entitled "Stress Evolution in Thin Films and Coatings: from Fundamental Understanding to Control", that was jointly organized by the Advanced Surface Engineering Division (ASED) of the American Vacuum Society (AVS) and the Society of Vacuum Coaters (SVC), in Chicago, in October 2016. It is mostly focused on polycrystalline thin films, so that the issue of strained surfaces and nanostructures, as well as epitaxial layers, will not be discussed here. The reader interested in such aspects is referred to the articles/monographs of Koch50, Ibach51, Brovko et al.52 and Fluri et al.[53] Similarly, for more extensive reviews of this work, particularly on the proposed stress models, it is advisable to go through the recent tutorial of Chason and Guduru.[23] Still, stress in amorphous thin films represents an important part of technological interests especially in relation to optical coatings and thin films on plastics.[11,54–56]

The present paper is divided into several parts. Sections II and III are dedicated to the fundamental aspects of how thin film stress can be measured and interpreted. In Section II, we outline the evaluation methods for stress determination, including wafer curvature, XRD and focused ion beam (FIB)-based techniques. Section III describes recent experimental findings on stress evolution during thin film growth and their understanding based on a kinetic model, recently extended to account for energetic particle bombardment during deposition (Sec. III-A). Selected examples are also provided to highlight chemical alloying effects and phase transformation (Sec. III-B), as well as the interplay between stress gradient and texture

development (Sec. III-C). Section IV addresses the ways how to deal with, how to tailor and manage stress in specific areas of applications. These include the methods and approaches to assess and control stress in microfabricated systems such as microelectronic components (Section IV-A), or issues related to the effect of deposition processes and film growth conditions in the context of most frequent amorphous and polycrystalline optical coatings (OC) and optical interference filters (OIF), as well as strategies to mitigate excessive stress by both experimental and design approaches (Section IV-B). Section IV-C gives an overview of problems and solutions related to stress in the context of inorganic coatings on plastic substrates, including polymer webs and injection molded components, while Section IV-D describes case studies related to stress build up and stress compensation approaches in the context of protective coatings for aeronautical, aerospace and related manufacturing components. Complementary stress engineering strategies, based on interfacial and alloying design or pulse management in sputtering processes, are proposed in Section IV-E, followed by an overview of the present status of understanding and interpreting the formation of cracks and their propagation in relation to stress (Section IV-F). Finally, Section V summarizes the still open question related to stress, and it suggests pathways and outlooks for future developments.

II. Evaluation methods for stress determination

A. A nondestructive method: wafer curvature

An important method for measuring stress in thin films is wafer curvature. The principle behind the method is to measure the curvature induced in the substrate due to stress in the film. Because it is non-destructive and can be used in real-time, it has been one of the workhouse techniques for quantifying stress in thin films.[23,33,57,58] In this section, we describe how the curvature is related to the film stress and make clear some underlying assumptions used in interpreting the measurements.

We will also discuss some methods that have been developed for measuring stress using wafer curvature.

The well-known Stoney equation relates the average stress in the film ($\bar{\sigma}$) to the measured curvature (κ)[59]:

$$\kappa = \frac{6\bar{\sigma} h_f}{M_s h_s^2} \qquad (1).$$

The values M_s and h_s refer to the biaxial modulus and thickness of the substrate, respectively. The product $\bar{\sigma} h_f$ is termed the stress-thickness and has units of force/length; note that the average stress cannot be determined from the curvature without knowing the film thickness. The average stress in the Stoney equation is assumed to be equi-biaxial and laterally uniform. This ignores, for instance, that in polycrystalline films the stress may be different at/near the grain boundaries (GBs) than in the middle of the grain[23,60] or that in patterned films (such as metallic interconnect lines) the stress may be non-uniform over the surface[61].

Even assuming that the stress is laterally uniform, it may still vary through the thickness of the film. Then the thickness-averaged stress can be computed by integrating the in-plane stress at height z from the substrate ($\sigma_{xx}(z)$) over the film thickness (h_f):

$$\bar{\sigma} = \frac{1}{h_f}\int_0^{h_f} \sigma_{xx}(z)dz \qquad (2).$$

In this discussion, we are ignoring the presence of any surface or interfacial stresses that may also contribute to the curvature.[62–64] Because of the thickness averaging, a single curvature measurement does not provide any information about the depth-dependence of the stress in the film. The curvature from a film with a non-uniform stress through the thickness is equivalent to a film of the same thickness with a uniform stress of the average value. A film that induces no curvature in the substrate may in fact have a large stress gradient in it. The lack of curvature only tells us that the tensile and compressive stresses integrated over the thickness are equal. Since large stress gradients

may lead to cracking even though the nominal stress appears to be small, it is important to know the distribution of stress throughout the film's thickness.

The depth-dependence of the stress can be explored by measuring the evolution of the stress-thickness as the film is deposited. The time derivative of the stress-thickness is given by:

$$\frac{d(\bar{\sigma}h)}{dt} = \sigma_{xx}(h)\frac{dh}{dt} + \int_0^h \frac{\partial \sigma_{xx}(z)}{\partial t} dz \qquad (3),$$

where h is the thickness at time t. The first term on the right corresponds to the effect of adding new layers to the surface with a stress of $\sigma_{xx}(h)$; this is sometimes referred to as the *incremental* or *instantaneous* stress. The second term corresponds to a change in the stress of the layers that have already been deposited.

If we can assume that the stress does not change after deposition (i.e., the time derivative in the second term in Eq. (3) is zero), then the stress at each height in the film is the same as when it was deposited. In that case, the incremental stress can be determined from the derivative of the stress-thickness with thickness:

$$\sigma_{xx}(h) = \frac{\frac{d(\bar{\sigma}h)}{dt}}{\frac{dh}{dt}} = \frac{d(\bar{\sigma}h)}{dh} \qquad (4).$$

To illustrate how this works, a schematic representation of a film of thickness h_f with a distribution of in-plane stress is given in Figure 1a. The arrows represent the stress at different heights in the film. The arrows pointing away from the film correspond to tensile stress and those pointing toward the film correspond to compressive stress. The corresponding evolution of the curvature during deposition is shown in Figure 1b as a function of thickness with the value h_f shown by the vertical dotted line. The average film stress at this thickness is determined by dividing the measured curvature by the thickness, represented by the line between the measured value and the

origin. The incremental stress at this thickness is represented by the slope of the stress-thickness at this point, represented by the tangent line on the curve. Note that at this thickness the average stress is positive (tensile) while the incremental stress is negative (compressive). The data are taken from stress-thickness measurements during electron beam evaporation of polycrystalline Ag on SiO_2.[65]

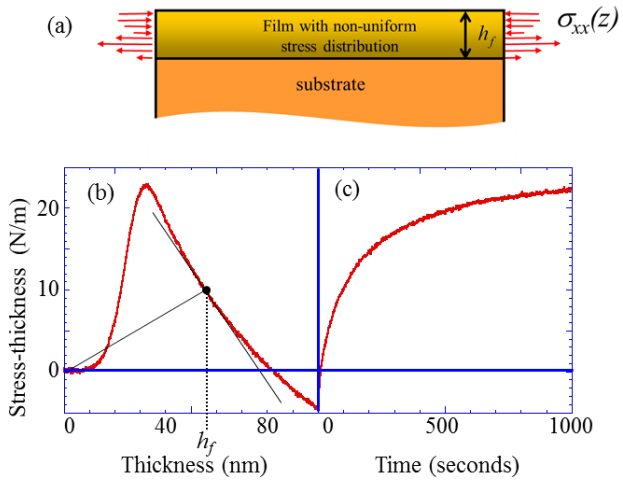

Figure 1: a) Schematic showing the distribution of stress throughout the thickness of a film on a substrate. b) Evolution of stress-thickness during electron-beam deposition of Ag on SiO_2. The slope of the line from the origin to the solid circle at h_f is proportional to the average stress. The slope of the tangent line is proportional to the incremental stress. c) Evolution of the stress-thickness when the deposition is terminated.

Recall that in equating the incremental stress with the slope of the stress-thickness, we assumed that the stress in the deposited layers does not change. The effect of the stress changing in the deposited layers can be seen when the growth is stopped at a thickness of 100 nm indicated by the vertical line (Figure 1c). Since there is no more growth, the thickness of the film does not change after this point. However, it is clear that the stress-thickness relaxes significantly. As discussed below, this may be due to various stress-induced processes like diffusion of atoms out of the grain boundary (GB), thermal expansion mismatch or grain growth in the film.

Multiple techniques have been developed for measuring the wafer curvature. Some methods monitor the change in shape of the cantilever by capacitance[66–68], microbalance,[69] dilatometry or interferometry.[70] Others monitor the deflection of light beams reflected from the cantilever surface.

Some monitor a single reflected beam[71] or the spacing between multiple beams reflected from the surface.[23,72,73] A benefit of the multi-beam reflection method is that it reduces the sensitivity to sample vibration because the curvature is determined from the change in spacing between the reflected beams. Vibration of the sample may change the direction of the reflected beams, but it changes them all by the same amount so that the relative spacing between the beams does not change. Multiple-beam optical stress sensor (MOSS) is therefore useful for *in situ* measurements in growth chambers where vacuum pumps may induce a large amount of mechanical vibration, as well as in liquid media, such as during electrochemical deposition,[74,75] where convection (natural or forced) may induce perturbations.

B. X-ray diffraction techniques

1. Conventional laboratory XRD

Conventional laboratory XRD analysis performed in reflection geometry is routinely used to characterize average residual stresses and stress gradients in thin films, coatings and near-surface regions.[76–80] Residual stress is determined from the measurement of X-ray elastic strains, ε, and applying a constitutive equation in the form of a generalized Hooke's law, which requires the knowledge of the elastic properties of the film.[79] The common procedure employs the so-called '$\sin^2\psi$ method', based on the determination of a set of lattice spacings d_{ψ}^{hkl} using Bragg's law from the measured Bragg's angle positions θ_{ψ}^{hkl} of *hkl* reflections at various sample tilt angles ψ and azimuth angles ϕ, whereby ψ represents the angle between the diffraction vector $\boldsymbol{Q}$ and the sample normal $\boldsymbol{z}$, and ϕ is the rotation angle around $\boldsymbol{z}$. In many situations, polycrystalline films exhibit a preferred crystallite orientation of rotational symmetry around the substrate normal, referred to as a fiber texture, so that it is sufficient to measure the strain solely as a function of the tilt angle ψ. In the absence of shear stress components ($\sigma_{ij}=0$ for $i\neq j$), and assuming an equi-biaxial in-plane stress state ($\sigma_{11}= \sigma_{22}=\sigma_{\parallel}$),

the quantity $\sigma_{\parallel}$ can be readily extracted from the slope of d_{ψ}^{hkl} versus $\sin^2\psi$ curve, according to the fundamental equation of x-ray residual stress analysis

$$\varepsilon_{\psi}^{hkl} = \frac{d_{\psi}^{hkl} - d_0}{d_0} = 2S_1^{hkl}\sigma_{\parallel} + \frac{1}{2}S_2^{hkl}\sigma_{\parallel}\sin^2\psi \qquad (5)$$

where S_1^{hkl} and $\frac{1}{2}S_2^{\mathrm{hkl}}$ refer to the x-ray elastic constants (XECs), and d_0 is the unstrained lattice parameter. XEC quantities are introduced in the formalism to account for the elastic anisotropy of crystalline materials. For randomly textured materials, they are independent of ψ (and ϕ) and can be calculated for each *hkl* reflection from the single crystal elastic compliances s_{ij} using a grain interaction model.[77,79,81] Indeed, in a diffraction experiment, only a given subset of crystallites contribute to the measured intensity, so that a micromechanical model relating the strain (or stress) inside these crystallites to the macroscopic average stress to which the whole specimen is subjected, is required. The most common approximations are the Reuss (all crystallites are subjected to the same stress),[82] Voigt (all crystallites exhibit the same strain),[83] and Neerfeld-Hill limits,[84,85] the last being the arithmetic mean of the Reuss and Voigt estimates.[77] Note that for isotropic materials, the XECs reduce to the mechanical elastic constants, S_1^{mech} and S_2^{mech}, defined as $S_1^{\mathrm{mech}} = -\frac{\nu}{E}$ and $\frac{1}{2}S_2^{\mathrm{mech}} = \frac{1+\nu}{E}$, where E and ν are the Young's modulus and Poisson ratio of the deposit, respectively.

The value of the unstrained lattice parameter d_0 can be obtained from the strain-free direction ψ^*, derived by stating $\varepsilon_{\psi^*}^{hkl} = 0$ from the fundamental Eq. (5), which yields $\sin\psi^* = \sqrt{\frac{2\nu}{1+\nu}}$ for the case of isotropic materials under an equi-biaxial stress state. In practice, when the elastic constants of the deposit material are unknown (which is rather often the case for multicomponent alloys or complex compounds), the strain-free lattice parameter may be obtained from the intersection point of d_{hkl} vs. $\sin^2\psi$ lines obtained for the same deposit under different stress states.[86,87]

However, it is important to note that the lattice spacing d_{ψ}^{hkl} represents an *average* quantity, which depends on the actual stress depth gradient, $\sigma(z)$, X-ray penetration depth, τ, chemical gradients influencing $d_{o}^{hkl}(z)$ and XRD experiment geometry. In practice, different approaches can be implemented depending on the laboratory diffraction equipment. On a two-circle diffractometer, a simple procedure consists in measuring a series of 2θ scans around a single *hkl* reflection at varying incident beam angles ω. In this asymmetric geometry, known as the Ω mode[79,88], the angle ψ is given by $\psi = \omega - \theta$. A second option is to use a glancing angle scan (at fixed ω) and determine the d_{ψ}^{hkl} lattice spacing of various *hkl* reflections which correspond to different ψ values. This approach is well suited for thick polycrystalline coatings with random orientation of the crystallites, allowing for the selection of *hkl* reflections at high 2θ values with appreciable intensity, contributing to a higher accuracy in the measurement of d_{ψ}^{hkl} values (misalignment issues of the diffractometer are minimized at high scattering angle). However, for thin films, Bragg reflections at high scattering angles are most often hardly measurable.[79] A third option, for researchers having a four-circle diffractometer, is to measure a series of symmetric θ–2θ scans at various inclination ψ angles of the sample holder around the diffractometer axis (known as χ mode[79,88], or side-inclination method[76]), allowing for a change in the angle ψ independently of the detector rotation. This geometry is the same as the one used for pole figure measurements, and has one great virtue that the accessible tilt angle range is much larger than in the Ω mode (for which $|\psi| < \theta$), starting from ψ=0° to almost ψ=90°. Moreover, the penetration depth remains nearly constant for a wide range of tilt angles (up to ψ~30-40°).

One should keep in mind, however, that the analysis outlined above is only valid for polycrystalline thin films/coatings having a random orientation of grains. Thin films/coatings produced by PVD/CVD techniques rarely belong to this category, as they most often exhibit a

crystallographic texture related to their specific columnar growth morphology, so that they can no longer be treated as macroscopically elastically isotropic specimens. In this case, the stress analysis is more complex, and one has to use the concept of x-ray stress factors to relate stress and strain.[79] Also, the available ψ directions which yield sufficient diffracted intensity are often restricted to small angular ranges near the intensity poles. However, rather simple expressions can still be derived for the most common fiber textures, <100>, <110>, <111> and <112>, when considering crystals with cubic symmetry.[79,89] The plots of the strain ε_{ψ}^{hkl} in the distinct poles versus $\sin^2\psi$ do not generally fall on a straight line, even for a biaxial stress state. The only exceptions are reflections of the type *h00* and *hhh*, as well as the <111> texture.

Another approach is offered for the case of thin films with strong and sharp texture (as also found in epitaxial layers or cold-rolled materials), known as the crystallite group method.[88,90] This method was introduced in 1982 by Willemse *et al*.,[91] and then adapted by Baron and Hauk to fiber-textured coatings.[92] It is based on considering the highly textured film with a crystallographic growth texture along a given <*uvw*> direction as a single crystal aligned along this corresponding ideal orientation, and measuring the lattice spacings of various *hkl* planes in the same set of grains belonging to this <*uvw*> ideal orientation (crystallite group), at specific angles ψ corresponding to the intensity poles. General expressions of the elastic strain ε_{ψ}^{hkl} vs. $\sin^2\psi$ have been reported by Clemens and Bain[90] for materials with cubic symmetry and for equal or non-equal biaxial stress states. This methodology is a special case of the $\sin^2\psi$ technique discussed above; it differs by the fact that the texture in the film is explicitly taken into account rather than using XECs or stress factors to describe geometrical distributions of crystallites in the polycrystalline aggregate. Kim *et al*.[93] have employed a similar procedure to determine the biaxial stress state in sputter-deposited AlCu films with a (111) preferred orientation.

In addition to anisotropy issues in textured thin films, another possible cause for deviation from linearity of d_{ψ}^{hkl} vs. $\sin^2\psi$ plots is the presence of stress gradients along the film thickness, especially when the film thickness is on the same order as the penetration depth τ at ψ=0°.[89] Different concepts and methods have been proposed to determine the residual stress gradient $\sigma(z)$ along the surface normal ***z*** in equibiaxially stressed polycrystalline thin films and coatings.[79,89,94,95] Neglecting the chemical gradients, the measured X-ray elastic strain can be expressed as:

$$\varepsilon_{\psi}^{hkl}(\tau)=\frac{d_{\psi}^{hkl}(\tau)-d_{o}^{hkl}}{d_{o}^{hkl}}=\frac{1}{d_{o}^{hkl}}\frac{\int_{0}^{\xi} d_{\psi}^{hkl}(z)\ \exp(-z/\tau)\ \mathrm{d}z}{\int_{0}^{\xi}\exp(-z/\tau)\ \mathrm{d}z} \qquad (6),$$

where ξ is the thin film depth and $d_{\psi}^{hkl}(z)$ is the depth-dependent measured lattice spacing. By varying the experiment geometry, e.g., by changing the angle ψ, it is possible to determine X-ray elastic strains $\varepsilon_{\psi}^{hkl}(\tau)$ for various X-ray penetration depths τ. This information is then used to calculate the unknown residual stress depth profile $\sigma(z)$, defined in the real space as a function of *z*, by fitting its supposed usually polynomial dependence to the experimental $\varepsilon_{\psi}^{hkl}(\tau)$ dependence (Eq. (6)), expressed in the so-called Laplace space, by applying X-ray elastic constants.[94] Since there are, however, infinitely many $\sigma(z)$ dependencies, which can be fitted to the measured $\varepsilon_{\psi}^{hkl}(\tau)$ dependence, the inverse Laplace space approach can be used to evaluate residual stress gradients $\sigma(z)$ only in simplified cases like shot-peened samples with linear and/or monotonic $\sigma(z)$ dependencies. An illustration will be given in Sect. IV.A for stress gradients in capped layers. In many other cases, $\sigma(z)$ dependencies can be very complex, like stepwise or oscillatory, and can be even combined with the presence of chemical gradients in the sample, smearing the measured d_{ψ}^{hkl} values. Therefore, there is a

need to develop novel characterization approaches, which can be used to assess nanoscale $\sigma(z)$ dependencies in graded thin films and coatings.

2. Cross-sectional nanodiffraction using synchrotron facilities

In 2012, a novel experimental approach to characterize nanoscale depth variation of residual stresses and microstructure in thin films and coatings was introduced.[96] Cross-sectional X-ray nanodiffraction is based on the application of synchrotron point (or pencil) X-ray nanobeams with a diameter (or thickness) down to 50 nm or even less to scan thin films at the cross-section in transmission (or reflection) diffraction geometries (Figure 2).[97]

Up to now, cross-sectional X-ray nanodiffraction experiments were performed at beamlines ID11 and ID13 of European Synchrotron Radiation Facility in Grenoble and at the beamline P03 of Petra III synchrotron source in Hamburg using monochromatic beams of energy E = 12-30 keV.[80,98] For the nanobeam focusing, Fresnel zone plates, nanofocusing parabolic refractive X-ray lens and multilayer Laue lenses were used. For the experiments, a thin lamella consisting of thin film or coating on the substrate with a thickness e (in the beam direction) in the range of ~10-250 μm is usually prepared using the FIB technique. It is important that the beam is aligned parallel to the substrate surface or to the interfaces between individual sublayers in the lamella by using the φ rotation axis (Figure 2). The diffraction data from the sample are collected using a charge-coupled device (CCD) area detector positioned behind the sample using a sample–detector distance of ~80-130 mm. In order to obtain diffraction data from different sample cross-sectional regions, the lamella is moved along the sample normal $\boldsymbol{z}$ with a step of the beam size or smaller. For each lamella position, two-dimensional (2D) diffraction data are collected using CCD. The diffraction data are then processed in order to obtain information about the position, shape and nature of Debye-Scherrer rings collected by the detector, *e.g.*, using a Fit2D or similar software packages.

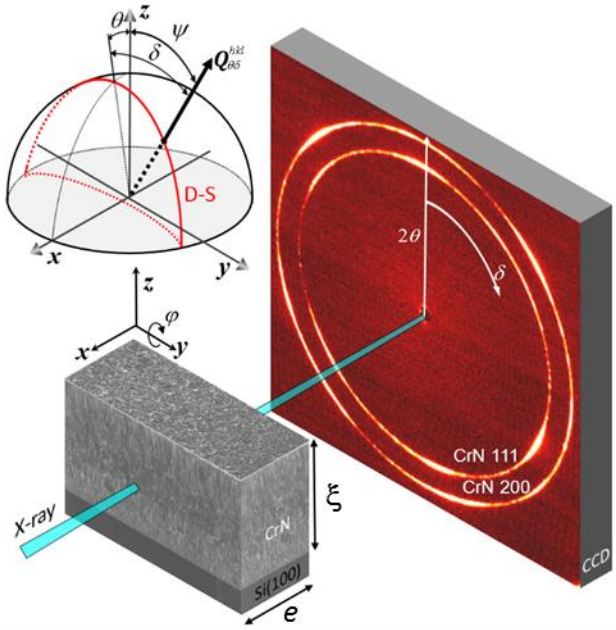

Figure 2: A schematic view of position-resolved X-ray nanodiffraction experiment carried out in transmission diffraction geometry on CrN coating with a thickness ξ deposited on Si(100) substrate prepared as lamella with a thickness *e*. The sample is moved along the *z* axis with a step of the X-ray beam size, and the diffraction data are collected using a CCD detector. The beam is aligned parallel to the interface using the φ axis movement. A CrN *hkl* Debye–Scherrer ring represents diffraction from CrN crystallites for which the diffraction vectors $\boldsymbol{Q}_{\theta\delta}^{hkl}$ are located on a bold line representing schematically Debye-Scherrer (D-S) ring depicted in the stereographic projection in the top left. The orientation of the diffraction vector can be specified by angles θ, ψ and δ. Reprinted with permission from Scripta Mater. 67, 748 (2012). Copyright 2012 Elsevier.

Every *hkl* Debye-Scherrer ring azimuthal position δ represents diffraction on (*hkl*) crystallographic planes oriented with their normal vector $\boldsymbol{n}_{hkl}$ parallel to the diffraction vector $\boldsymbol{Q}_{\theta\delta}^{hkl}(z)$ (Figure 2). Therefore, Debye-Scherrer rings collected using the 2D detector at the thin film depth *z* can be used to evaluate the lattice spacing $d_{\theta\delta}^{hkl}(z)$ as a function of the ring azimuthal angle δ using Bragg's law by analyzing Bragg's angle $2\theta_{\delta}^{hkl}(z)$ azimuthal dependencies on the detector. Depending on the diffraction statistics, usually 36 values of $d_{\theta\delta}^{hkl}(z)$ can be determined for 36 azimuthal angle δ sections called azimuthal cakes. Every $d_{\theta\delta}^{hkl}(z)$ value represents an X-ray probe volume-averaged lattice parameter for the diffraction

vector $\boldsymbol{Q}_{\theta\delta}^{hkl}(z)$ orientation defined by the angles δ and θ in Figure 2. For every $d_{\theta\delta}^{hkl}(z)$, X-ray elastic strain at the thin film depth *z* can be determined as follows:

$$\varepsilon_{\theta\delta}^{hkl}(z)=\frac{d_{\theta\delta}^{hkl}(z)-d_o^{hkl}}{d_o^{hkl}} \tag{7}.$$

The measured strain $\varepsilon_{\theta\delta}^{hkl}(z)$ can be expressed as a function of unknown strain components $\varepsilon_{ij}^{hkl}(z)$ defined in the sample coordinate system with axes *x, y* and *z* from Figure 2 as follows:

$$\begin{aligned}\varepsilon_{\theta\delta}^{hkl}(z)=&\sin^2\theta\,\varepsilon_{11}^{hkl}(z)+\cos^2\theta\,\sin^2\delta\,\varepsilon_{22}^{hkl}(z)+\cos^2\theta\,\cos^2\delta\,\varepsilon_{33}^{hkl}(z)\\&-\sin 2\theta\,\cos\delta\,\varepsilon_{31}^{hkl}(z)+\cos^2\theta\,\sin 2\delta\,\varepsilon_{32}^{hkl}(z)-\sin 2\theta\sin\delta\,\varepsilon_{12}^{hkl}(z)\end{aligned} \tag{8}.$$

By considering thin film X-ray elastic constants $\frac{1}{2}S_2^{hkl}(z)$ and $S_1^{hkl}(z)$, which depend on single crystal elastic constants, crystallographic texture, *hkl* reflection and grain interaction mechanism, it is possible to write X-ray diffraction Hooke's law as:

$$\begin{aligned}\varepsilon_{\theta\delta}^{hkl}(z)=&S_1^{hkl}(z)\left[\sigma_{11}(z)+\sigma_{22}(z)+\sigma_{33}(z)\right]\\&+\tfrac{1}{2}S_2^{hkl}(z)\left[\sin^2\theta\,\sigma_{11}(z)+\cos^2\theta\sin^2\delta\sigma_{22}(z)+\cos^2\theta\cos^2\delta\,\sigma_{33}(z)\right]\\&+\tfrac{1}{2}S_2^{hkl}(z)\left[-\sin 2\theta\cos\delta\,\sigma_{31}(z)+\sin 2\delta\cos^2\theta\,\sigma_{32}(z)-\sin 2\theta\sin\delta\,\sigma_{12}(z)\right]\end{aligned} \tag{9},$$

where $\sigma_{ij}(z)$ represents unknown stress components defined in the sample coordinate system. Usually, the stress state in thin films is equi-biaxial with $\sigma_{11}(z)=\sigma_{22}(z)=\sigma(z)$, and the out-of-plane stress component as well as shear stress components can be neglected with $\sigma_{33}(z)\cong 0$ and $\sigma_{ij}(z)\cong 0$. Consequently, Eq. (9) can be simplified:

$$\varepsilon_{\theta\delta}^{hkl}(z)=2\;\sigma(z)\;S_1^{hkl}(z)+\sigma(z)\;\tfrac{1}{2}S_2^{hkl}(z)\left[\sin^2\theta+\cos^2\theta\sin^2\delta\right] \tag{10}.$$

Since for small Bragg's angles θ the term $\sin^2\theta$ and $\cos^2\theta$ in Eq. (10) goes to zero and one, respectively, Eqs. (6) and (10) can be rewritten as:

$$\frac{\partial d_{\theta\delta}^{hkl}(z)}{\partial \sin^2\delta} \cong \sigma(z)\ \tfrac{1}{2} S_2^{hkl}(z)\ d_o^{hkl}(z) \qquad (11).$$

It means that for every *hkl* Debye-Scherer ring and the corresponding $d_{\theta\delta}^{hkl}(z)$ dependence, the in-plane residual stress is proportional to the Debye-Scherer ring ellipticity quantitatively expressed through $\partial d_{\theta\delta}^{hkl}(z)/\partial \sin^2\delta$.

In practical cases, $d_{\theta\delta}^{hkl}(z)$ values are evaluated for 36 azimuthal positions δ of the *hkl* Debye-Scherer rings, which are then plotted as a function of $\sin^2\delta$. The slope of the $d_{\theta\delta}^{hkl}(z)$ versus $\sin^2\delta$ dependence is proportional to the magnitude of the in-plane stress $\sigma(z)$ (Eq. (11)). An important advantage of this approach is that the unstressed lattice parameter $d_o^{hkl}(z)$ has to be determined only approximately.

In the case of thin lamella with the lamella thickness *e* comparable to or even smaller than thin film or coating thickness ξ (Figure 2), the lamella preparation results in the relaxation of the stress component $\sigma_{11}(z)$, which influences the measured $\varepsilon_{\theta\delta}^{hkl}(z)$ as well as the evaluated stress $\sigma(z)$. In that case, it is necessary to perform a finite element (FE) modeling of the stress state in the thin lamellae in order to recalculate the stress state in the unstressed sample as extensively discussed elsewhere.[97] In majority of cases, it is possible to prepare a lamellae with $e >> \xi$, and the FE analysis is not required.

Another advantage of cross-sectional X-ray nanodiffraction is the fact that besides the possibility to evaluate residual stress gradients, also thin film and coating depth gradients of phases and microstructure (including texture and crystallite size) can be determined directly in real space as a function of the coating depth *z*. This can be done by evaluating and comparing individual Debye-Scherrer rings collected at different depths (Figure 2). The approach opens

the possibility to analyze residual stress gradients in graded thin films with chemical gradients and correlate them with depth gradients of texture, crystallite sizes and phases.

C. FIB-based methods

1. **Method description and validation**

In recent years, the development of FIB scanning electron microscopy (SEM) and Digital Image Correlation (DIC) created new possibilities for the downscaling to the sub-micron scale of material removal residual stress measurement techniques (e.g., hole drilling, ring-core and slitting methods).[99]

The novel FIB techniques involve a combination of FIB milling, SEM imaging, DIC analysis, and FE modelling.[100–116] The method consists of incremental FIB milling, by using several possible milling geometries, combined with *in situ* high-resolution field emission gun SEM imaging of the relaxing surface, and a full field strain analysis by DIC. The through-thickness profile of the residual stress can also be obtained by comparing the experimentally measured surface strain with FE and/or analytical constitutive modeling.

FIB-DIC procedures have recently been established as the one method capable of achieving sub-micron spatial resolution for the residual stress analysis in amorphous materials, coatings and thin nanostructured layers.[100–116] Kang and co-workers[100] first proposed the downscaling of the slitting method measuring the stress release caused by milling of a slot on a thin diamond-like-carbon (DLC) film deposited on a glass substrate. Several other milling relaxation geometries have been proposed in the literature, including hole-drilling,[101] ring-core,[102–105] H-bar (also called double slot)[110], and four-slot geometries.[112]

The ring-core geometry has recently received particular attention because of its main advantages of highest spatial resolution (< 1 μm), the possibility of full 2D strain and stress mapping, and the fact that complete stress relaxation is achieved if the trench depth *h* is higher

than the central stub's diameter (d_m), thus allowing for direct use of the Hooke's law to calculate the average residual stress from the measured strain relief. Additionally, the use of a ring (or pillar) milling geometry could even be used to measure the fracture toughness of the film, by using the nanoindentation pillar splitting method, which involves sharp nanoindentation over the pillar to induce fracture of the material at a certain critical load that can be correlated to the fracture toughness, by knowing the pillar's radius. Since this section is focused on the use of the ring-core geometry to measure residual stress, we refer to previous papers for more details of the possible use of the same geometry to measure fracture toughness.[117,118]

In Figure 3, a schematic representing the main steps of the method and examples of the possible typical dimensions of the core are reported. More details on SEM imaging strategies and DIC procedures are reported elsewhere.[113]

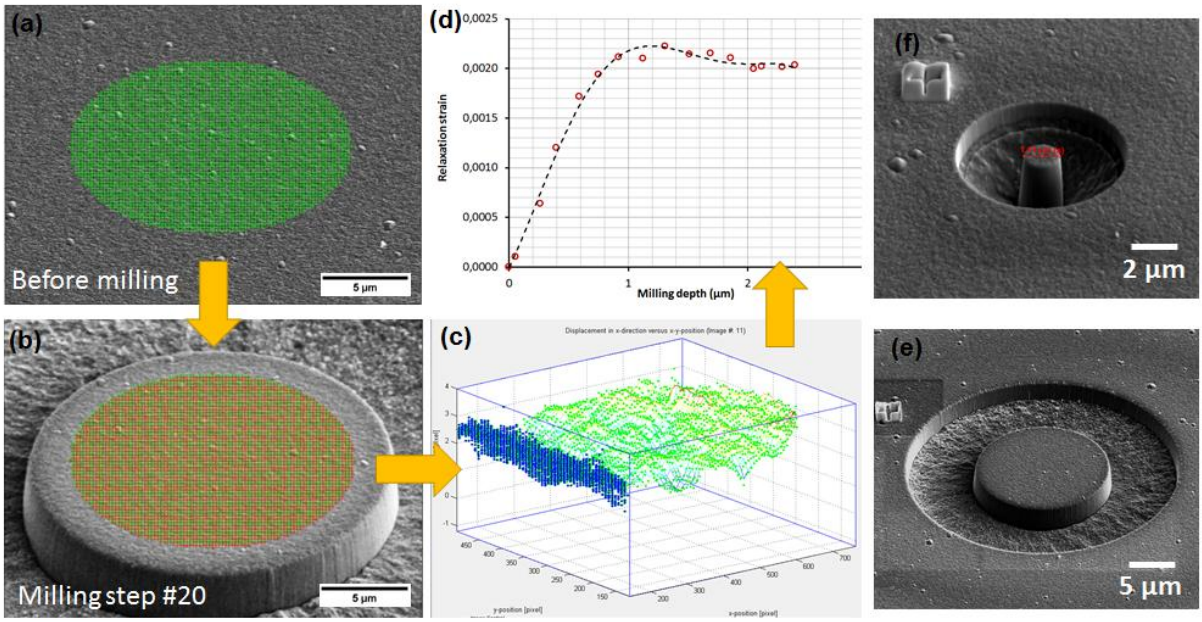

Figure 3: Schematic representation of the FIB-DIC method (ring-core) for residual stress assessment at the micro scale. (a) SEM image acquired before FIB milling and definition of a grid of markers, (b) FIB incremental milling and acquisition of one (or more) SEM images after each milling step, (c) DIC to map relaxation strain and (d) extraction of the relaxation strain as a function of milling depth. In (e-f), the typical size of the milled trench can vary between 1 and 20 µm.

Significant activities in terms of validation of the method have recently been performed, including comparisons with other standard measurement techniques. In particular, the procedure has been validated against conventional XRD ($\sin^2\psi$), curvature (Stoney's equation) and micro-Raman methods. In a recent paper,[111] a critical comparison between the XRD-$\sin^2\psi$ and the FIB-DIC methods has been performed on a fully characterized CrN coating grown by cathodic arc deposition (CAD). While a very good agreement is found between the two measurements, the observed differences have been critically discussed. In particular, the uncertainty on the elastic modulus of the coating, which is needed for stress calculation in both cases, can be the primary explanation for the observed differences. Additionally, the presence of a texture in the film can be a source of stress calculation errors in both cases, since it may affect both the linearity of the stress vs $\sin^2\psi$ fit and the relaxation strain distribution after FIB milling. The presence of a stress depth profile can also be considered as a possible source of discrepancy between the two approaches, since this is not considered in the most conventional XRD-$\sin^2\psi$ method. In relation to this latter point, another main source of discrepancy could be the different probing volumes between the two techniques, which is usually equal to the entire film thickness in the case of FIB-DIC, while it is a function of the beam energy and angle of incidence in the case of XRD methods.

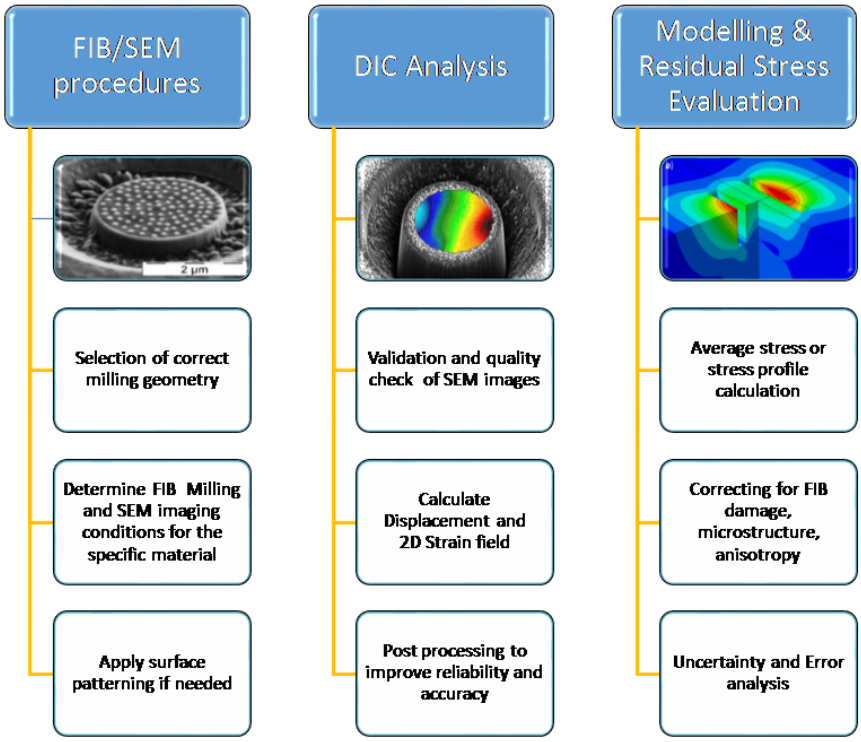

Figure 4: Synthetic description of the main experimental and modeling issues related to FIB-DIC residual stress measurement techniques.

2. Choice of the proper FIB milling geometry

The choice of an appropriate milling geometry allows for a quantitative and detailed evaluation of the full in-plane stress tensor, the depth profile of residual stress with sub-micrometer resolution, the stresses inside single grains with different crystal orientation, or even the Poisson's ratio of the material.

The selected geometry should be in compliance with the material's requirements and the object of the measurement. From this point of view, the method offers multiple possibilities that may be used for gaining more comprehensive information about the residual stress distribution over the sample surface and in-depth. Table 1 reports a series of suggestions regarding selection of the milling geometry for different applications.

Table 1: A summary with practical recommendations on the correct choice of the best milling geometry for different applications.

Milling geometry	Characteristics	Suggested application
Single-slot	Higher displacement, for a given stress, over a large area. Strong strain gradient from the edge. Possibility of stress depth profiling.	Best choice in case of very thin films and stress profiling on them.
Double-slot	Uniform strain (linear displacement) in the area between the two slots. Fast and simple analysis. Information only from one direction. Good choice for homogeneous coatings with equal-biaxial stress	Homogeneous coatings with a thickness range 1-10 µm, where equal-biaxial stress is expected.
Hole drilling	Strong strain gradient from the edge. Possibility of stress depth profiling.	Good option for depth profiling, since it is a very well established procedure (from macro-scale).
Ring-core	Highest spatial resolution (< 1 µm). Full 2D stress analysis. Possibility of stress depth profiling. It is the one geometry that gives surface full stress relaxation: analytical calculation of stress is possible for $h/d_m > 1$.	Coatings with a thickness range 0.2-20 µm. Best choice for residual stress mapping over heterogeneous and/or multi-phase materials. Analysis on thicker films (> 20 µm) by cross-section profiles. Possibility of stress profiling.
Four-slot	Combination between two-slots and ring-core. Same advantages as ring-core. Additionally, the Poisson's ratio can be obtained within the same experiment. Procedure is more time-consuming.	Homogeneous coatings with a thickness range 1-10 µm, also when non-biaxial stress is present.
Ion beam layer removal (ILR)	Method based on cantilever bending after stress relaxation by FIB cutting. Fully analytical procedure, but complex and time-consuming experimental procedure.	Best procedure for depth profiling for coatings with range 0.5-10 µm

3. Residual stress depth profiling

The FIB-DIC method can also be used for residual stress depth profiling by performing the milling process in a stepwise fashion and by using an extended integral method for stress calculation. Such method was originally proposed for the hole-drilling method and can be adapted to other milling geometries provided that the basic influence functions *A(H,h)* are assessed by FE calculations:

$$\varepsilon(h) = \int_0^h A(H, h) \cdot \sigma(H) \cdot dH \quad (12),$$

which can be converted into a matrix formulation by assuming the calculation is divided into *n* calculation steps:

$$\varepsilon_i = \sum_{j=1}^{j=i} \boldsymbol{A}_{ij}\sigma_j \quad 1 \le j \le i \le n \quad (13),$$

where $\boldsymbol{A_{ij}}$ is a triangular matrix of FE calculated calibration coefficients and ε is the measured strain relief.

The main limitation of the integral method for residual stress depth profiling relies on the mathematical ill conditioning of the matrix inversion procedure to calculate the stresses, which involves significant calculation errors for $z/d_m > 0.3$, as discussed in previous papers. An attempt to solve such limitation is to increase the stub's diameter in order to keep $z/d_m < 0.3$, or even to perform tests with multiple diameters to gain information on residual stress distributions over a wider range of depth. Such an approach has been lately used to evaluate residual stress profiles in multi-layer Cr-CrN coatings, where a significant effect of the residual stress depth-profile on scratch adhesion was observed and discussed.[119]

In a recent study, Korsunsky *et al.* [120] have presented and validated a novel approach for residual stress depth profiling, based on a novel calculation procedure that revises the classical integral method (Eq. (13)) by focusing on eigenstrain reconstruction[121] to evaluate the residual stress profile. This new method can overcome the limits of previous approaches, thus allowing for residual stress depth profiling with <50 nm resolution.

4. Factors affecting method's reliability

Several error sources have been identified for this method, most of which can be properly taken into account and corrected for. In particular, the quality of SEM images has been

identified as the major source of experimental errors and data uncertainty. Recent papers by de Hosson and co-workers[113] have presented a statistical method to check instabilities in SEM imaging, based on the correlation of digital images and the definition of four different parameters that can be used to evaluate image qualities and to remove bad images from the analysis.

Some works have focused on method development as well, showing that best SEM imaging conditions can be achieved by using the integration of a large number (usually 128) of micrographs acquired with a low dwell time.[104] The same papers have shown strain measurement to be much more accurate and reliable along the fast SEM scan direction.[104,113] The noise associated with strain measurement was quantified to be in the range of $1.0\text{-}5.0\times10^{-4}$ for SEM magnifications ranging from 10000 to 50000x.[112,113] A further improvement in terms of strain resolution can be achieved by using specifically designed surface patterning/decoration[111] and by applying automated electron (and ion) beam drift correction strategies.[104]

Another relevant source of calculation errors can be represented by the choice of the elastic parameters for calculating stresses from strains. This is a particularly critical situation in the case of strongly oriented materials and/or stress analysis inside single grains with unknown orientation. A recent paper by E. Salvati *et al.*[122] introduced a simple statistical procedure to quantify the uncertainty of residual stress evaluation due to elastic anisotropy effects in materials with unknown texture. It is demonstrated that the uncertainty in stress calculation can even reach 40% in case of materials with a high anisotropy factor A (Nickel alloy, $A = 2.83$), while it can be kept below 10% for Aluminum ($A = 1.23$).

Finally, the major issue of the additional residual strains induced by FIB damage should be carefully considered. Recent Molecular Dynamics (MD) studies[123] have reported a detailed and quantitative analysis of the defects and additional strains induced by a cascade of ion

impacting a material (Silicon) with known energy. Obtained results allowed quantifying the thickness of the damage layer and the amount of induced residual strains. In combination with validation experiments, it was then possible to evaluate the minimum pillar diameter for which the induced strain can be considered as negligible (i.e., lower than the usual strain error associated to DIC). Results for a 30 kV Ga^+ FIB showed that the minimum pillar diameter for Silicon is equal to 1 µm, thus meaning that FIB artifacts can be considered as negligible for a trench.

5. Industrially relevant applications

In recent years, the method was used for a very wide range of industrially relevant applications. Examples include (a) the use of this technique for high-resolution stress mapping and stress profiling in thin films and coatings, (b) strain mapping in MEMS and TSV structures, (c) the analysis of residual stress distribution inside single grains (or across GBs) in polycrystalline materials, (d) the investigation on stress concentration and/or redistribution in correspondence of fatigue cracks, (e) model validation for residual stress prediction in BMGs, or even (f) residual stress mapping in biomaterials and biological (dental) tissue.

The method has also been demonstrated to be extremely useful for the design and production of multilayered PVD coatings with tailored residual stress profile and improved adhesion. In a recent paper, Renzelli *et al.*[119] showed that multilayer Cr-CrN coatings with controlled stress gradient could be produced by varying the applied bias voltage during deposition, as also highlighted by other recent publications. In their work, the authors demonstrated that reducing the interfacial residual stress can be extremely effective in improving the scratch adhesion, while maintaining constant the average compressive stress throughout the film. Residual stress profiles where selected through analytical modeling, and then experimentally measured by incremental FIB-DIC ring-core method.

D. Methods validation and critical comparison of the available measurement techniques

In order to establish a critical comparison between different residual stress characterization methods, a multilayer chromium nitride (CrN) film was deposited on a Si(100) substrate by means of magnetron sputtering. Deposition of CrN layers was made in an $Ar+N_2$ gas mixture at a temperature of 350 °C. Three consecutive CrN sub-layers, each 1 μm in thickness, were deposited by varying the energy of incident ions and without interrupting the film growth. A sequence of three bias voltages of −40, −120 and −80 V (from substrate to external surface) was used, resulting in a total film thickness of 3 μm. In Figure 5a, an SEM micrograph of the film cross-section shows changes in film morphology corresponding to the bias voltage transitions.

The residual stress gradient in the sample was characterized by three different techniques: (a) the conventional wafer curvature method based on the Stoney equation,[28,124] (b) cross-sectional X-ray nano-diffraction using a sampling step of 15 nm and X-ray beam diameter of 30 nm,[98] and (c) FIB residual stress profiling, according to the procedures described in the previous sections.

The FIB method allows for both the assessment of the average residual stress in the film as well as for the evaluation of the residual stress depth profile. Figure 5b shows a micro-pillar that was incrementally milled by FIB using a current of 48 pA, resulting in a relaxation strain profile reported in Figure 5c. In this profile (Fig. 5c), a clear transition from a slow negative relaxation strain in sub-layer-1 to higher positive strains in sub-layer 2 is observed. This corresponds to mild tensile stress states in sub-layer 1, followed by a higher compressive stress in sub-layer 2.

According to the stress calculation procedure reported in Section II-C, the average residual stress analysis by FIB indicated a value of -584±120 MPa, which is in very good agreement with the result from the curvature method of -429 MPa.

As reported in other works,[103,125] curvature measurements provide usually slightly lower stress values, in comparison with FIB-DIC. This observation can be explained by considering that FIB-DIC experiments acquire information from a smaller gauge volume (a few μm^3), while curvature measurements provide information from a larger scale and also include stress relaxation phenomena due to the presence of micro-droplets and micro-cracks over the entire film surface.

A comparison between FIB-DIC and cross sectional nanodiffraction is reported in Figure 5d, where a remarkably good agreement between both techniques is indicated. In particular, both methods demonstrate a clear transition from mild tensile stress in the sub-layer near to the surface (where grain growth contributes to stress relaxation), to a significantly higher compressive stress in the second sub-layer, which is associated with the higher bias voltage (−120 V) applied for the sub-layer 2. Then, a relatively smaller compressive stress is detected in the bottom sub-layer, corresponding to the bias voltage of −40 V. Finally, we observe a sharp increase of the compressive stress in the film's region near to the interface, corresponding to the early stages of film growth with a fine-grained microstructure.

Finally, it can be concluded that both approaches provided very complementary data on the residual stress gradients in the graded CrN film.

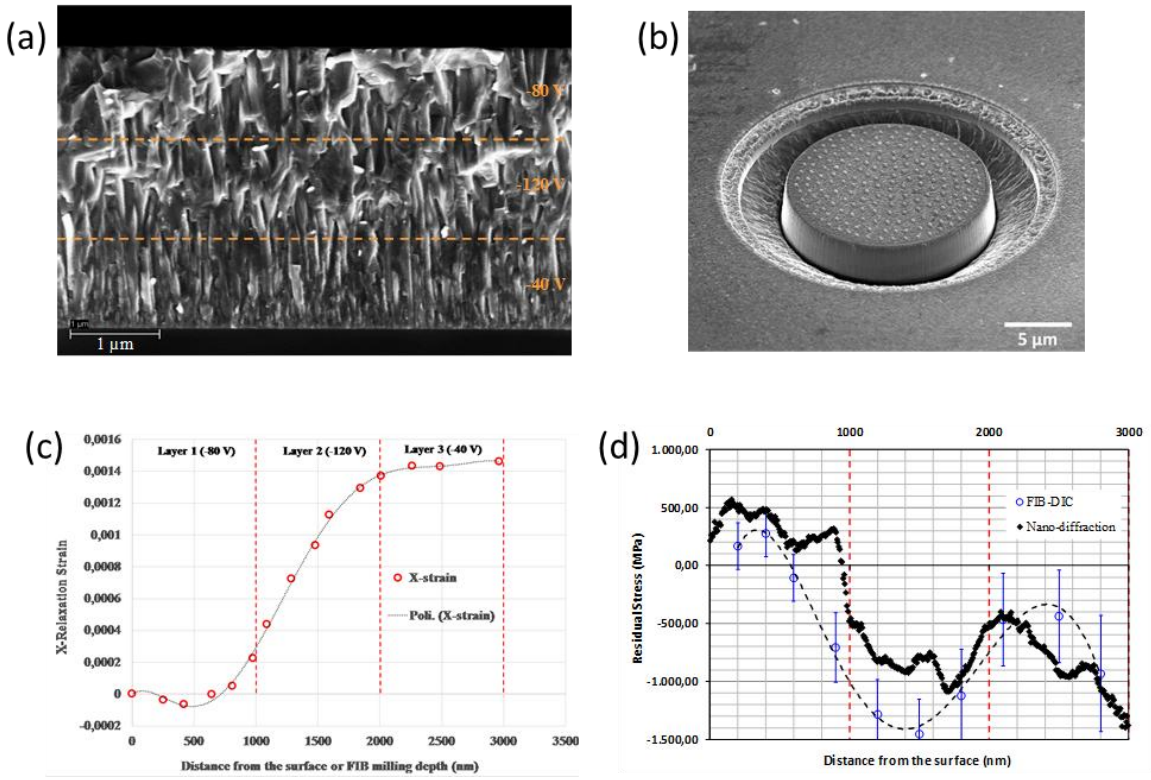

Figure 5: Complementary results from X-ray nanodiffraction and FIB-DIC analyses of residual stresses in 3µm thick CrN thin film sputtered in steps using three bias voltages of –40, –120, –80 V (a). A FIB incremental milling of a micro-pillar (b) using a current of 48 pA resulted in a relaxation of the strain profile (c), which was used to determine the FIB-DIC stress depth profile (d). For comparison, a stress profile evaluated from X-ray nanodiffraction with a sampling step of 15 nm is presented. Results presented here demonstrate that both nanodiffraction and FIB-DIC profiling techniques have become robust methods for stress profiling with sub-micrometer spatial resolution, for which standardization and industrialization routes could be open.

III. Stress in polycrystalline films: Current models and selected examples

A. Modeling stress development during polycrystalline thin film growth

1. Non-energetic deposition conditions

As noted above, there is a large literature quantifying the evolution of stress in numerous systems for many deposition methods and processing conditions. Because of the impact of stress on film performance and failure, there is a strong motivation for trying to understand it in terms of the underlying atomic-level processes occurring during film growth. In this section we describe recent

progress in developing a rate-equation based model to understand the dependence of stress on the temperature, growth rate and evolving microstructure.

Many different kinetic processes occurring simultaneously during film growth can influence the stress, including deposition, attachment of atoms to terrace ledges, GB formation, and diffusion of atoms on the surface and into the GB. Some of these are shown schematically in Figure 6. The deposited atoms can have low kinetic energy in non-energetic processes such as evaporation or electrodeposition. In energetic deposition processes such as magnetron sputtering (MS), the deposited species have much higher than thermal kinetic energies that can modify the stress. For example, sputter deposition is commonly used to counteract large tensile stresses that develop in films of refractory materials if non-energetic deposition is used. The impact of energetic particle bombardment on the intrinsic stress development will be addressed specifically in Sections III-A.2, IV-B.2 and IV-E.

After adsorption on the surface, the deposited atoms may be mobile if the diffusivity is sufficiently high. These atoms can meet other atoms and form clusters on the surface or diffuse to sinks such as terrace edges or GBs. The film's microstructure also evolves as the film grows. Starting from a bare substrate, the deposited atoms cluster into islands that are initially not connected, assuming that the film does not wet the substrate. As the thickness increases, the isolated clusters start to intersect and coalesce into a uniform film. This coincides with the formation of GBs between the islands. Ultimately, the film becomes relatively uniform and flat; depending on the material mobility the grain size may continue to change with the thickness as it grows.[126]

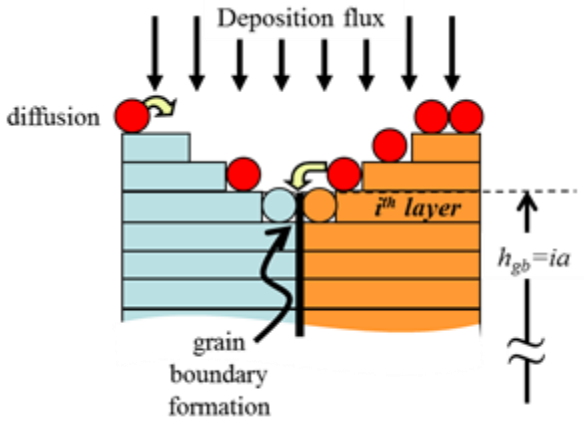

Figure 6: Schematic of a section of thin film around a GB illustrating kinetic processes that can influence stress. Reprinted with permission Thin Solid Films **516**, 1 (2012). Copyright 2012 Elsevier.

The measurements of stress-thickness in Figure 1b show that the film stress goes through different stages corresponding to the evolving microstructure. In the earliest stages, the shallow slope indicates that the incremental stress is small. At a thickness of ~ 10 nm, the slope starts to increase, indicating a tensile stress in the layers being deposited. At ~ 30 nm, the stress-thickness reaches a maximum and the incremental stress changes from tensile to compressive. After this, the incremental stress remains compressive, and the average stress ultimately becomes compressive.

These different regimes of stress evolution are correlated with the evolution of the film's microstructure with thickness. The early low-stress stage corresponds to the film consisting of individual islands on the surface. The increasing tensile stress corresponds to the onset of coalescence, where the individual islands start to impinge on each other and form GBs between them. For metal films like Ag, the transition to compressive stress corresponds to the film becoming fully coalesced into a continuous film. This results in the existence of a maximum (tensile peak) in the film force evolution with thickness. Recent findings, based on simultaneously coupling MOSS and surface differential reflectance spectroscopy (SDRS) during deposition of a series of high-mobility metal films, have demonstrated that the onset of film continuity coincides with the tensile

peak.[127] For materials with lower atomic mobility, the incremental stress may remain tensile and not become compressive, at least under conditions of low-energetic vapor flux.

The evolution of stress with thickness depends on the material and was described as type I or II by Abermann.[128] The behavior shown for the Ag in Figure 1 is called type II; this is characterized by the incremental stress changing from tensile to compressive with thickness and relaxing when the growth is interrupted. These materials have relatively high atomic mobility or low melting points, like Al, Ag or Au. Alternatively, in type I materials the incremental stress remains tensile with thickness and does not relax when the growth is interrupted. These materials have relatively low atomic mobility or high melting points, such as Mo, Ta, and W.

The different stress behavior depends on the material, but it may also be modified by changing the temperature or growth rate. For instance, evaporated Fe films grown at low temperature show stress-thickness evolution like type I materials, but when the same material is grown at higher temperature the behavior is like a type II material.[35,58] In general, higher growth rates and lower temperatures tend to promote type I behavior, while lower growth rates and higher temperatures promote type II behavior.

The stress depends on the grain size but its dependence is complicated. Koch *et al*. [129] showed that smaller grain size can lead to more compressive stress in the growth of a type II material. Similar behavior was found for electrodeposited Ni and Cu films at low growth rates[130] where smaller grain size led to more compressive stress. However, at high growth rates a smaller grain size led to the stress becoming more tensile. This shows that stress cannot be understood without considering the interaction between the growth rate and the grain size. The model developed below is able to explain this complicated behavior.

There have also been numerous measurements of the stress evolution during relaxation when the growth is interrupted.[33,58,131] This relaxation can be reversible if the growth is resumed shortly after the interruption;[67,132,133] for longer times there can also be an irreversible component.[134]

Measurements of the relaxation dependence on the grain size[135] suggests that GBs play a role in relaxation as well as growth stress.

The stress measurements provide guidance about the underlying kinetic processes controlling it. The correspondence between the rise in the tensile stress and the onset of island coalescence suggests that GB formation plays a role. Based on this, Hoffman[136] suggested a mechanism that considers the energy for creating new sections of GB between islands and for elastically deforming the islands. This analysis shows that adjacent islands will snap together to form new GB as long as the increase in strain energy is less than the decrease in interfacial energy. The maximum tensile stress is equal to

$$\sigma_T = 2\left(\frac{M_f \Delta\gamma}{L}\right)^{\frac{1}{2}} \qquad (14),$$

where M_f is the film's biaxial modulus, $\Delta\gamma$ is the change in interfacial energy and L is the grain size. Films with small L are predicted to have more tensile stress at coalescence because of the large number of GBs, in agreement with recent experimental findings.[36] Similar results for the stress at coalescence have been produced by others using different geometries.[137,138]

The transition from tensile to compressive stress in type II materials is more controversial and several mechanisms have been proposed. One mechanism suggests that the compressive stress is inherited from the stress in the individual islands before they coalesce. This is attributed to the effect of the surface stress inducing compression in the islands before they become firmly attached to the surface. However, it is difficult to reconcile this mechanism with the reversibility of the stress relaxation.

GBs provide symmetry-breaking sites where atoms can be added to the film without distorting the lattice. Nix and Clemens[137] proposed that adding atoms at the GB can relax the tensile stress in the film. Spaepen[139] suggested that other sites where atoms can be trapped are at ledges on the

growing surface. These mechanisms provide ways in which compressive stress can be generated in the film, but they do not explain why the stress should become compressive. Indeed, with increasing thickness, the film can develop *net* compressive stress, indicating that it is not just relaxing the initial tensile stress. Because elastic strain energy raises the total energy of the system, this means that the stressed film has higher energy than it would if there were no stress. Since generation of stress raises the system's total energy, this indicates that there must be a driving force for the insertion of atoms into the film to generate compressive stress.

Chason *et al.*[65] have proposed that the driving force for atom insertion into the GB is the supersaturation of atoms on the surface. This is a consequence of the non-equilibrium nature of film growth which raises the chemical potential of atoms on the surface ($\delta\mu_s$) during growth relative to equilibrium. On the other hand, stress in the film changes the chemical potential of atoms in the GB by $-\sigma\Omega$ where Ω is the nominal volume of the atom. For compressive film stress (i.e., negative values of stress) this raises the chemical potential and tends to drive atoms back out of the GB. Since the chemical potential difference between the surface and GB determines the rate at which atoms diffuse into the GB, the system can reach a steady-state where there is stress in the film due to the supersaturation on the surface. The diffusion of atoms in and out of the GB due to the surface and GB chemical potentials is also consistent with the reversibility of the stress when the growth is stopped and then resumed.

These mechanisms of tensile stress generation (due to GB formation) and compressive stress (due to insertion into GBs) have been incorporated into kinetic models[65,140] to compare with the measurements. In the model discussed below, we consider the evolution of stress in each layer of the film while it is growing. We assume that diffusion in the GB is slow so the stress in the layer does not change after it is covered by the next layer. An alternate set of analytical equations can be derived if we assume that the GB diffusion is rapid, i.e., the stress is uniform through the thickness of the film.[65,141] For these two kinetic limits, we can derive analytical expressions for the stress

evolution. Other GB diffusion conditions can be considered by solving the equations numerically but they will not result in simple analytical expressions.

The tensile stress in the i^{th} layer is reduced by the insertion of atoms into the GB (N_i):

$$\sigma_i = \sigma_T - M_f \frac{N_i\, a}{L} \qquad (15),$$

where a is the nominal size of the atom ~ $\Omega^{1/3}$. Combining this with the rate of atom insertion produces an equation for the stress evolution:

$$\frac{\partial \sigma_i}{\partial t} = -\frac{\beta D}{aL}(\sigma_i - \sigma_c) \qquad (16a),$$

where

$$\beta \equiv \frac{4 C_S M_f \Omega}{kT} \qquad (16b),$$

C_s is the concentration of mobile atoms on the surface, D is the effective diffusivity for transitions from the surface into the top of the GB, and $\sigma_c \equiv -\delta\mu_s/\Omega$.

This equation describes the stress in the layer at the surface, starting from the time when adjacent islands come together in the layer to form a new segment of GB. At this point, the stress is equal to σ_T. The stress decays exponentially with time until the top of the GB layer is covered over by the next layer. The amount of time that the i^{th} layer is at the surface is equal to $a/\frac{dh_{gb}}{dt}$ where $\frac{dh_{gb}}{dt}$ is the rate at which the top of the GB is moving upwards. The resulting stress in the layer is equal to

$$\sigma_i = \sigma_C + (\sigma_{T,o}\left(\frac{L_o}{L}\right)^{1/2} - \sigma_C) \cdot e^{\frac{-\beta D}{L\frac{dh_{gb}}{dt}}} \qquad (17)$$

Here we have explicitly shown the grain size dependence of the tensile stress σ_T by assuming that it has the value $\sigma_{T,o}$ when the grain size is equal to L_o. In the steady-state, the GB grows at the same

rate as the rest of the film and $\frac{dh_{gb}}{dt}$ equals the average growth rate, *R*, so that the steady-state stress during growth can be expressed as

$$\sigma_{growth} = \sigma_C + (\sigma_{T,o}\left(\frac{L_o}{L}\right)^{\frac{1}{2}} - \sigma_C) \cdot e^{\frac{-\beta D}{LR}} \quad (18).$$

The model shows the contributions of different parameters to the steady-state stress. The exponential contains the term *D/RL*, showing how larger diffusivity or lower growth rate will drive the stress to be more compressive. This is consistent with the observations of type I and II materials as well as measurements of the temperature and growth rate dependence. Both the exponential and the tensile stress depend on the grain size, which can explain the observed dependence of stress on the grain size. The rate at which the GB height changes is higher during the initial stage of coalescence than it is at steady-state, which is consistent with the tensile to compressive transition in stress with thickness observed for type II materials. This effect was confirmed by studying the stress evolution in patterned films that grew as an array of hemispherical islands.[142,143]

In order to compare the model predictions quantitatively with experiments, it is necessary to fully characterize the sample's microstructure. This is important because in many films the grain size changes as the film grows. As described by the structure zone model (SZM) of Thornton and Hoffman,[25] the grain size can remain constant (zone I), change at the surface but not throughout the film (zone T), or change throughout the film (zone II). The consequence of the microstructural evolution for the stress-thickness can be seen in Figure 7. The stress-thickness in Fig. 7a shows results from electrodeposited Ni which grows with constant grain size (zone I). As predicted by Eq. (18), the constant growth rate and grain size lead to a constant incremental stress. This is consistent with the stress-thickness evolution reaching a constant slope at larger thicknesses in the figure. The dependence of the steady-state stress on *R*, extracted from these data, is shown in Fig. 7b. The red

line represents the results of the model using parameters obtained from non-linear least squares fitting of the data.

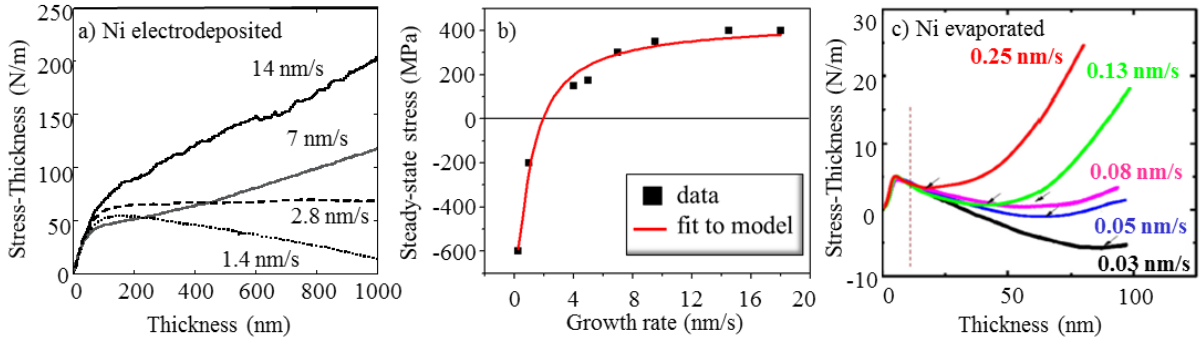

Figure 7: a) Evolution of stress×thickness in electrodeposited Ni at different growth rates indicated in the figure. b) Steady-state stress as a function of growth rate determined from the data in (a). c) Evolution of stress-thickness in evaporated Ni at different growth rates indicated in the figure (adapted from Ref. [144]).

For comparison, evaporated Ni films deposited under UHV conditions have very different microstructural evolution. Measurements by Yu *et al.*[144] indicate that Ni grows with a zone II behavior. The film's grain size is proportional to the thickness, and the grain growth proceeds through the thickness of the film so that the grains remain columnar in morphology. Therefore we cannot assume the grain size is constant with thickness. In addition, the extensive grain growth in the underlying layers can produce additional tensile stress due to densification of the film. As originally described by Chaudhari,[145] increasing the grain size from its initial value creates stress by removing regions of excess volume at the GBs; this can be modified to consider the contribution of grain growth to the stress in growing films.[23,144] The effect of the changing grain size and grain growth has significant consequences for the stress-thickness evolution measured in the evaporated Ni shown in Fig. 7c. Instead of reaching a constant slope, the slope changes continuously with thickness, and a turnaround phenomenon from compressive to tensile incremental stress is observed (indicated by arrows).

Validation of the model is ongoing. New experimental studies are being performed in which all of the necessary parameters are characterized so that the model can be compared directly with the

data. Modifications of the model are also being made to include the effect of grain growth so that the results of zone II growth can be analyzed.[130] A goal of all this work is to see if a series of kinetic parameters can be obtained for different materials and growth processes that will allow the stress to be predicted under different conditions.

2. Influence of energetic vapor flux

It is well known that energetic particle bombardment during growth can strongly modify the stress,[25,146] affecting not only surface but also sub-surface processes. Hoffman and Thornton were the first to study such effects, and they reported in a series of papers on various single metal films deposited by cylindrical magnetron sputtering over a large range of Ar working pressure a clear transition from tensile to compressive stresses when the working pressure was decreased.[147–150] They additionally observed that the critical pressure for the compressive to tensile transition increased with the atomic weight of the metal target relative to that of the working gas, with increasing discharge voltage, and was dependent on the cathode geometry.[151–153] They concluded that the atomic peening mechanism[30,154] contributed to these effects, whereby the impact of incident energetic particles produced recoil implantation of the coating material surface atoms and entrapment of working gas atoms, at the origin of compressive stress build-up in the film. However, the influence of the deposition rate on the compressive stress magnitude could not be isolated from these experiments.[151]

In an effort to provide a more complete picture of the stress-inducing effects during PVD film growth under energetic deposition conditions, the model presented above was extended to take into account the contribution of incident particle bombardment. Indeed, defect incorporation through ballistic-induced displacement sequences and/or collision cascades in the growing layer is ignored in the expression of the intrinsic stress given by Eq. (18). It is well known, however, that incident particles with energy in the range from several eV up to 100 eV, as typically encountered in MS

discharges or CAD, provide means to affect not only surface but also sub-surface processes. Collisions between the impinging particles and surface atoms can result in reflection of incoming species from the surface, re-sputtering or kinetically-assisted surface diffusion.[155] Arriving particles can also implant in the shallow surface through a series of knock-on mechanisms, providing, by forward momentum transfer, kinetic energy to atomic recoils. This will induce displacement of sub-surface atoms located close to the impact site to more favorable sites, like vacant sites, but also will contribute to the creation of point defects (at interstitials and substitutional sites) above a certain energy threshold. If film densification occurs when energetic particles flux is involved, it is often accompanied by the development of compressive stress, as a result of "atomic peening process".[146,154,156] The volumetric distortion is proportional to the fractional number of atoms being displaced from their equilibrium sites, which based on the forward sputtering model of Sigmund,[157] implies a square root dependence of the compressive stress on the incoming particle energy.[146]

This explains why low-mobility (type I) materials exhibiting tensile stress under non-energetic deposition conditions are usually under compressive stress when subjected to energetic vapor fluxes. An illustration of this phenomenon is shown Figure 8a which compares the evolution of the film force per unit width of sputtered Ta films with film thickness as a function of Ar working pressure. A clear transition from a compressive towards a tensile steady-state stress is observed with increasing Ar pressure from 0.12 to 0.75 Pa. In particular, there exists a critical pressure, P_c, at which the net average stress would be zero (P_c ~0.5 Pa in the present example). The value of P_c is material dependent (it increases with the target/gas mass ratio, M_t/M_g), but also depends on the deposition rate R, geometry of the deposition system (the target-to-substrate distance, d_{TS}) and nature of plasma discharge.[146] Conversely, the application of a negative bias voltage to the substrate, at a fixed working pressure, increases the compressive stress due to contribution of ion bombardment-induced defect formation in the growing layer (compare orange and green force curves in Fig. 8a). The development of tensile stress at high working pressure is related to the

formation of underdense columnar growth morphology, typical for refractory metals deposited under kinetically limited surface diffusion conditions.[35,58]

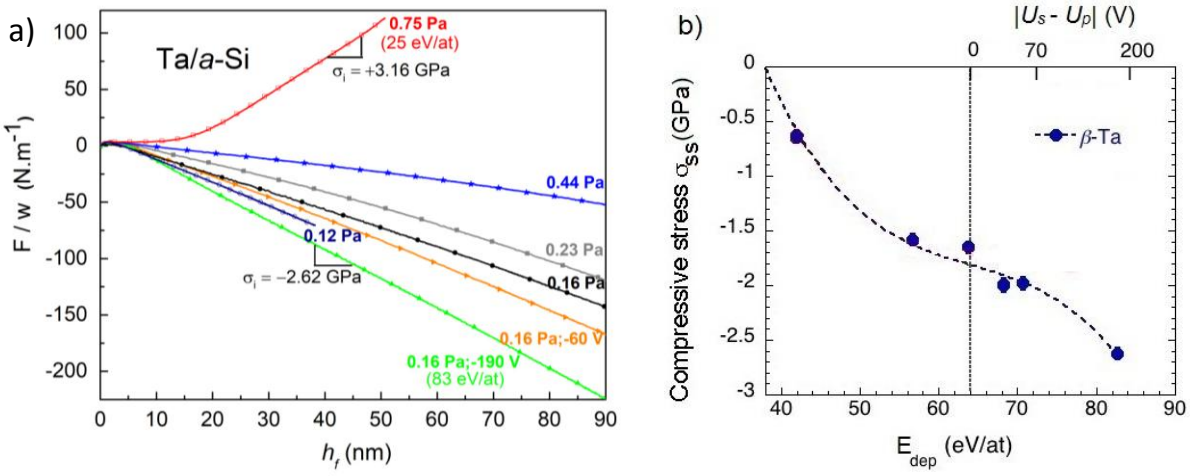

Figure 8: a) Evolution of the stress-thickness during sputter-deposition of Ta films at different Ar working pressure (0.12-0.75 Pa range) and bias voltage values (ground, –60 and –190 V). Note that grounded (0 V bias) substrate conditions correspond to lines without mention of bias voltage and values given in parenthesis correspond to the average energy per deposited atom, E_{dep} (see text). b) Evolution of the (compressive) steady-state stress with E_{dep}, determined from the data in (a). Data are taken from Ref. [158].

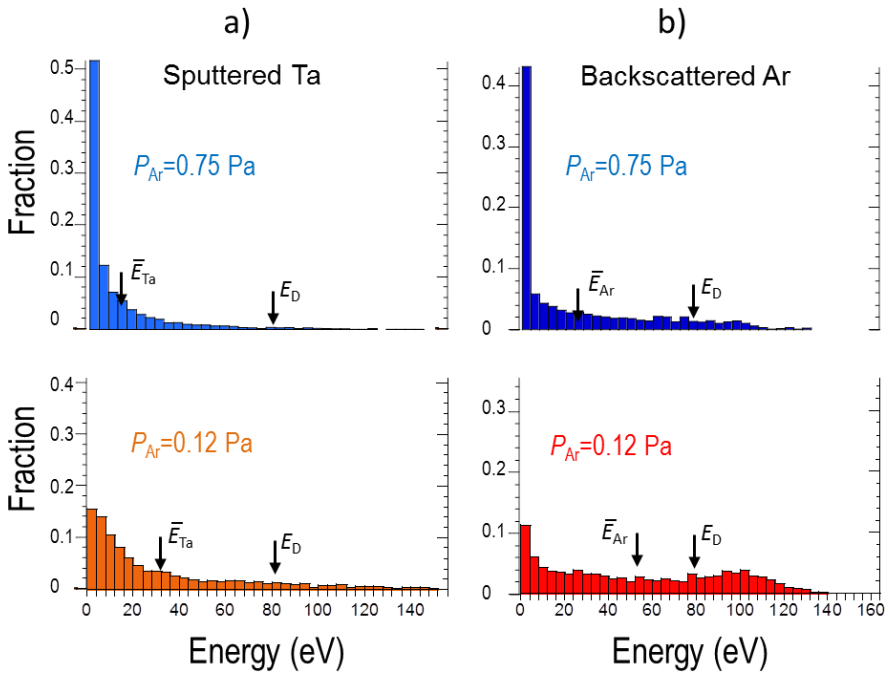

Figure 9: Energy distributions (obtained from "SIMTRA" calculations[159]) for a) sputtered Ta atoms and b) backscattered Ar at two different Ar working pressures: 0.12 and 0.75 Pa.

Compared to thermal evaporation, the particles flux reaching the substrate for the case of sputter-deposition is characterized by a broad energy distribution of film-forming species. For conventional direct current magnetron sputtering (DCMS) discharges, the film-forming species are essentially neutrals, i.e. sputtered (target) atoms and gas atoms reflected back from the target, while for high-power impulse magnetron sputtering (HiPIMS),[160] there is a large fraction of ionized species.[161,162] The energy distribution of sputtered atoms and backscattered neutrals depend on the target material type and target voltage, and are therefore intrinsically related to the plasma conditions.[25,162,163] However, the energy of ions can be controlled by applying to the substrate a certain bias voltage, U_s. Also, particles leaving the target experience collisions with working gas atoms (if d_{TS} is larger than the atom mean free path) during their transport in the gas phase, so that the energy (and angular) distribution of the particles flux reaching the substrate may differ significantly from that of the nascent flux leaving the target. As an example, the energy distribution of Ta sputtered atoms and Ar backscattered atoms is shown in Figure 9, for the case of DCMS of a Ta target with 280 eV Ar ions, at two different Ar working pressure. These data were computed using SRIM[164] and SIMTRA[159] codes, assuming a target-to-substrate distance of 18 cm. The particles energy range spans two order of magnitudes, from a fraction of eV to > 100 eV. Increasing the Ar working pressure from 0.12 to 0.75 Pa leads to a modification of the energy distribution of the incoming particles: a large fraction of Ta and Ar atoms have energy lower than 2 eV, due to collision-induced thermalization process during transport in the gas phase. Consequently, the average energy of sputtered Ta atoms, $\bar{E}_{Ta}$, decreases from 31.1 to 12.3 eV, and that of backscattered Ar, $\bar{E}_{gas}$, from 52.9 eV to 25.9 eV.

Knowing the relative fraction of sputtered atoms, backscattered gas atoms and ions, the mean energy deposited per incoming Ta particle, E_{dep}, can be calculated from the following expression[158]

$$E_{dep}(eV) = \bar{E}_{Ta} + \Phi_b \bar{E}_{gas} + \Phi_i n_i (U_s - U_p) \qquad (19),$$

where U_p is the plasma potential (typically ≈ 10 V in standard magnetron configuration), Φ_b the ratio of backscattered particles to sputtered particles, Φ_i the ratio of ionized particles to sputter particles, and n_i is the charge state of the ionized species. As reported in Figure 8b, the compressive stress gradually increases with E_{dep}, suggesting a larger propensity of defect creation with increasing deposited energy. If the mean energy per deposited atom provides a simple way of characterizing the incoming particle flux in terms of growth energetics, this quantity does not reflect *per se* the important contribution of single collisional events related to the high energy tail (> 100 eV) of the particles energy distribution, which are scarce events but at the origin of point defect creation. Indeed for Ta, the energy threshold for atomic displacement, E_D, is 80 eV.[165] While for sputtered atoms, the fraction of species having energies higher than 80 eV is small (around 10% at low pressure), this fraction reaches 31% for the case of reflected Ar (see Figure 9). The contribution of backscattered gas atoms should not be overlooked when addressing the issue of stress in sputtered films, especially for heavy-mass targets sputtered with lighter particles for which the backscattering yield Y may reach > 20% (Y roughly scales with $(M_t/M_g)^2$).[146]

Relatively large compressive stress values, up to −4 GPa, have been reported for ion beam-sputtered Mo films, as a result of incorporation of interstitial defects which induce a volume expansion of the crystal lattice and an associated expanded stress-free lattice parameter.[87,166] If "atomic peening" is a concept known for several decades, the kinetics of defect incorporation, their underlying mechanisms and the interplay with film's microstructure, have not yet been systematically studied and elucidated. Fillon *et al.*[167] have reported an increase of compressive stress for sputter-deposited Mo films at higher deposition rates, a behavior which is opposite to what is observed for materials grown under non-energetic deposition conditions (see Figure 7a). For Mo films, Magnfält *et al.*[168] have evidenced a densification process in which atoms are inserted at the GB, causing a source of compressive stress without significant lattice expansion. In this case, the stress field is biaxial, while the incorporation of point-defects in the grain interior would

generate a triaxial stress state.[166,169] Interstitials (and to some extent substitutional atoms) are, in general, unstable and can be annihilated by diffusion towards the nearest underdense regions if sufficient energy is provided. Based on these observations, we proposed to add to the thermally activated diffusion processes considered in the kinetic model presented in the previous section two other processes related to sub-surface point defects creation by atomic peening (see Figure 10a), namely:

- Incorporation of excess atoms at the GB. The average in-plane grain size is denoted as L.
- Creation of defects in the grain, at a depth l from the surface. The value of l depends on the deposited energy (it is expected to decrease with increasing working pressure P), but is typically a few monolayers (up to ~2 nm).

We assume that the first process is a diffusionless mechanism occurring by collision-induced displacement and relocation of atoms to more favorable sites in the vicinity of the GB. This region is marked by the shaded area in Figure 10a and its width is approximated to be proportional to the distance l. The contribution of defect trapping at the GB to stress is expressed as

$$\sigma_{gb}^{energ} = A_o \times (l / L) \qquad (20),$$

where A_o is a parameter that depends on the deposition conditions (E_{dep}, f, R) and that will be adjusted to compare the model with the data.

For the second mechanism, we consider the rate of defect creation to be equal to fc_o, where f is the flux of energetic particles and c_o is the number of defects generated per particle. We also take into account the possible annihilation of these defects at the free surface. The balance between defect creation and relaxation at the free surface depends on the characteristic time τ_s necessary to diffuse to the surface and the growth rate R. Since the surface is moving upward due to propagation of the growth front at constant R, the expression of τ_s is not simply given by l^2/D_i, where D_i is diffusivity of the considered defect. For its complete expression and more details on the stress

model, we refer the reader to Ref. [170]. It results that the concentration of defects in the steady-state regime, C_{ss}, is given by

$$C_{ss} = \frac{c_o f}{R} \frac{1}{\left(1 + \frac{l}{R\tau_s}\right)} \quad (21)$$

Note that at high R or low D_i, the rate of defects annihilation at the free surface goes to zero so that the value of C_{ss} saturates at $c_o f/R$. Conversely, when $R \rightarrow 0$ or $D_i \rightarrow \infty$, then $C_{ss} \rightarrow 0$. The contribution of defect trapping in the grain interior to stress can be written as

$$\sigma_{bulk}^{ener} = (1 - \frac{l}{L})\, \sigma_o C_{SS} \quad (22),$$

where the term σ_o represents the stress per defect retained in the bulk. The factor $(1-l/L)$ is present because we assume the bulk stress effect is proportional to the fraction of energetic particles that are not within a distance l of the GB. The complete expression for the steady-state stress during deposition with energetic species is therefore given by

$$\sigma_{ss}^{tot} = \sigma_{growth} + \sigma_{gb}^{ener} + \sigma_{bulk}^{ener} \quad (23),$$

where the different stress sources σ_{growth}, σ_{gb}^{ener} and σ_{bulk}^{ener} are given by Eqs. (18), (20) and (22), respectively.

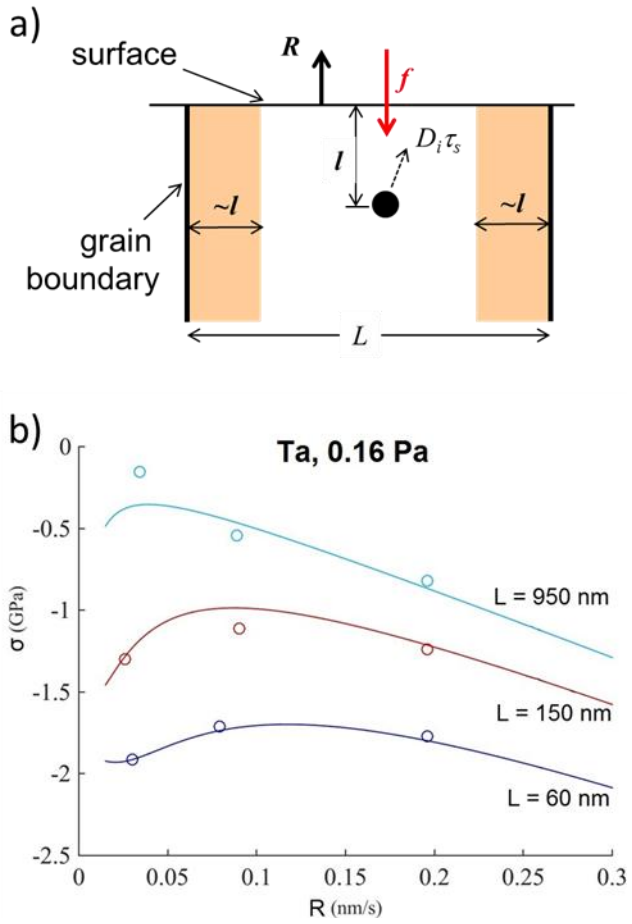

Figure 10: a) Schematic of the defect creation and annihilation processes due to energetic particle bombardment considered in the stress model. b) Evolution of the steady-state stress of sputtered Ta films with different grain-size *L* versus deposition rate *R*. Symbols refer to experimental data obtained from real-time MOSS and solid lines are fits to the model described in the text.

The comparison of the predictions of the model given by Eq. (23) with experimental data acquired for a set of sputtered Ta films with different controlled in-plane grain size[171] is shown in Fig. 10b, where solid lines correspond to best-fit values obtained from non-linear least-squares fitting procedure. One can observe that the trend of increased compressive stress at higher growth rates is captured by the extended kinetic model. This effect is more pronounced for the series of Ta films with the largest grain sizes (L = 950 nm). Looking at the individual terms of Eq. (23), it is found that the dominant stress contribution is σ_{bulk}^{ener} which counterbalances and even outweighs the thermally-activated surface diffusion term $\sigma_{growth.}$ The same trend is also reported for sputtered Mo films, and well reproduced by the model.[170] With decreasing grain size, the magnitude of the

compressive stress is found to increase: an almost linear-dependence of σ_{ss}^{tot} with $1/L$ at constant growth rate (not shown here) is observed, that can be ascribed primarily to the contribution of σ_{gb}^{ener} which scales with $1/L$, [see Eq. (20)]. The other term, σ_{growth}, also contributes to a higher compressive stress at lower grain size, but to a lower extent in the present experimental conditions.

The agreement between the calculated stress and the data shows that the model is capable of reproducing the dependence on R, P and L seen in the experiments which incentivizes further pursuing this approach to modeling the stress.

An even more challenging area of study is to model the stress evolution in alloy thin films. These are especially important technologically. Experiments in sputtered metals[172] and nitrides[173] show that in some cases the alloy behavior looks like a superposition of the stress behaviors of the individual constituents. This suggests that it may be possible to consider the stress in terms of a superposition of stress-induced effects in the single element systems. However, there exist situations, as presented below, where such simple considerations do not hold.

B. The impact of interface reactivity, alloying and phase transformation on stress

The sequence of compressive-tensile-compressive (CTC) stress evolution, shown in Figure 1b, is typical for high-mobility metals deposited on weakly interacting and inert substrates, such as amorphous SiO_2, for which texture inheritance can be disregarded and chemical reactivity is insignificant. The resulting film microstructure is, in this case, typical for a polycrystalline material. On a crystalline template, adatoms will feel the interatomic potential of the substrate, and will locate at favorable adsorption sites corresponding to minima of the potential energy landscape of the substrate.[40] Under conditions of sufficient surface diffusivity, a pseudomorphic epitaxial growth is observed, up to a critical thickness above which the stored elastic strain energy due to lattice mismatch with the substrate is relieved by means of nucleation and glide of dislocations, cluster nucleation, surface

undulations, etc.[174]. While the case of epitaxy, and how it affects growth stress, is not addressed in this article, we will highlight in what follows the influence of chemical interaction with the substrate on the stress evolution. The case of alloy thin films and *dynamic* (i.e., during growth) segregation will be addressed in Sec. III-B.2.

1. Interface reactivity and surfactant effects

Figure 11 illustrates the influence of chemical reactivity between the substrate and the deposited metals on the stress response. In Figure 11a, the film force evolution during growth of evaporated silver on amorphous germanium (*a*-Ge) layer is shown, comparatively to the deposition on *a*-SiO_2, as reported by Flötotto *et al.* [175]. A CTC behavior is observed for Ag film on both substrates, but the position of the tensile peak maximum is drastically altered. This means that the onset of film continuity is reached at a thickness of ~60 nm on *a*-SiO_2 and ~ 8 nm on *a*-Ge. TEM observations confirm that the Ag film deposited on *a*-Ge has much finer grain morphology, and the sequence of islands nucleation, islands coalescence and formation of a continuous film occurs at much smaller thickness comparatively to on *a*-SiO_2. By performing angular-resolved X-ray photoelectron spectroscopy, the authors disclosed that Ge atoms are segregating during growth of Ag, forming a Ge-rich topmost surface layer. The Ge surface coverage is below 1 ML and decreases with increasing Ag thickness (reaching 0.2 ML for ~300 nm thick Ag film). In the pre-coalescence stage, the higher density of islands and the lower surface diffusivity of Ag adatoms on the parent *a*-Ge surface (the diffusion barrier is 0.45 eV vs. 0.32 eV for Ag on *a*-Ge and *a*-SiO_2, respectively) promotes the formation of a continuous Ag film at earlier thickness, together with smaller grain size. In the post-coalescence stage, the segregating Ge atoms also hinder the surface diffusion of Ag and lead to continued renucleation of new Ag grains during growth. Due to the much higher GB

density of the Ag film deposited on *a*-Ge, this latter one develops larger compressive stress (see Fig.11a), in agreement with the model presented in Sec. III.A.

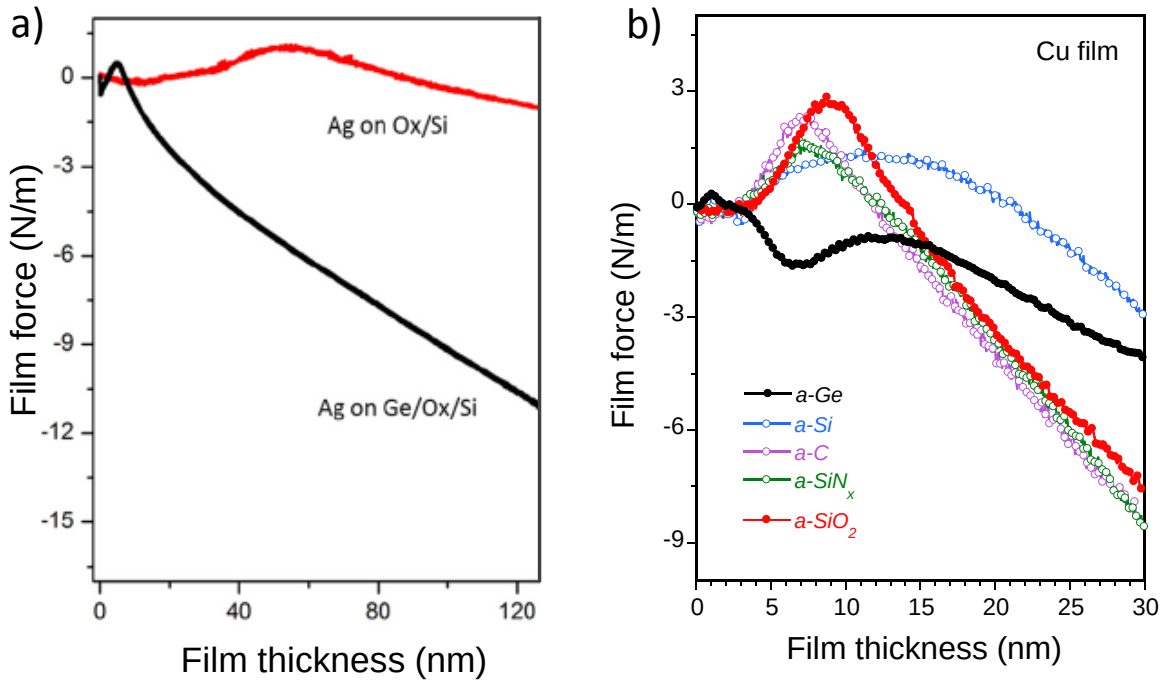

Figure 11: a) Real-time evolution of the film force per unit width during thermal evaporation of Ag films on *a*-SiO_2 and *a*-Ge surfaces at a growth rate R=0.035 nm/s; graph adapted from Ref. [175]. b) Real-time evolution of the film force per unit width during sputter-deposition of Cu films on *a*-SiO_2, *a*-Ge, *a*-Si, *a*-SiN_x and *a*-C surfaces at a growth rate R= 0.065 nm/s.

Fig. 11b shows the evolution of the film force during sputter-deposition of Cu films on different types of amorphous substrates, namely, *a*-SiO_2, *a*-Ge, *a*-Si, *a*-SiN_x and *a*-C layers. While Cu films deposited on *a*-SiO_2, *a*-SiN_x and *a*-C layers exhibit a similar CTC behavior (having a tensile peak maximum in the 7.5-9.0 nm range), the stress development on *a*-Si and *a*-Ge is markedly different: i) in the earliest growth stage, for Cu film thickness below 1 nm (~5 ML), the instantaneous stress goes slightly tensile instead of being slightly compressive, ii) there is no characteristic shape of a tensile peak, and iii) at later growth stages, above 15 nm, less compressive stress is being developed. Noticeably, for *a*-Ge, the stress shows a complex evolution, characterized by consecutive compressive and tensile stress transients below ~12 nm. SDRS experiments reveal the absence of isolated Cu islands on *a*-Si and *a*-Ge

surfaces for Cu film thickness below 2 nm, which suggests a strong chemical reactivity at the interface. The formation of an interfacial Cu_5Ge alloy is evidenced in Cu/Ge multilayer from analysis of XRD patterns.[176] The driving force for this compound formation is yet to be deciphered, especially to identify the fast diffusing species and any surfactant effect. It is interesting to note the significant improvement of the [111] out-of-plane texture of Cu films deposited on *a*-Ge comparatively to what is observed on *a*-SiO_2, while opposite results were reported by Flötotto *et al*.[175] for Ag on *a*-Ge. In the case of Ag/*a*-Ge, the continuous presence of segregating Ge adatoms throughout growth reduces the diffusion length of Ag adatoms, favoring copious renucleation events, which can explain the development of randomly oriented grains. The stronger reactivity of Cu, compared with that of Ag, together with dynamic intermixing favored by higher energy particle flux hitting the film surface under sputter-deposition conditions compared to thermal evaporation, likely explain the distinctive stress and texture evolutions of these metals on *a*-Ge. Finally, it can also be concluded from the stress data of Fig.11b that *a*-SiN_x and *a*-C behave as weakly-interacting surfaces, similarly to native silicon dioxide, and can be used as suitable buffer layers for depositing Volmer-Weber metal films for plasmonics or catalysis applications.

2. Alloying effect

The prior sections have reviewed and established the importance of GB in regulating the stress evolution in polycrystalline thin films. These examples concerned the case of single species films. For alloys, with atoms having different surface mobilities, segregation energies and atomic radii, one may expect synergistic or antagonist effects to come into play, resulting in different growth stresses. Changing the alloy composition affects the enthalpy of mixing, which likely also influences the stress state. Fu and Thompson[172] have studied the compositional-dependence of intrinsic stress of Fe_xPt_{1-x} alloys obtained by co-sputtering from

elemental targets at room temperature. This system is interesting because, when deposited as pure elements, Fe and Pt are behaving as low-mobility and high-mobility species, developing tensile and compressive steady-state stress, respectively. In the bulk, Fe and Pt are rather miscible elements: the Fe-Pt phase diagram exhibits a high-temperature fcc solid solution domain extending over the whole compositional range, while ordered Fe_3Pt, FePt and $FePt_3$ compounds crystallize at lower temperatures. With increasing Pt content in the alloy film, the intrinsic stress changed from tensile to compressive. However, the stress variation did not obey a linear mixing trend; in particular, the compressive stresses of Fe_xPt_{1-x} alloys with x ranging from 0.54 to 0.79 were larger than that of pure Pt. The authors explained this behavior by the propensity of the more mobile Pt adatoms to segregate at the GB, as confirmed from atom probe tomography (APT) analysis. The presence of Pt atoms in the GB modifies its chemical potential, so that more compressive stress is built-up if the chemical potential difference between the surface and the GB is enhanced with increasing Pt content in the film. The authors also pointed out that the driving force for the chemical enrichment at the GB is likely attributed to enthalpy minimization. They also noticed that the alloy with x=0.35 exhibited a "zero-stress" state together with negligible compositional segregation of one species at the GB compared to the bulk of the grains. It is noteworthy to disclose, for this specific system, that the alloy composition had little effect on the resulting grain size, and that the intrinsic stress was not affected by a change in the deposition rate at fixed alloy composition.

There are other recent reports which highlight the influence of solute segregation on the microstructure and peculiarities in the stress behavior of binary alloys. It was recognized that the addition of a few at. % of Al[177] or Ni[178] in Cu alloys formed by co-sputtering lead to a higher amount of compressive stress in the continuous (post-coalescence) film regime, comparatively to the pure Cu case. Similar findings have been obtained in the case of Cu-Ge

system upon increasing Ge content[179]. This effect is consistent with a tensile peak maximum being shifted to lower film thicknesses, indicating a reduced island size during nucleation and at percolation in the presence of Ge atoms. While a clear refinement (by a factor of 5) in grain size was revealed for Cu-Al alloys upon alloying Cu with 1 or 2 at.% Al, pointing to reduction of adatom surface mobility, similarly to incorporation of impurity elements like oxygen,[180] the decrease in grain size was more moderate (a factor 2-3) in the case of alloying with Ni. Kaub *et al*. proposed that the highest compressive stress for the Cu-Ni alloy with the least Ni content (5 at.%) was due to Ni-enrichment at the GB, with subsequent increase in Ni content resulting in a decrease of the compressive stress magnitude once the GB saturation is achieved.[178]

For the case of low-mobility metals, as exemplified in the Fe-Cr system, addition of Cr in solute concentration into Fe resulted in a decrease of the tensile stress in the post-coalescence regime.[181] An overall good correlation between the change in grain size L and magnitude of tensile stress σ was observed (with σ scaling with $1/L$), although variations in the degree of film texture, GB character (high-angle vs. low-angle) and GB chemistry[182] may also control the stress state in such systems.

Fu and Thompson also addressed the case of immiscible binary alloys by investigating the Fe-Cu system.[183] The stress evolution was monitored during sputter-deposition a $Fe_{0.51}Cu_{0.49}$ alloy at different *in situ* deposition temperatures, from 25°C to 325°C, using a 10 nm thick Si_3N_4 buffer layer acting as a diffusion barrier layer to prevent any deleterious silicide formation at the film/substrate interface. Increasing the deposition temperature resulted in the phase separation of the FeCu alloy into bcc Fe-rich and fcc Cu-rich phases. While similar stress evolutions were recorded in the initial stages of island nucleation and coalescence, the magnitude of the compressive stress was found to increase notably during the continuous growth regime with deposition temperature. Note that grain size and surface roughness

significantly increased with deposition temperature. From cross-sectional and plan-view STEM observations, it was concluded that the Fe islands nucleate off of the Cu islands. The origin of increased compression at higher deposition temperature could not be associated with a change in atomic volume during phase separation, as Fe and Cu share similar atomic volume. Rather, trapping of excess atoms at surface defects and/or at GB was invoked. The formation of a rougher surface with increasing deposition temperature would, however, reduce the diffusion of adatoms into GB due to self-shadowing effect and Erlich-Schwoebel barrier at the step edge.

3. Stress evolution in phase transforming thin films

As described in this review, the growth of a film – from an embryonic island to a coalescence state – will result in a dynamic evolution of the thin film stress states. This stress evolution has then been used to infer adatom mobility of the deposited species in relationship to the film's microstructure progression. In a similar manner, these same *in situ* stresses can be used to help deciphering phase state changes within the film, with such changes being crystalline-amorphous transformations, polymorphic crystalline transitions, and precipitation. Thus, stress monitoring can provide unique diagnostic insights into both adatom mobility between phase states as well as the microstructure evolution between phase states. The stress generators created by the phase changes are nominally linked to the volumetric change created by the new phase and/or the interfacial strains resulting from the new phase in contact with either other phase(s) or the substrate. In this section, a few highlights of stress dependent responses in phase changing films are given to illustrate how film stress has been employed as an investigative response into understanding mechanisms of thin film stress evolution.

In the recent works by Li *et al.* [184,185], the growth stresses for the hexagonal close packed (hcp) to body centered cubic (bcc) Ti phase transformation was monitored as the Ti film

grew. The Ti was deposited in a multilayer stack using two different bcc template layers – Nb or W – to determine the effect of the template bcc lattice matching on the stabilization. In each report, the Ti layer thickness equaled that of the bcc template layer. For the Ti/Nb multilayers,[184] the bcc Ti was stabilized up to 2 nm after which it reverted to its bulk hcp phase with further increases in thickness. This bcc Ti phase is equivalent to its bulk high temperature β-Ti phase. By extrapolating the β-Ti lattice parameter to room temperature, it was found to be 0.327 nm, which was very similar to that of the bcc room temperature Nb parameter of 0.330 nm. The close matching resulted in a coherent interface. As the Ti layer initially grew on the Nb layer, the stress-thickness revealed a slight tensile (or positive slope) condition (Figure 12). This stress response was associated with the tensile strain that occurred as the bcc Ti lattice matched the slightly larger lattice spacing of the Nb layer. At approximately 2 nm of Ti growth, the stress-thickness slope transitioned and became negative or compressive, also shown in Figure 12. Using post mortem electron diffraction of the multilayers, this thickness corresponded to the change from bcc to hcp Ti.

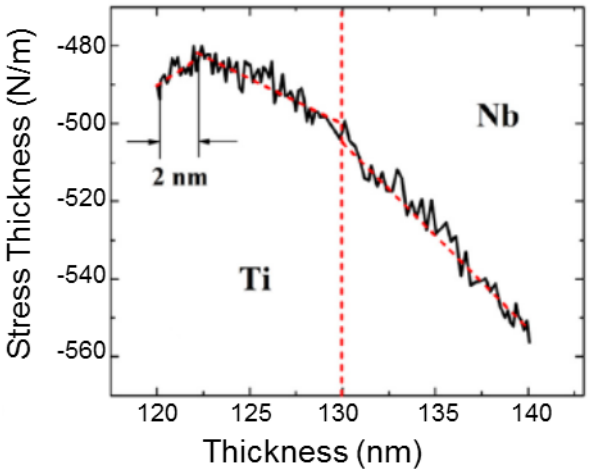

Figure 12: In situ growth response of Ti on Nb. Note the slight positive or tensile stress response of Ti up to 2 nm where upon it transitions to a negative or compressive stress for larger layer thicknesses. This thickness represented the change from bcc to hcp Ti. Figure adapted from Ref. [184].

In comparison, when Ti was deposited onto the bcc W template layers in the Ti/W multilayer, a different stress response was observed.[185] Unlike Nb, W's lattice parameter of 0.316 nm provided a significant strain that consequently reduced the Ti layer's stabilization to being ~1 nm. During Ti's growth, the stress thickness was found to exhibit a very steep (negative) slope gradient over the first ~1nm. This was associated with the bcc Ti being under compression in an attempt to match the W template. Ti's transformation to hcp Ti after 1 nm retained the compressive stress state but the stress in the thicker regime was less compressive, indicating some stress relief with the transformation. In both examples, the *in situ* stress measurements provided real-time diagnostics of the phase changing behavior of the growing film.

Beyond polymorphic crystalline phase transformations in multilayers, amorphous to crystalline transformations (or crystallization) have also been observed. For example, Mo/Si multilayers used for X-ray optic mirrors, can stabilize an amorphous Mo layer up to a thicknesses of ~ 2 nm.[186] This amorphous stabilization can be extended by alloying Mo with Si. Fillon *et al.* [41] provided a nice summary of this stabilization in relationship to the stress dependence for a series of $Mo_{1-x}Si_x$ films. For $x < 0.15$, a tensile stress was found to develop after ~3-5 nm of growth with this tensile stress gradually levelling out; for $0.16 \leq x < 0.19$, a large tensile stress developed after ~13-20 nm of growth which was subsequently retained; and for $x \geq 0.19$, the stress state rapidly became compressive after ~ 3 nm. Each of these stress states were found to correspond to the phase state of the film. For $x \geq 0.19$, the films were amorphous whereas compositions below this value were related to a critical thickness-dependence for an amorphous-to-bcc solid solution transition. The authors explained the critical thickness dependence in terms of volumetric and interfacial energy descriptions for stabilization, which has also been developed for polymorphic transformations.[187] These stresses would then be related to the volumetric strains that would accompany the

crystallization of the film. What was intriguing in their findings was that the largest tensile stresses corresponded to the largest grain sizes. In polycrystalline films, the attractive forces at the GBs are nominally inversely proportional to the grain size. To explain this potential conflicting issue, the authors correctly pointed out that these films do not initially grow polycrystalline but are amorphous, and the stresses dominated by volumetric changes from the transformation would propagate as elastic strains as the film thickens. Thus, their findings emphasize prior sections of this review concerning microstructure-stress relationships as well as expanding those in recognition of the influence of a phase transformation on the stress response. Recently, this scenario of a spontaneous, compositional- and thickness-dependent crystallization process in $Mo_{1-x}Si_x$ alloys was confirmed by combining *in situ* and real-time wafer curvature, XRD and X-ray reflectivity experiments simultaneously during thin film deposition.[188] Data reported in Fig. 13a show that the sudden tensile rise that manifests above a certain deposition time is concomitant with the rapid increase of the integrated XRD intensity (Fig. 13b) of the bcc (110) peak for $Mo_{1-x}Si_x$ alloys with Si content $x \leq 0.20$. This crystallization is also accompanied by a sudden increase of surface roughness (Fig. 13c), which continues during later growth. A significant delay in the amorphous-to-bcc solid solution transition is observed when the Si content approaches a critical composition, x~0.20. For x=0.20, this critical thickness is found to be ~10 nm. The film with x=0.25 do not exhibit any phase transition with deposition time and grows persistently in an amorphous state, with a slight compressive stress and smoother surface. From a simulation of the temporal evolution of the XRD integrated intensity (Fig. 13b), the propagation velocity of the crystallization front was found to be ~13 nm/s, highlighting for a relatively fast process. This is, however, several orders of magnitude lower than what usually takes place during laser-induced or metal-induced explosive crystallization (EC) of *a*-Si and *a*-Ge (velocity on the order of cm/s to

m/s).[189–191] Noteworthy, the initial stress state of precursor *a*-Si films is suggestive to influence the EC mechanisms and resulting grain sizes of the formed poly-Si films.[191]

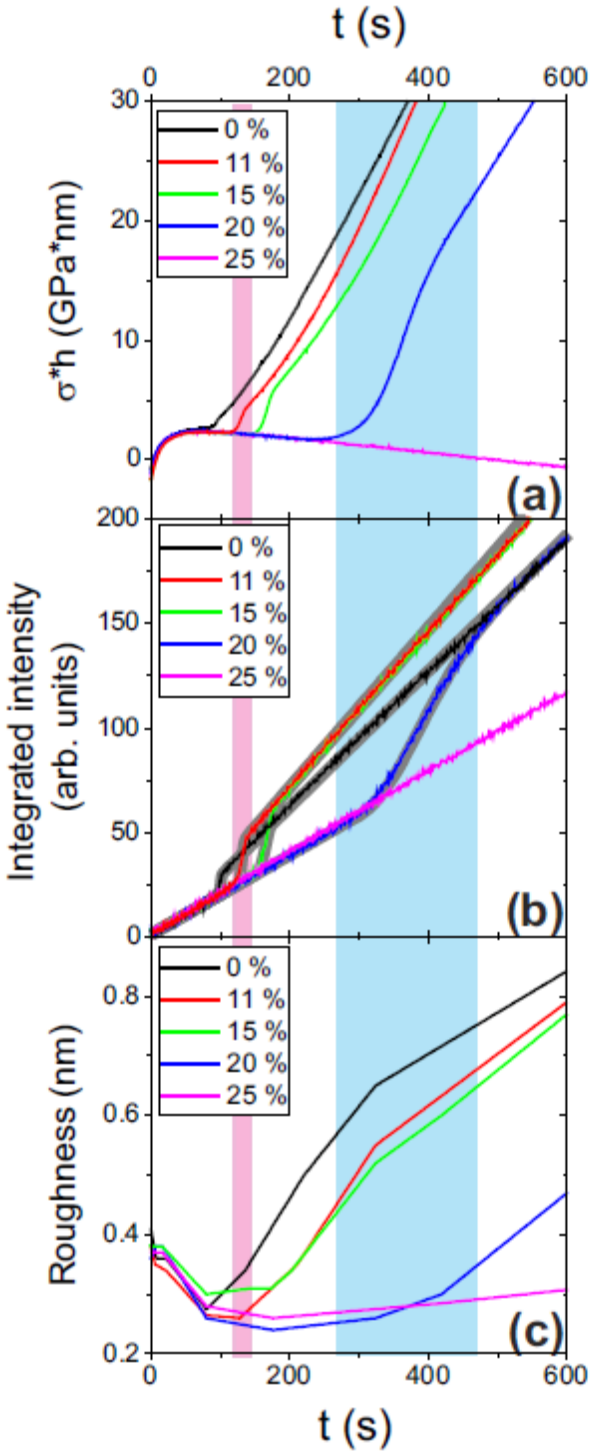

Figure 13: Time-dependent evolution of a) the stress thickness product measured by MOSS, b) the integrated XRD intensity of the (110) peak, and c) the surface roughness determined from XRR, during sputter-deposition of $Mo_{1-x}Si_x$ alloys.[188] Reprinted with permission from ACS Appl. Mater. Interfaces 8, 34888 (2016). Copyright 2016 American Chemical Society.

Similar crystallization stress state studies have been investigated in amorphous Te-based alloys, which are potential phase changing materials for optical data storage. In the work by Leevard Pedersen *et al.*[192], a series of *ex situ* heats were conducted where the stress associated with the onset of crystallization was monitored during the annealing. The authors noticed that the observed stress accounted for only ~9% of what would be computed from a purely elastic crystallization reaction. Further stress relief noted in the films were then associated from the plastic flow in the amorphous phase. Moreover, the stress relaxation rate after crystallization was found to be minimal, suggesting to the authors that inelastic stress changes must be accommodated by viscous flow in the amorphous phase. Thus, from these phase changing stress studies, the authors concluded that a small volume change and a small elastic modulus would be preferred in a phase changing optical device film if one is to avoid extensive stress accumulation from the accompanying viscous flow that occurs upon crystallization.

Beyond internally induced stresses from a phase transformation, film stress dependent phase changes can also be influenced by external processing variables such as temperature and deposition method. In the work by Clevenger *et al.*[193], the tetragonal β to cubic α phase change in Ta films were investigated. In their experiments, 100 nm thick Ta films were grown in both a tensile and compressive stress states dependent on deposition method - evaporation or DCMS, with the sputtered films further modified by varied pressures and RF substrate bias. With the variety of Ta films deposited, they were heated up to 850^{o}C at 10^{o}C/min under purified He with the stress monitored during the annealing by a wafer curvature method. The β-to-α Ta phase transition occurred over a range of temperature between 600-800^{o}C, with the onset of the transformation strongly dependent on the initial film's deposition process conditions. This β-to-α phase change was noted to be the main stress relief mechanism for the

Ta films and was most pronounced in the intrinsically compressive stress states. Incomplete compressive stress relaxation was observed if the film was initially deposited in the α-phase state or if the β-phase only partially transformed.

Thin films of NiTi, commonly referred to as the Nitinol shape memory alloys, provide a unique study of a phase changing material that can be cyclically iterated between two distinct phases. Such materials are candidates for micro-electro-mechanical-system (MEMS) applications. Fu *et al.*[194] have reported how variations in processing conditions and Ti content can alter this phase dependent stress response for a series of Nitinol based films. In their paper, they varied the sputtering deposition pressure and Ti composition and linked these variables to the phase changing stress response via *ex situ* annealing. At the lowest sputtering pressure (0.8 mTorr), the films exhibited compressive stress states which were associated with the sputtered atoms having lost minimal kinetic energy from a reduced number of collisions with gases in the vacuum chamber. These conditions contribute to enhance atomic peening and adatom mobility during growth, as discussed previously in Sec. III-A. With increasing the sputtering pressure (3.2 mTorr), the films became tensile which then decreased with an ever increasing film thickness >250 nm or films deposited at even higher pressures (10 mTorr). These reduced tensile stress states were rationalized to various relaxation mechanisms within the microstructure of the evolving film.

In each film, the as-deposited TiNi film state was noted to be amorphous. Upon annealing the films up to ~ 130^{o}C (400 K), they each exhibited an evolution towards an ever increasing compressive stress condition where upon the stress then reverted towards either tensile direction (for the 0.8 mTorr film) or relatively invariant stress evolution (for the 3.2 mTorr film) during densification of the films' microstructure (Figure 14a-b). Upon crystallization, a notable slope change was observed in the films stress state, which then readily became compressive (negative slope) with increasing temperature. Cooling the films from ~630^{o}C

(900 K), the stress reverted towards a tensile stress state and the shape memory austenite-martensitic transformation became readily apparent as an abrupt reduction in stress below 400 K, also shown in Figure 14a-b with appropriate phase transformation identifiers labeled within the figure. These changes in stress relief provide clear indications of a phase-dependent stress behavior for alloys whose composition does not change but undergo either a crystallization or a diffusionless shape memory transformation with temperature.

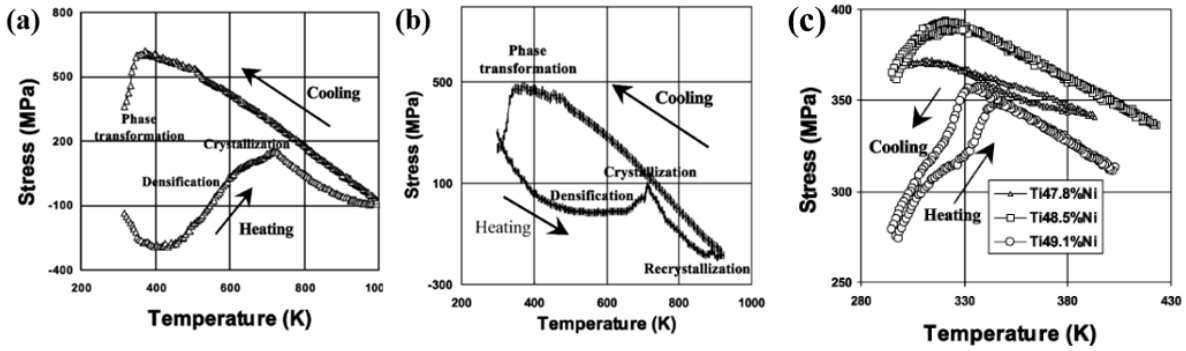

Figure 14: The stress versus annealing behavior under various transformations (a) NiTi film grown at 0.8 mTorr (b) NiTi film grown at 3.2 mTorr and (c) for different compositions of NiTi films.[194] Reprinted with permission from Surf. Coat. Technol. 167, 120 (2003). Copyright 2003 Elsevier.

The stress state associated with this shape memory transformation was also found to be composition-dependent (see Fig. 14c). For films that were 47.5 at.% Ti, a small change in the stress evolution curve was observed suggesting that the martensitic transformation was not significant. When the films were 48.5 at.%Ti, the shape memory transformation did increase, which resulted in an increase in the recovery stress upon the martensitic-austenitic transformation. But the heating and cooling stress curves did not converge to the same temperature-stress levels at ambient temperatures, leading to a partially closed hysteresis loop. This separation was suspected to be associated with an additional R-phase transformation in the shape memory effect; the R-phase is an intermediate structure between the high

temperature, high symmetry austenite structure and the low temperature, lower symmetry martensitic structure. Upon increasing the Ti content to 49.1%, a two-step transformation was clearly observed upon heating and cooling and is considered clear evidence of this R-phase transformation. Once the film composition became Ti-rich, i.e. 50.2 at%, the two-step transformation was not present, the stress vs. temperature heating and cooling loops were closed, and the films exhibited a perfect shape memory transformation. Further increases in Ti content decreased the martensitic transformation temperature but with only a partial relaxation of the stress states that were observed at the prior Ti-rich compositions.

The study by Shen *et al.*[195] compiled many of the characteristics described above but in a single system which undergoes a composition-dependent phase state - stress dependent relationship. In their work, reactive sputtering of W in $Ar+N_2$ atmosphere was undertaken to produce WN_x films. It was found that N concentrations less than 8 at.% retained a bcc solid solution phase, whereas increasing the N content between ~12 to 28 at.% vitrified the W film. If the N content reach ~ 32 at.%, the film again crystallized as the intermetallic W_2N. In all cases, the films were compressive; however, the stress decreased as the N concentration increased, with the lowest value being an amorphous film at a concentration of ~ 20 at.% N. These structural changes were rationalized to be pressure-dependent variations in the mixed $Ar:N_2$ gas ratio used during sputtering. The gas mixture, at a fixed sputtering pressure of 6 mTorr, appeared to influence the average energy of the species bombarding the film during deposition. This impacted the microstructure and corresponding residual stress response. As the N content increased, the columnar microstructure noted in the solid solution W films transitioned to a disordered amorphous network that promoted a loss in intercolumnar coupling and increased porosity in the GBs. These phase changed microstructure alternations facilitated the observed relaxation of the compressive stresses.

In some cases, the phase transforming stress is a result of intrinsic impurities that cause a phase transformation. In the very early stages of W film growth, the nominally bcc phase can adopt a A15 structure, called β-W in the literature.[196–199] Kaub and Thompson[200] have shown that small amounts of Ti solute coupled with *in situ* annealing during deposition will change the thickness stability and the magnitude of the initial stress state for A15 W. They suggested that the Ti reacts with the residual oxygen in the film which has been suggested to facilitate the stability of bcc W. APT confirmed a higher presence of titanium oxide complexes in the mass spectrum providing evidence to support this notation that oxygen is likely regulating the phase stability of A15 W and by controlling its reactivity with W, the phase transformation is manipulated. Thus, alloying, in this case, is not necessarily controlling the stress state from a reaction between the solvent and solute species but rather a means to control impurities in the system responsible for phase transformations.

A concluding comment is made concerning intermetallic ordering in phase changing films and their phase-stress responses. Very much like the martensitic transformation of NiTi, where the composition does not change, an ordered intermetallic film (where the atoms reside in specific lattice sites) can have an equally pronounced effect on film stress. In the work by Fu *et al.* [40], a series of FePt thin films were sputter deposited at various *in situ* deposition temperatures to promote the solid solution A1 to ordered intermetallic $L1_0$ phase change. It was found that upon increasing degree of ordering, the film's compressive stress was reduced. Nominally, an increase in deposition temperature would promote higher mobility and potential microstructures that would increase the compressive stress. This deviation in behavior for the chemically ordering film was contributed to the adatoms becoming less mobile as they adopted their thermodynamically preferred lattice registry sites in the growing film. Even more interesting was the stress relaxation response that occurred with growth interruption (or, in other words, how the stress evolves with time after deposition ceases). As

the film increased in degree of chemical order, the rate of compressive stress relaxation dramatically increased. One could assume a film with a higher compressive stress would be biased for greater stress relaxation. In contrast, the opposite was noted as the least ordered films were the most compressive. The rapid stress relaxation noted for the ordered films was contributed to these ordered films having an additional chemical potential contribution to bias the stress relaxation according to the model proposed by Chason *et al*.[65,140]

Phase transformation, whether polymorphic, crystallization, order-disorder reactions, etc. have a dramatic effect on the stress evolution of thin films. These transformations result in varied stress relaxation mechanisms and insights into the mobility responses of the adatoms involved in these changes. The phase transformations offer stress relieving mechanisms that will change the mechanical attributes of the films that contain them. Through this brief section's overview, a few highlights have been given to illustrate how thin film stress evolves under a variety of phase transformation types and how residual stress measurements offers a very valuable diagnostic tool for investigating such phase transformations and their influence on mechanical responses.

C. Stress gradients and texture development

The structure-stress dependences in nanocrystalline thin films were discussed in previous sections mainly with respect to the variation of grain size, fraction of GB and growth kinetics/energetics. The film microstructure can also evolve with respect to the orientation of the grains, so that the influence of texture development on stress gradient has to be considered.

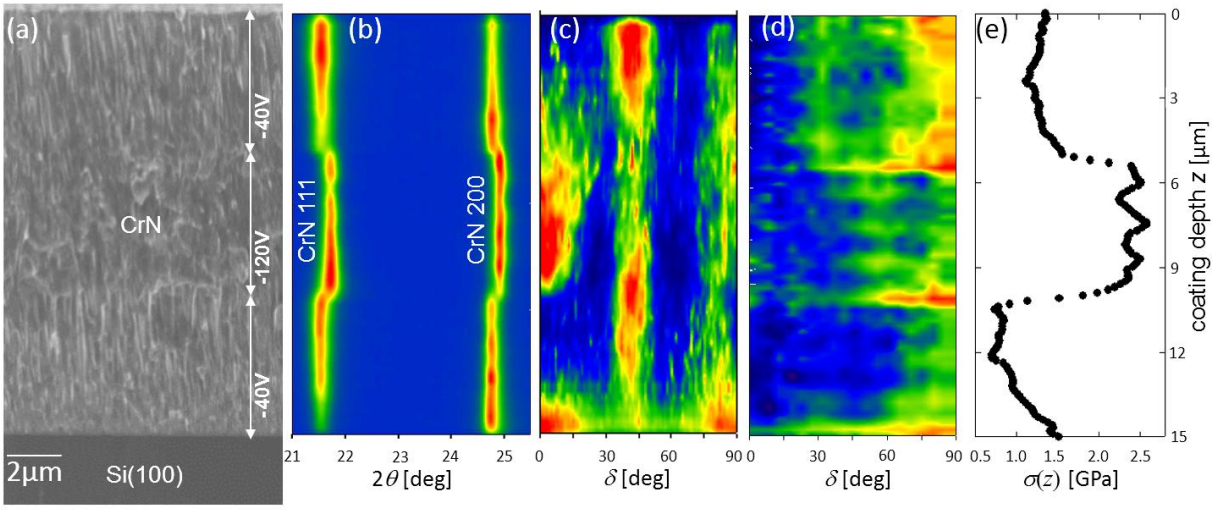

Figure 15: Experimental results collected using cross-sectional X-ray nanodiffraction approach from a 15 µm thick CrN nanocrystalline coating on a Si(100) substrate.[96] (a) SEM image from the film deposited at bias voltages of −40 and −120 V. (b) Diffraction scans collected at different depths reveals the presence of three sublayers with different lattice parameters and crystallographic texture gradient. A map (c) of diffraction intensities for CrN 200 reflection demonstrates smooth transitions of fiber textures across the coating. FWHMs of CrN 111 reflection (d) demonstrate the complex microstructural development with three nucleation zones. Coating depth dependent in-plane residual stresses (e) correlate with the microstructural evolution (a-d) and process conditions.

In Figure 15a-e, results from cross-sectional X-ray nanodiffraction analysis on a 15µm thick CrN coating deposited on Si(100) substrate using MS in an Ar+N_2 gas mixture at a temperature of 350°C using a sequence of three bias voltages of –40, –120 and –40 V are presented.[96] Three consecutive CrN sublayers, each 5 µm in thickness, were deposited by varying the energy of incident ions and without interrupting the film growth. In Fig. 15a, a SEM micrograph of the film cross-section demonstrates the film morphology with three sublayers and needle-like crystallites in the top and bottom sublayers. In Fig. 15b, diffraction intensity plotted as a function of Bragg's angle 2θ is plotted. The data were obtained by integrating the Debey-Scherrer rings in the δ range of 80-100 deg. (Fig. 2). The results indicate that the middle region of the monolithic CrN coating possesses different lattice parameter as other two sublayers. The variation of the intensity documents that the texture of the film changes as a function of the thickness. In Fig. 15c, a variation of the diffraction

intensity along the Debye-Scherrer ring of CrN 200 reflections documents that the coating grows in the near-substrate regions with CrN (100) planes oriented parallel to the coating-substrate interface and that this preferred orientation changes with the distance from the substrate. In Fig. 15d, a variation of Full Width of Half-Maximum (FWHM) of CrN 111 reflection is presented. At the interface region, large FWHMs values indicate a presence of small crystallites and/or a presence of strains of second and third order. At a distance of ~3μm and more from the interface the small and the large FWHMs for $\delta \cong 0$ and $\delta \cong 90$, respectively, indicate a presence of anisotropic crystallites elongated along the surface normal. At a depth of ~5 and ~10μm, when the bias changed, one can observe an increase of FWHMs indicating the presence of small crystallites and/or a large amount of crystallographic defects which can be interpreted by nucleation process.

Finally, in Fig. 15e, residual stress dependence in the coating evaluated using Eq. (10) is presented. At the interface, a relatively large compressive stress of ~1.5 GPa in the coating nucleation region can be explained by the presence of small crystallites and large density of GBs, which dominate the microstructure and allows for generation of structural defects during the film growth. When the film grows the magnitude of the compressive stress decreases and then saturates at a depth of ~10-12 μm. The decrease and the saturation can be explained by the gradual evolution of V shape grains and the decrease of GB density. When the bias changed from −40 to −120 V, at a depth of ~10μm, ion bombardment with more energetic particles leaves a higher fraction of residual radiation-type damage in the form of clusters of point defects (mainly interstitials) and/or trapping of atoms at GB sites, as discussed in Sec.III.A.2, resulting in compressive stress of a higher level (~2.5 GPa). After the bias was changed again to −40 V, the stress decreased and saturated because of microstructure saturation.

The results in Fig. 15 indicate a very complex nature of microstructure and stress evolution in the coating, which is due to self-organization phenomena as well as process parameters. The results in Fig. 15 were obtained from one scan lasting less than two minutes and document the possibility of cross-sectional X-ray nanodiffraction to correlate residual stress gradients with microstructural evolution and process parameters.

IV. Stress in engineering coatings and coating systems

Fundamental studies on structure-stress interrelation and advanced measurement methods have become fundamental tools for the understanding of materials performance in real-life industrial environments. In fact, the accurate knowledge of residual stress distributions at multiple-length scales (from macro- to nano-) can be extremely relevant to better understand the mechanical behavior and reliability of micro-systems and thin films in practical applications.

In the following sections (IV-A to IV-D), a series of industrial applications is presented, where the importance of residual stress control and monitoring, and the correlation between residual stress and in-service performance, are highlighted and discussed with specific reference to previous sections. In particular, we present selected examples from the areas of microelectronics, optical coatings, coatings on plastics, and tribological coatings for aerospace. Although more examples from other fields, such as health and energy, could also be shown, the following considerations and case studies are highly relevant in order to highlight the main and effective strategies to tailor intrinsic stresses in coatings, with specific reference to different coating/substrate combinations as presented during the 2016 Stress Workshop.

We also provide in Sec. IV-E a brief synthesis of the most common stress generation and relaxation mechanisms in relevance to the case studies presented in this paper, and outline novel approaches to manage stress. Finally, Sec. IV-F presents our current understanding on crack initiation in stressed layers.

A. Stress in microfabricated systems

The promise that nanotechnology holds with respect to increased performance and reliability lies in the ability to utilize effects that naturally arise in structures with greater surface-to-volume ratios. For example, the increased mechanical flexibility imparted by MEMS features by incorporating lithography with novel deposition and etching techniques have allowed for intricate and unique arrangements of materials and features, from metamaterials[201] to three-dimensional transistors[202]. These structures have both enabled new properties (negative indices of refraction) and have allowed us to greatly improve existing features, such as stronger electrostatic control in 3D field effect transistor (FET) designs. The presence of residual stress within such devices, resulting from manufacture or deliberate incorporation, can represent either an enhancement or a detractor to the overall performance, based on the mechanical response of the system. Tensile stress, typically observed in metallic features deposited on dielectric substrates, can be a detriment with respect to failure mechanisms associated with delamination or cracking, while compressive stresses can produce buckling.

These effects can be accentuated in complementary metal oxide semiconductor (CMOS) devices, where tensile stress in combination with diffusion of atoms due to high current densities by electromigration can lead to open circuit failures[203]. However, the piezoresistive effect found in many semiconductors[204,205] leads to an effective change in a material's mobility by altering its band structure based on the applied strain. In this way,

strain engineering, implemented over the past decade in CMOS technology, exploits the benefits of increased performance by tailoring the composite geometry and magnitude of strain within adjacent, stressor features. A number of strategies have been employed to generate strain within the current-carrying regions of devices. The deposition of heteroepitaxial stressor structures within recesses in the substrate on either side of a device channel, can be used to induce either compressive strain by using materials that possess a larger lattice parameter than Si, such as $Si_{1-x}Ge_x$[206], or tensile strain by incorporating materials with a smaller lattice parameter, such as $Si_{1-x}C_x$[207]. Liner films possessing large residual stresses can be lithographically patterned to generate stress concentrations near CMOS features, representing another scheme that has demonstrated increased carrier mobility[208] in the underlying semiconductor.

1. Characterization of residual stress through wafer curvature

Assessing the effectiveness of these approaches first requires a determination of the intrinsic stress that these stressor materials contain both before and after device manufacture. Standard characterization involves wafer curvature measurements performed on blanket stressor films deposited on Si substrates. Quantifying the corresponding residual blanket film stress (σ_B) relies on using the appropriate mechanical model that describes the elastic response of the layered, composite system. If the film and substrate are perfectly bonded and uniform in thickness, then the Timoshenko model[209] or the Stoney equation[28], in the case of film thicknesses much less than that of the substrate, can be used to extract film stress from the differences in curvature before and after film deposition. For a single-crystal substrate, its elastic anisotropy and crystallographic orientation affect the observed curvature due to elastic stress. Neumann's principle dictates that the symmetry of the crystal system must be present in the symmetry of the property, which is described by second-rank tensors for stress and strain[210]. For example, strain induced in Si (111) and Si (001) substrates, which possess 3-fold

and 4-fold symmetry, respectively, generate radially symmetric wafer curvature profiles. However, Si (110) substrates exhibit 2-fold symmetry and can support two independent radii of curvature. Because this substrate orientation has been shown to produce improved p-type device mobility in planar FET[211] and FinFET devices[212], it is important to properly analyze the anisotropic strain distributions and corresponding curvature in such substrates.

The intrinsic elastic anisotropy present in Si can result in a distribution in curvature as a function of in-plane angle even if the overlying film possesses isotropic stress. This effect is demonstrated in Figure 16, which depicts the difference in curvature of Si substrates with (001) and (011) orientations due to an overlying, 0.5 μm thick Si_3N_4 film. As can be seen, the residual stress of the amorphous Si_3N_4 film induces curvature displaying two-fold symmetry in the Si (011) substrate. The greater elastic stiffness along {011} produces minima in curvature ($-23.9\ km^{-1}$) relative to that ($-34.4\ km^{-1}$) along the more compliant {100} in Si (011), resulting in a difference of approximately 44% along these two principal directions. In contrast, a similar Si_3N_4 film deposited on a Si (001) wafer induces a radially symmetric curvature of approximately $-36.9\ km^{-1}$ even though the in-plane elastic stiffness within (001) varies by approximately 30%; it is the symmetry of the wafer's crystallographic orientation that dictates distributions in curvature. Comparisons to an analytical model developed for arbitrary orientations within elastically anisotropic thin films and substrates[213] allow for a quantification of Si_3N_4 film stress of 1.19 GPa and 1.14 GPa on the Si (001) and (011) substrates, respectively.

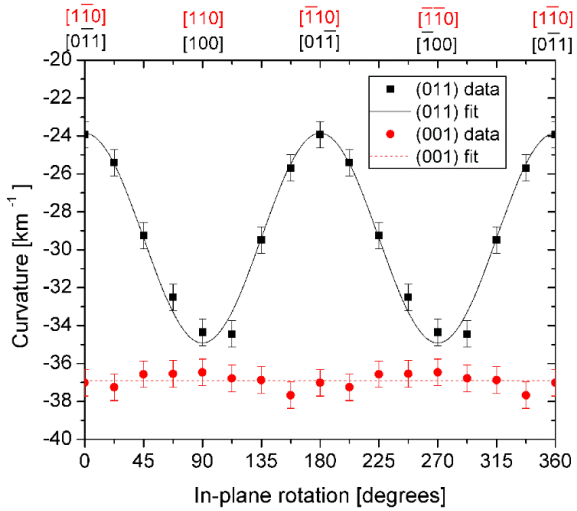

Figure 16: Comparison of measured curvatures induced in Si substrates of different crystallographic orientation by blanket silicon nitride films to calculated values.[213] The Si (011) wafer possesses two independent radii of curvature, where greater curvature is exhibited along the more compliant direction {100} than along {011}. Reprinted with permission from J. Appl. Phys. 104, 103509 (2008). Copyright 2008 American Institute of Physics

2. Stress distributions in CMOS features

While wafer curvature measurements provide data on the stress state within blanket stressor films that provide the driving force for elastic deformation, it is necessary to employ techniques with greater spatial resolution to assess strain distributions that arise within and near CMOS devices. Several approaches have been applied to this task, including micro-Raman microscopy[214,215], TEM[207,216], and synchrotron-based microdiffraction[217,218]. Micro-Raman spectroscopy measures stress indirectly through a correlation of phonon frequency shifts to those for samples with a known stress state (uniaxial, biaxial, etc.). However, laser-induced heating of the sample can artificially induce such frequency shifts[215], particularly in silicon-on-insulator (SOI) layers. TEM-based techniques clearly require significant sample preparation to produce electron-transparent specimens that can also modify the original stress state in the features under investigation. Among the techniques that allow for *in-situ* measurement of strain at a submicron scale, synchrotron-based x-ray microbeam diffraction is best suited to determining the elastic strain tensor components.

Strain fields in SOI regions underneath Si_3N_4 stressor features have been shown to extend up to 40 times the thickness of the stressor[219]. Figure 17a depicts a 0.84 μm wide, 105 nm thick Si_3N_4 feature deposited on a SOI substrate, in which the free edges of the feature induce stress in the underlying layers. Out-of-plane SOI strain was determined by measuring the change in the (008) reflection from the SOI region using an x-ray microbeam width of approximately 0.25 μm and a photon energy of 11.2 keV. Depth-averaged strain distributions within the SOI layer were compared to elastic simulations based on an anisotropic edge force model[220] and the boundary element method (BEM)[219] in Figure 17b. Fitting of the models to the observed strain profiles yielded a compressive stress value (σ_B) of –2.5 GPa in the unrelaxed Si_3N_4, equivalent to that found by wafer curvature measurements performed on blanket wafers. As shown in Figure 17b, the BEM model produces a better representation of the observed strain distributions and confirms the fully elastic strain transfer between the Si_3N_4 feature and SOI, though the sharp strain gradients near the feature corners are not captured by the measurements due to the finite size of the x-ray beam. The out-of-plane compressive strain underneath the Si_3N_4 stressor feature corresponds to in-plane tensile strain due to Poisson contraction, whereas the portions of the SOI outside of the feature possess in-plane compressive strain, which would correspond to the device channel regions. However, similar strain mapping across wider Si_3N_4 features revealed that the magnitude of strain induced in the SOI decreased with decreasing stressor width[221], signaling less efficacy in strain transfer for smaller device sizes. Micro-diffraction measurements performed on SOI device channels and adjacent, embedded $Si_{1-x}C_x$ stressor features show the elastic strain is also fully transferred[222] and suggest a more effective strategy as device dimensions decrease.

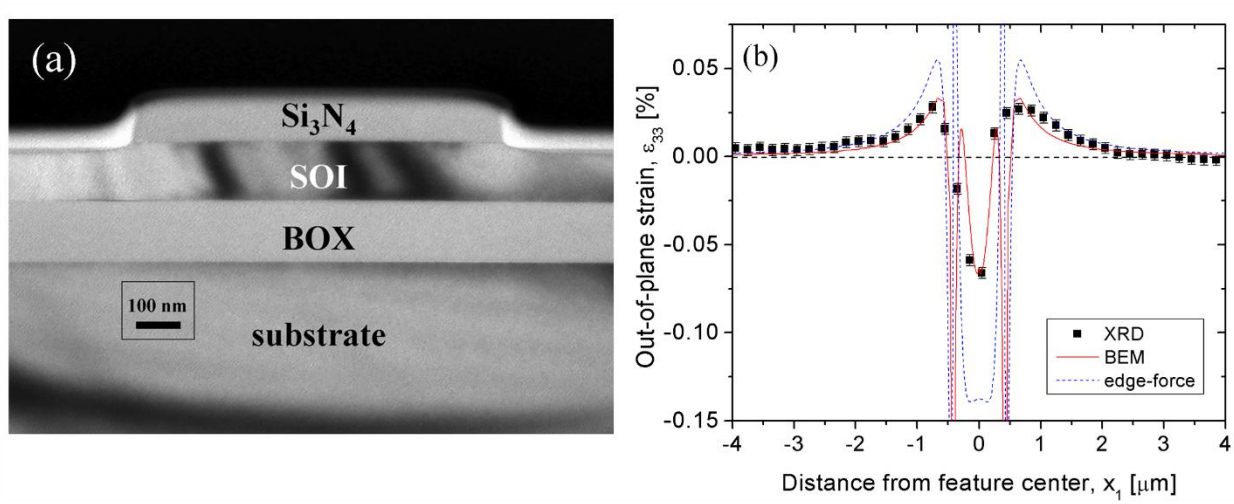

Figure 17: (a) Cross-sectional TEM image of 0.84 μm wide Si_3N_4 stressor feature patterned on a silicon-on-insulator (SOI) layer and (b) comparison of measured out-of-plane strain in the SOI layer as a function of position underneath the stressor feature to mechanical modeling simulations based on the boundary element method (BEM) and an anisotropic edge-force model.[221] Reprinted with permission from Thin Solid Films 530, 85 (2013). Copyright 2013 Elsevier.

3. Stress gradients within microelectronic metallization

A final example that illustrates the effects of stress in microelectronic technology is the presence of stress gradients within the metallization that provides power to CMOS devices. It has been known that large current densities within metallic lines can be sufficient to generate atomic mass flow, or electromigration, and ultimately create voids leading to open circuit failures[223]. Strategies developed over the past five decades to reduce diffusion paths within the interconnect microstructure involve incorporating select solute atoms that hinder flux of the metallization and minimizing the number of GBs that are aligned parallel to current flow. However, such approaches have not been effective at limiting the decrease in median lifetime of copper-based interconnects, which is halved in every new generation of CMOS technology, where device density is also doubled[224]. Novel capping layers have been explored to mitigate diffusion along the top surface of the metallization, a location that is highly susceptible to electromigration[225]. Capping films are required to limit oxidation and

impurity diffusion into interconnects during manufacture. However, the fabrication of copper metallization contains numerous processing steps that expose the interconnects to high temperatures. The mismatch in coefficients of thermal expansion between copper and the other materials that comprise the back-end-of-line levels can induce significant tensile stress in the metallization due to the thermal cycling. In particular, plastic deformation generated within the Cu can result in tensile stress gradients that can double the total stress near the cap / metallic film interface relative to the bulk stress in the film[226]. Because greater tensile stress can exacerbate voiding in interconnect structures, accurate measurement of stress distributions within these features is critical to understanding their vulnerability to electromigration.

Glancing-incidence x-ray diffraction (GIXRD) can be used to nondestructively probe strain gradients within metallic films[227–229]. By employing angles of the incident and diffracted x-ray beam with respect to the top sample surface close to the critical angle for total external reflection, we can control the depth to which diffraction information is collected, as already mentioned in Sec. II. B. Using the lattice spacings measured by GIXRD in combination with conventional d_{hkl} vs. $\sin^2(\psi)$ stress techniques for a particular *hkl* reflection, stress gradients that develop near the top surface of crystalline films can be quantified relative to the bulk, in-plane stress[230]. Figure 18b depicts the stress gradient extracted from GIXRD measurements using the (220) reflection from a 2.2 μm thick Cu film capped with a 25 nm $SiC_xN_yH_z$ layer, deposited at a temperature of approximately 350^0C. The constraint imposed by the overlying cap during such thermal excursions is responsible for a greater tensile stress near the cap / Cu interface relative to that deeper in the Cu film where plastic relaxation is more prevalent[226]. Although the stress gradients, $\Delta\sigma$, are collected as a function of incidence angle, it is important to transform these distributions to ones as a function of depth within the film.

In order to accomplish this, the distribution in x-ray beam intensity, which decreases exponentially with depth due to photoelectric absorption, must be deconvoluted from the measured shift in lattice spacing. However, difficulties in solving this inverse problem can result in significant error in obtaining accurate stress profiles[231]. To better illustrate this issue, we superimpose on the measurements in Figure 18b the predicted curves corresponding to two hypothetical stress gradients, as depicted in Figure 18a. One distribution assumes a constant value of $\Delta\sigma$ to a depth of 70 nm followed by an exponential decrease of the stress gradient (decay length of 39 nm) to the bulk stress value, while the other possesses a constant $\Delta\sigma$ that extends to a depth of 105 nm. Least-squares fitting was used to identify these dimensions as well as the maxima in the stress gradients, σ_0, of 125 MPa. Although the stress gradient distribution with an exponential decay exhibited a lower fitting error, both profiles indicate a depth in the range of 100 to 200 nm below the cap / Cu interface over which plastic deformation is affected by the overlying cap, and essentially overlap when plotted as a function of incidence angle (Fig. 18b), highlighting the challenges in finding a unique stress gradient.

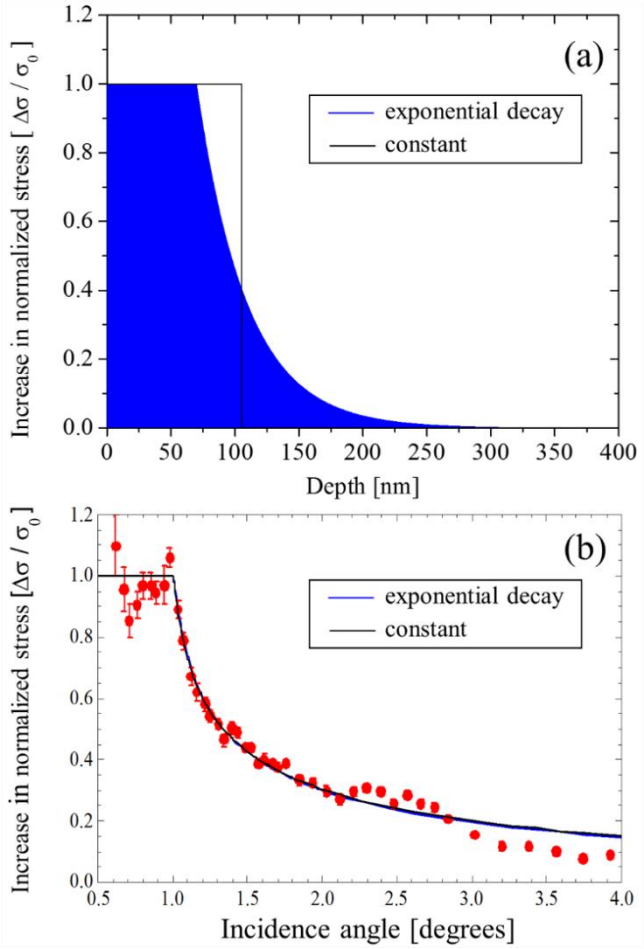

Figure 18: Stress gradients measured in a $SiC_xN_yH_z$ capped Cu film using GIXRD. (a) Two stress distributions displayed as a function of depth, where the parameters were determined by least-squares fitting of the (b) measured (220) x-ray reflection as a function of incidence angle.[230] Reprinted with permission from Appl. Phys. Lett. 104, 081920 (2014). Copyright 2014 American Institute of Physics.

4. Summary – stress in microfabricated systems

Strain distributions within microelectronic features influence many aspects of device performance, from increased carrier mobility to greater susceptibility to electromigration-based failure. Extracting stress distributions within these features through complementary techniques affords us a better understanding of how such distributions impact overall behavior, as well as how adjacent strain fields interact with each other as device density increases. With the introduction of more complex device geometries and smaller feature sizes, future characterization methods must be able to investigate all components of the stress tensor

in three dimensions within key regions of these features to ensure that strain in the entire composite can be properly tailored to enhance the key properties essential to these future devices.

B. Stress in optical coatings

Advances in the physics and technology of thin films have significantly been stimulated by their use in optical systems for numerous conventional and high-tech applications. This most frequently includes transparent dielectric optical coatings (OC) for optical interference filters (OIF) that are, in a broad sense, devices selecting a portion of the transmitted or reflected light, such as antireflective (AR) coatings, band pass filters, edge filters, hot/cold mirrors and others[11,54,232,233].

1. Optical coatings requirements

In order to qualify for optical applications, the following criteria should be respected when choosing the appropriate film material and film deposition process:[54]

a) The technique must allow good control and reproducibility of the complex refractive index $N(\lambda) = n(\lambda) - ik(\lambda)$. The wavelength ($\lambda$) dependence of the refractive index $n(\lambda)$ and the extinction coefficient $k(\lambda)$ is governed by the dispersion relations, which depend on the material's microstructure. In all OC applications, at least two basic materials must be available which possess high (n_H) and low (n_L) indices; they are frequently complemented by a third, medium (n_M) index material. A large ($n_H - n_L$) value may help reducing the design thickness and improving the performance of the OIF.

b) In most OC applications, materials are desired to be amorphous, isotropic, and with no birefringence, while keeping scattering below 10^{-4}.

c) The optical film must fulfill certain minimum mechanical requirements; these include (i) good adhesion, (ii) acceptable scratch-, abrasion- and wear resistance, (iii) high

environmental durability, (iii) acceptable stress (typically 0–500 MPa in compression), and (iv) absence of cracks and other defects.

d) The fabrication methods are frequently required to achieve good film thickness uniformity across the coated part (typically below 3%, or well below 1% for high-precision applications such as filters for telecommunications), and an acceptable deposition rate (about 1 nm/s).

Stress in thin films is closely related to the microstructure and packing density, which is a consequence of the fabrication process: in the case of (most frequent) amorphous dielectric OIFs, attractive forces within pores lead to tensile stress, while gas or vapor entrapment and its physi- or chemisorption in inner cavities or at GBs lead to compressive stress. In practical situations, the total internal stress, σ_{tot}, in OC is determined from bending curvature measurements: The curvature κ is obtained by capacitance, electromechanical, interferometric, and other measurements, usually using a circular plate or a cantilever beam, and σ_{tot} is then calculated from the Stoney formula, as described and discussed in detail in Section IIA.

In order to fully describe the behavior of OC in relation to the fabrication process as well as to the effect of environmental conditions and the conditions of use, σ_{tot} is usually expressed as (e.g., ref. [56]):

$$\sigma_{tot} = \sigma_{int} + \sigma_{therm} + \sigma_{env} \quad (24)$$

in relation to the intrinsic stress (σ_{int}), thermal stress (σ_{therm}), and the stress due to the sorption of gases and vapor from the surrounding environment within the pores and internal cavities (σ_{env}).

A classical example of the evolution of the total stress in the most typical optical film materials, namely SiO_2, during the fabrication cycle using evaporation is shown in Figure 19. During deposition, the total compressive stress increases with the increasing thickness. At the

end of the deposition cycle, the Meissner trap is degassed leading to partial filling of the film's pores, accompanied by a slight increase of the compressive stress. This stress further significantly rises due to the sorption of water vapor during venting, followed by a slow stress relief due to the microstructural relaxation[234].

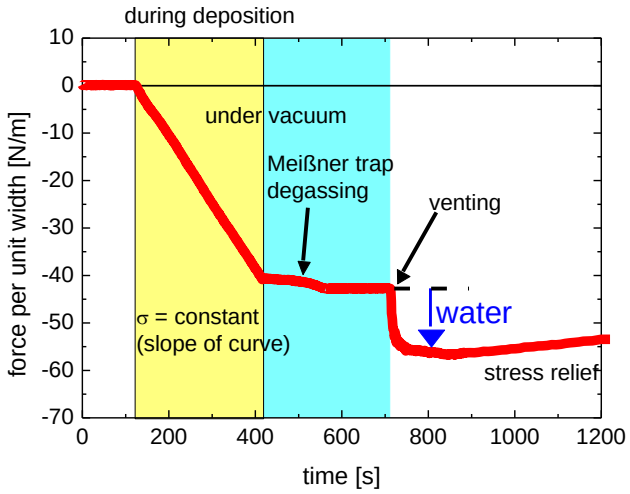

Figure 19: Variation of stress in a typical optical film (SiO_2) during the fabrication process consisting of EBE, degassing, venting, and exposure to the ambient atmosphere (modified after Ref.[234]).

The effect of water sorption has been studied in detail by Hirsch[235] who proposed a model in which the propensity to the accommodation of water molecules is related to the size of cylindrical pores and the adsorbent dipole moment. In relation to the water vapor sorption phenomenon, much of the effort in the field of OC has been devoted to the suppression of porosity by applying appropriate energetic conditions leading to high film packing density (see e.g., refs. [225,232,236]).

Since most of the OCs appear in the form of discrete multilayer stacks of n_H, n_L and n_M layers, it is generally accepted that the final stress, represented by the coating/substrate curvature κ, scales with the stress of individual layers σ_i weighed by the corresponding film thickness h_i (e.g., refs. [237,238]):

$$\kappa = \frac{6(1-\nu_s)}{E_s h_s^2}[\sigma_1 h_1 + \sigma_2 h_2 + \cdots + \sigma_n h_n] \qquad (25)$$

where ν_s is the Poisson ratio, E_s the Young's modulus, and h_s substrate thickness.

It has been demonstrated that the curvature method generally used for the assessment of the stress can also be effectively applied for the determination of the films' coefficient of thermal expansion (CTE or α_f) as well as of the Poisson ratio (ν_f) using the two-substrate method[239]. In this approach the film is simultaneously deposited on two different substrates (1 and 2) with their known (bulk) CTE (α_{s1} and α_{s2}), while assuming that the microstructures are the same. Taking into account the thermal stress for the two individual coating/substrate combinations[240]:

$$\sigma(T) = (\alpha_s - \alpha_f)(\frac{E_f}{1-\nu_f})(T - T_i) \tag{26}$$

where T_i is the initial temperature, measuring the variation of stress with temperature ($d\sigma/dT$) for individual substrates s_1 and s_2 can then be used to derive α_f and ν_f from the two following equations:

$$\alpha_f = \frac{\alpha_{s2}(\frac{d\sigma}{dT})_{s1} - \alpha_{s1}(\frac{d\sigma}{dT})_{s2}}{(\frac{d\sigma}{dT})_{s1} - (\frac{d\sigma}{dT})_{s2}} \tag{27}$$

$$\nu_f = \left(\frac{1}{E_r} - \frac{1-\nu_i^2}{E_i}\right)\frac{d\sigma}{dT}\frac{1}{\alpha_s - \alpha_f} - 1 \tag{28}$$

The only unknowns in the latter equation is the reduced Young's modulus of the film (E_r) that can be obtained from depth-sensing indentation measurements, while ν_i and E_i are the Poisson ratio and the Young's modulus of the diamond indenter. As an example, using c-Si and GaAs wafers with their known CTE values of $\alpha_{Si} = 2.6\times10^{-6}\ ^oC^{-1}$ and $\alpha_{GaAs} = 5.12\times10^{-6}\ ^oC^{-1}$, this approach yielded $\alpha_f = 4.9\times10^{-6}\ ^oC^{-1}$ and $\nu_f = 0.22$ for Nb_2O_5, $\alpha_f = 4.4\times10^{-6}\ ^oC^{-1}$ and $\nu_f = 0.27$ for Ta_2O_5, and $\alpha_f = 2.1\times10^{-6}\ ^oC^{-1}$ and $\nu_f = 0.11$ for SiO_2 obtained by dual ion beam sputtering (DIBS) (for more detail and references, see ref.[240]). More recently, this technique has also been applied for the assessment of the CTE and ν values of the novel hybrid (organic-

inorganic) optical coatings prepared by ion beam assisted chemical vapor deposition (IBA-CVD).[241]

A new *in situ* real-time approach to perform and analyze scratch tests in relation to stress in transparent coating/substrate systems has recently been introduced[242]. This method allows one to observe, in real-time, the contact region during the scratching process. As an example, thin TiO_2 layers exhibiting stress levels ranging from tensile to compressive were deposited by ion beam assisted deposition (IBAD) onto plastic substrates. Failure processes obtained using an increasing and a (novel) decreasing load scratch sequences were linked to the internal stress in the coatings allowing one to derive a stress management diagram and to evaluate the yield stress of the layers. Such an approach helped to enhance understanding of the OC failure mechanisms, but it also outlined a new pathway to increase scratch measurement reproducibility.

In the next section, we will discuss the relation between the fabrication techniques and the mechanical stress and stress evolution in OC.

2. Effect of the fabrication technique on stress in optical coatings

OC have traditionally been fabricated by PVD techniques from a solid source; this includes thermal and electron beam evaporation (EBE), MS, ion beam sputtering (IBS) and DIBS, and filtered CAD. Advances in low pressure plasma processing, and in plasma enhanced chemical vapor deposition (PECVD) in particular, have greatly increased the interest in PECVD for the fabrication of OC, while novel techniques such as atomic layer deposition (ALD) have also been considered.

As already mentioned above, considerable effort has been devoted to ensure film densification in order to obtain high packing density. This can be accomplished by increasing substrate temperature, $T_{s,}$ or by an appropriate control of ion bombardment energy, E_i ,

typically below 1 keV. The film microstructure obtained by such processes can be well described by the SZM, first proposed for evaporated metals[243] and for MS[25,244]. The SZM has then been revised by Messier *et al.* [245] who showed that T_s required for high packing density can be decreased by superimposed ion bombardment due to growth-related effects such as interfacial atom mixing, high surface mobility (diffusion) of deposited species, resputtering of loosely bound species, and deeper penetration of ions below the surface, leading to the displacement of atoms (forward sputtering or knock-in effects).[126] This has since been clearly demonstrated for OC and other coatings prepared by MS as well as by PECVD[11,54,236,246].

Different approaches have been used to quantitatively describe ion bombardment and its effect on the film microstructure and properties (see also Section III-B). It appears that a key parameter for describing such effects is the energy, E_{dep}, delivered to the growing film per deposited particle that, based on Eq. (19), can be expressed as $E_{dep} \sim E_i \, \Phi_i/\Phi_m$, where E denotes energy, Φ the particle flux, and indices i and m refer to ions and neutrals, the latter one including condensing precursor species. Generally, Φ_m can be experimentally determined as $\Phi_m = R \, \rho \, N_A/m_A$ where R is the deposition rate, ρ is the density, N_A is Avogadro number, and m_A is the atomic mass. These relationships are also reflected in the recent novel structure-zone diagram that includes the flux of energetic particles as one of the key parameters.[247]

Typical values of stress for the most frequently used OC prepared by PVD[56] and PECVD have been summarized[11,54]; they typically range from −500 to −100 MPa in compression for SiO_2, Ta_2O_5 and TiO_2, while they are around +400 MPa for MgF_2. Stress in PECVD optical films is generally lower compared to PVD. For example, using a dual-mode microwave/radiofrequency plasma for the deposition of SiO_2, $SiN_{1.3}$, SiON and TiO_2 films, the stress could be adjusted from tensile (around +200 MPa) to compressive (between −100 and −500 MPa), with zero stress values obtained for a substrate bias voltage of about −150V.[248] Such transition has been associated with the conversion of a highly porous

structure to a dense structure related to the energies required for the displacement of individual atoms constituting the film. This phenomenon has been explored for the fabrication of porous/dense single-material discrete layer and inhomogeneous layer (rugate) filters[249] that have been proposed as all-optical gas and vapor sensors.[250]

The performance of hard diamond-like carbon (DLC; *a*-C:H) films obtained from hydrocarbon gases or vapors under high energy ion bombardment has frequently been related to (and limited by) high residual compressive stress. Such high stress has been associated with the incorporation of hydrogen that is not chemically bonded, but it is physi- or chemisorbed on inner surfaces or trapped in the voids[251]. It has been shown that significantly lower stress values are obtained for high Φ_i/Φ_m ion flux ratios but lower ion energy, mainly due to an enhanced surface mobility and reduced sub-plantation[251], as also supported by MD simulations.[252]

Over the years, there has always been a debate about the effect of the deposition technique on the performance of OC, especially their optical and mechanical properties. In response to that Klemberg-Sapieha *et al.* [253] performed a systematic round robin study on the comparison of the most typical n_H and n_L OC, namely SiO_2, Ta_2O_5 and TiO_2 using PVD (IBAD, DCMS, HiPIMS, FCAD) and PECVD. It has been found that following optimization for the best performance (highest packing density), the optical properties were very similar (or almost identical), while most of the differences were in terms of the mechanical properties, such as hardness, Young's modulus and particularly stress (see Figure 20). It has been concluded that lower σ values are obtained at higher Φ_i/Φ_m values. This is also further supported by a recent study using reactive HiPIMS where the lowest stress for SiO_2 and Ta_2O_5 films compared to other techniques has clearly been demonstrated (see Figure 20).[254,255] In addition, multilayer OIFs, fully fabricated by HiPIMS were also found to exhibit significantly lower residual stress levels compared to single layers as well as to other

techniques, an effect accompanied by a substantially increased scratch resistance, and high environmental and long-term stability.

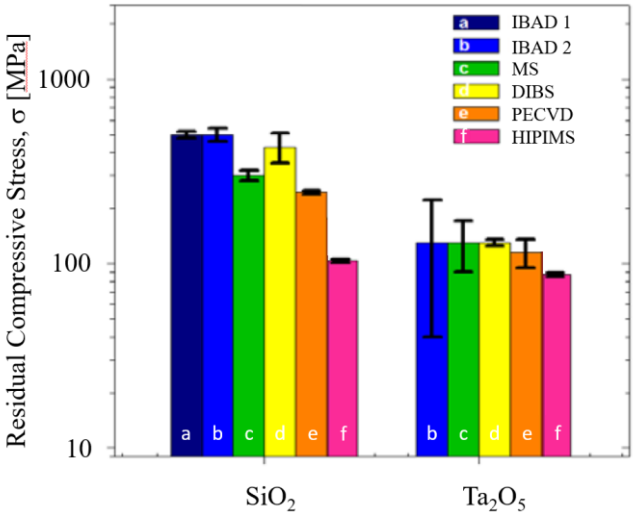

Figure 20: Comparison of (optimized) residual stress in low index (SiO_2) and high index (Ta_2O_5) films prepared by different complementary methods including IBAD, pulsed DCMS, DIBS, and PECVD (according to ref. [253]). The values for films prepared by HiPIMS are taken from ref. [254]

This is also in agreement with a study of the effect of E_i on Nb_2O_5 and Ta_2O_5 n_H films prepared by DIBS in which σ has systematically been compressive, but partial stress relaxation has been observed for E_i above about 250 eV.[240] This is in line with a model according to which the process of stress reduction consists of two stages (e.g., ref. [156]): (i) the atoms initially implanted in the film are in metastable positions, while (ii) some fraction of the incoming ion energy is transferred to those atoms, releasing them by a thermal spike from their metastable positions, moving them to a stable location.

3. Strategies to manage stress in optical coatings

The performance of OC systems and devices may be negatively affected by the deleterious effects of mechanical stress. In this section we discuss several strategies that allow one to decrease or compensate stress in the OIF applications, namely (i) use of new or novel

film materials, (ii) implementing minimum stress as a target in optical filter design, and (iii) multilayer stack release to obtain free-standing optical filters.

Application of inorganic OIF on plastic substrates such as in ophthalmic applications can be limited by the incompatibility of the coating and the substrate material due to a large difference in CTE, possibly leading to cracking, delamination and reduced durability. In this context, hybrid films have recently been proposed and explored,[241,256] fabricated by IBA-CVD, in which an organic precursor is introduced into the path of an ion beam. Such hybrid films have been found to possess optical properties suitable for OIF applications, while providing mechanical performance enhancement due to high mechanical flexibility, high hardness/modulus ratio, and high durability of the plastic optical components leading, for example, to decreased "crazing" (visible fracture patterns). In addition, such hybrid films are substantially less prone to water vapor sorption compared to their inorganic counterparts. This effect has important consequences on the σ_{env} contribution to the total stress as illustrated in Figure 21 demonstrated by a significantly reduced difference between the stress before and after venting, $\Delta\sigma$.

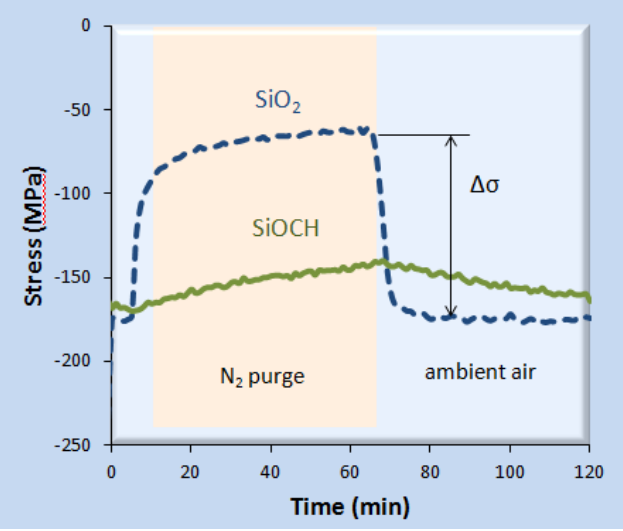

Figure 21: Variation of the total stress in two types of optical films (inorganic SiO_2 and hybrid silica-like organic-inorganic SiOCH) during the purge with dry nitrogen, venting, and exposure to the ambient atmosphere (after ref.[256]).

Excessive total stress in OIF can exhibit a negative effect on the performance of optical components such as astronomical mirrors due to substrate bending. This can be compensated by depositing equivalent film thicknesses on both sides of the substrate by taking into account the expression for the total stress of the OIF and for the individual layers.[257]

Recently, a new approach has been demonstrated that simultaneously considers both optical and mechanical targets in the OIF design[258]. Using a supplemental module in the OpenFilters open source design software (ref. [258] and references therein), each individual optical layer is represented by its refractive index (n_H, n_L) and by its stress. This combined optical/mechanical optimization and design technique has been experimentally validated by fabricating multilayer stacks using EBE, in combination with their mechanical stress assessment performed as a function of temperature. Two different stress-compensation strategies have been compared including (a) a design of two complementary OIFs on either side of the substrate, and (b) implementing the mechanical properties of the individual materials in the design of the OIF on one side only. This approach has been tested by the manufacture of a Fabry–Perot etalon used in astronomy; using evaporated SiO_2 and TiO_2 films, the substrate curvature could be decreased by 85% and 49% for the first and second strategies, respectively.

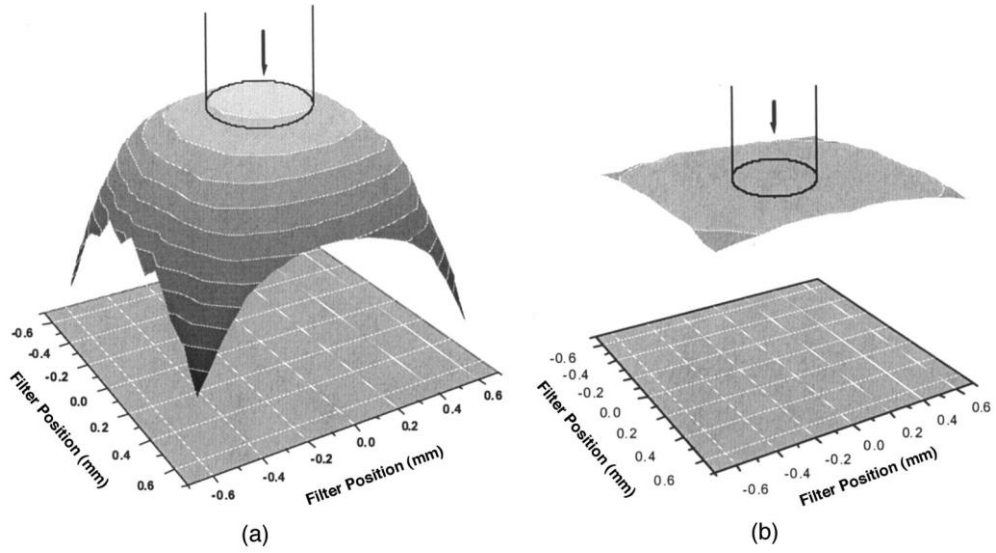

Figure 22: Spatial distribution of the central wavelength measured in reflection. The filter size is 1.4 mm x 1.4 mm. The vertical scale represents the shift of the filter's central wavelength: the contour lines are spaced at 0.2 nm. The cylinder on the top indicates the size of the light beam: (a) typical 100 GHz bandwidth filter produced with standard process, and (b) a 100 GHz filter fabricated with the ultra-low-stress process.[259] Reprinted with permission from Appl. Opt. 45, 1364 (2006). Copyright 2006 Optical Society of America.

OIFs have found widespread use in the fiber optic telecommunication industry. They must be thermally stable, exhibit excellent spectral performance, have low polarization dependence, and must be readily produced in high volume[260]. One of the frequent ways how to compensate stress is OIF annealing for stress relaxation[261]. However, when pushing toward an increased complexity of the fiber optic network architecture, more efficient components require more complex filters, which imply thicker coating designs and smaller final filter size. In such cases, coating stress at the edges of the filter is relieved through bending or distortion of the substrate, and the coating becomes thinner. The coating at the center of the filter retains a high stress condition, and remains thicker. The thickness difference leads to the central wavelength variation and the resulting passband width performance degradation.

As a remedy to the above problem, it has been proposed to release the coating after deposition and to reattach it to a suitable substrate, giving rise to an OIF with an ultra-low stress[259] (see Figure 22). Specifically, the OIF is first fabricated on a sacrificial substrate provided with a moisture sensitive surface. The coating is then released by scratching a small

part of the disc with a diamond tip: this causes moisture to penetrate to the NaCl layer and spontaneously (<100 ms) release the dielectric filter. The resulting coating flakes are flat and have sizes of up to 60 cm^2. Since these freestanding filters have a large thermal central wavelength shift (typically 9 pm/^oC), too high for telecommunication applications[260], the freestanding filter is then attached onto either a high-CTE glass or a stainless-steel washer with the appropriate CTE (see Figure 22). This process made it possible to produce high performance filters (200 GHz, 100 GHz, 50 GHz, etc.) with smaller physical dimensions, while maintaining or improving optical performance.

C. Stress in the coatings on plastics

The topic of stress in thin film-coated structures would not be complete without an examination of the specific challenges and opportunities of coating polymer components, many of which enable the light-weight, robust, mass-producible products that surround us. While the underlying physics is no different than stress-related issues at other interfaces and substrates, this section looks at particular systemic influences on stress for two popular polymer substrate configurations: roll-coated polymer webs and injection-molded polymers. The particular origin of stress-related issues is related to the inherent difference between the CTE of polymers compared to inorganic coatings by about two orders of magnitude, and the phenomena related to the complexity of the interfacial region (or "interphase") between the two materials.[55]

1. Stress on Roll-to-Roll – coated polymer webs

The mechanics of a coating on a thin polymer web (e.g., for a window film, as thin as a few micrometers) introduces significant application effects at stress levels that would be considered benign when compared to coatings on glass or other rigid substrates. As an

example, Stoney formula indicates a significant deflection of a 25 μm-thick substrate (with a Young's Modulus E = 4 GPa) with a 200 nm thick coating with a residual compressive coating stress of about 60 MPa, giving rise to a 50 mm radius of curvature. It is easy to see how such a deflection may affect the installability of a window film, for example, if there were not effective ways to mitigate it for a successful product. Similarly, it explains why brittle vacuum-deposited coatings on thin substrates can be quite prone to cracking, resulting in delamination or crazing defects if not designed properly.

The resulting effect on a products' utility can be quite severe, as the following examples demonstrate: Structurally perfect barrier coatings (such as those produced by ALD) based on dielectrics can crack under stress and create diffusion paths that diminish the barrier function; window films with brittle dielectric coatings can incur "crazing"; electrically conductive coatings may exhibit much higher sheet resistances due to micro-fractures; the permissible bending radius of films with high layer counts may be so large that it inhibits handling, installation or further downstream processing; high-k insulating films may incur reduced electric breakdown strength due to stress-induced micro-fractures. Therefore, understanding of the sources of stress and availability of the fundamental mitigation strategies for industrial applications are very important.

2. Sources of stress in coated polymer webs

While some stress-inducing mechanisms are the same as for any other substrates (nucleation / film growth effects, differences in CTE), polymer webs incur stresses related to web handling and due to the thermal (i.e., primary physical variable) conditions during the coating process[262]. A very common substrate for window film products is biaxially oriented polyethylene terephthalate (BOPET) which requires bulk processing temperatures below the "glass transition temperature" (T_g) of approximately 70°C to retain its dimensional and

mechanical characteristics. Coating at higher temperatures will generally (especially when unconstrained) induce shrinkage that was designed into the material during the stretching process, and thus impose compressive stress on any coatings. Predicting the behavior of releasing the shrinkage of a BOPET during a constrained (e.g., web coating) operation requires very thorough knowledge of the material's processing history and web coating conditions, and will complicate the resulting substrate/coating stress regime. While the CTE difference between polymers and typical vacuum-deposited coatings can be quite large, the stress influence is frequently relatively benign due to the small permissible temperature excursion.

BOPET is an example for a web substrate that is produced by extrusion of a molten resin through a die, and (if desired) subsequent stretching and heat-setting[263], and thus imparting heat-shrinkability functionality that is advantageous for many applications that require three-dimensional shape conformity. Some polymers (such as polyimide) require a different film manufacturing method utilizing casting from a solvent solution, while the casting process can significantly influence the structural and mechanical properties of the substrate[264]. Such films are typically not heat-shrinkable.

Another significant influence on coating stress during the deposition process is web handling. Polymer webs are elastic materials, and the high anisotropy of the web geometry and often of the web manufacturing process has significant implications on stress profiles. A web coater needs to maintain a certain tension (primarily for sufficient process cooling over a chilled coating drum, but also for other effects such as scratch control and roll formation), and the resulting elastic elongation in machine direction induces a constriction and thus compressive stress in the transverse direction. This non-isotropic stress/strain profile in the uncoated substrate will be superimposed with the coating stress induced by the sequential stages of coating formation, and can significantly affect the subsequent processability and

characteristics of use of the film (Figure 23). Processing of very thick films over small-diameter rollers may impart additional stresses onto the substrate and possibly the coating, and create complex load scenarios especially when real-life "noise" factors such as roller misalignment and web distortion are considered.[265]

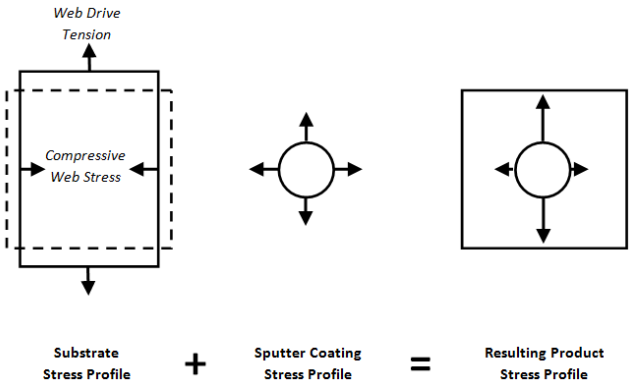

Figure 23: Qualitative composite stress profiles in roll-to-roll web coatings as a result of superposition of web-handling- and sputter-coating-induced stress profiles (example: compressive dielectric sputter coating).

Stress mitigation efforts in web coating often focus on balancing the deposition process conditions with the web handling constraints, and more complex filter stacks are often designed as dual-sided coatings (on both sides of the substrate) for sufficient stress compensation. Very elastic films that would incur high stress anisotropy during web handling may be coated with the assistance of a more rigid carrier film. In view of the limited thermal budget not only due to the melting temperature, but typically more importantly the T_g value of many polymer web substrates, this obviously eliminates classical high-temperature thermal annealing of a coating for effective re-crystallization for stress relief, so a post-treatment is generally not an option, and the stress mitigation must be accomplished during the deposition process itself. For some processes, it may be possible to decouple the thermal load of a coating process from the substrate by special annealing methods such as flash lamp annealing processes.[266] In multi-ply coating systems where the product is made from multiple layers of coated polymer films (e.g., high-end window film), the aforementioned effects of web

tensioning and additional coating processes (particularly wet-coatings using solvents, as for adhesives and hardcoats) and an appropriate product design and coating sequence can be successfully employed to produce stress-neutral product from quite stressy sub-components.[262] Nevertheless, the demands on production consistency and precise process control and process monitoring are very high to maintain high production yields.

A stress mitigation strategy may also be found in substituting brittle ceramic (dielectric) coatings with polymer or polymer composite coatings that typically possess a much lower modulus, and can conform better to distortions[267,268]. It has been shown that the crack onset value on many organic layers is above 12% as compared to 1% for many ceramic materials, which translates to a much higher tolerance for tight bending radii. The improved stress tolerance of such polymer-based thin films and coatings may also be an enabling characteristic for successful high-performance thin film barriers for flexible polymer devices such as organic light-emitting devices[269]. The approach of utilizing hybrid (organic-inorganic) layers is also a powerful stress mitigation tool for coatings on injection-molded polymer products, as is outlined in an example in the next section.

3. Stress in coatings on injection-molded polymers

The proliferation of high-end polymer optics relies on producing high-end coatings, especially for dielectric filters for anti-reflection, color correction, or other functional requirements. Coatings on polymers particularly benefited from the success of adding an anti-scratch coating onto lightweight polycarbonate ophthalmic lenses, and coatings have expanded from high-performance optical filters to low-cost/mass-produced anti-reflection and reflector coatings. Coating adhesion and durability are frequent requirements, especially in applications when exposed to harsh environments.

Compared to web coatings, the range of substrate polymers is much broader, but the most prominent materials groups are polycarbonate (PC, including the CR39 derivative, widely used for ophthalmics), polymethyl methacrylate (PMMA/Acrylic), Polystyrene, and copolymers (such as blends of acrylic and styrene, e.g., styrene acrylonitrile[270]. Other common specialty polymers for coated optics are polyetherimide ("Ultem®") and cyclo olefin polymers ("Zeonex®"). Polymers are selected due to their properties such as refractive index, spectral transmission, UV sensitivities, mechanical properties, thermal tolerance, molding process properties, cost, just to name a few.

High-end optical engineering polymers exhibit high compositional stability that is primarily mandated by the requirement of stable and predictable optical performance. In some low-cost polymers, oligomer migration over time can affect long-term interface properties. Oligomers are chain fragments or short monomer structures that may have considerable mobility and different physical properties compared to the bulk. They may occur as a side effect of injection molding, or can be intentionally added to modify bulk properties; for example, thermoplastics often contain ester oligomers as plasticizers to make them more impact-resistant. The issue with oligomer migration with respect to stress is that the oligomers accumulating at the component surface may act as a (largely unintended and uncontrolled) release layer that weakens the substrate-coating interface, and delamination can occur over time even though initial adhesion was quite sufficient. Similarly, additives such as flow enhancers or mold release agents may also be sources of interface "skins" that typically degrade the stress tolerance at the substrate/coating interface.

Most injection-molded polymers are compatible with a wide range of coating processes as long as thermal and chemical limitations are observed, and exhibit good adhesion properties that tolerate quite high stress levels[271]. PMMA, however, has been shown to be degraded by deposition process-related plasma radiation, resulting in poor adhesion and

requiring special coating methods[272]. Satisfactory coating adhesion on PMMA requires either a plasma-free vacuum coating process (such as thermal evaporation or IBAD) or the use of a radiation protection coating.

The molding conditions of a component have a major influence on the surface characteristics presented to a coating. During the molding process, the polymer is subjected to very high pressures, temperatures and often high shear rates that can significantly alter the component's chemical and mechanical properties from the bulk polymer resin, and especially the cooling profile (the outer skin solidifies first while the core is still in melt stage) and bulk geometry can introduce significant compositional material gradients that may vary on different areas even within the same injection-molded part. High-precision optical polymer components may be produced with injection compression molding, which greatly improves the fidelity of the optical contour to the mold, but also imparts higher stresses and relaxation phenomena[273]. Advanced mold design, flow modeling, and molding process control make it possible to control material variations, and the same conditions that support good optical properties of an injection-molded lens typically tend to provide uniform coating interface conditions for the functional surfaces, creating more predictable interface conditions for managing coating stress.

Another notable influence on coating stress in injection-molded parts can be the geometry which may induce large differences in the angle-of-incidence in directional coating processes. Different ones, such as MS, impart film thickness and sometimes film density non-uniformity on optics with high-aspect ratio contours, which affects the optical performance as well as the interfacial stresses at the film-substrate interface. The assumption here would be that the highest compressive stress levels (due to thickness and bulk density) would be at surfaces normal to the incident deposition flux, whereas off-angle geometry features exhibit lower density and lower thickness, and thus lower interfacial stresses. This can make the

design of stress-compensated precision optics more complicated. It is recognized that conformal deposition processes, such as PECVD[11,54] and lately, particularly ALD[274] present an attractive option to address this issue, although it remains to be seen whether the elevated deposition temperatures required for many of the attractive coating materials can be lowered to open up the application space of injection-molded polymer optics.

When it comes to the choice of coating material systems, particular improvement of the performance of antireflective stacks on plastic lenses has been demonstrated by implementing hybrid (organic-inorganic) layers in the optical stack.[241,256] It was demonstrated that such hybrid systems provide a significantly improved resistance to temperature- and humidity-induced stress variation due to a higher elastic recovery of hybrid (SiO_2-CH_x, ZrO_2-CH_x) coatings compared to their inorganic counterparts. Such coatings prepared by IBA-CVD show a higher thermal expansion (10^{-5} K^{-1}) close to that of polymer substrates (10^{-4} K^{-1} for CR-39), and a relatively high H/E ratio (up to 0.16), as well as high durability following accelerated environmental tests including exposure to high temperature/high humidity, UV and solar radiation, as well as a saline solution.

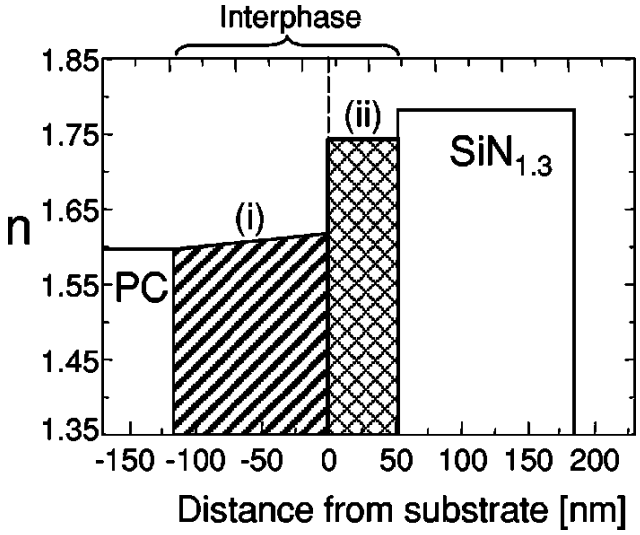

Figure 24: Illustration of a structured interfacial region (interphase) between a plasma deposited film (here $SiN_{1.3}$ and a polymer substrate (PC)). Schematic illustration of the $n(z)$

profile in the interfacial region shows: (i) a crosslinked layer formed by plasma pretreatment attributed mainly to polymer interaction with energetic VUV emitted light, and (ii) a transition layer obtained after $SiN_{1.3}$ deposition (modified after ref. [275]).

Important improvement in the performance of inorganic films on polymer substrates has been demonstrated by specifically tuning the surface reactions when applying plasma-based deposition techniques. Surface interactions involving energetic photons, ions, and reactive species (free radicals) have been found to lead to the formation of a physically thick structured interfacial region (interphase) between the inorganic coating and the plastic substrate (see Figure 24) [261,275]. Similar depth profiles have been observed for different combinations of materials, including SiO_2 and $SiN_{1.3}$ on PET, PC, PMMA, and other polymers[276]: The interphase has been found to be up to several tens of nanometers thick [275,277]; it consists of a cross-linked layer (region (i) in Figure 24), followed by a transition layer (region (ii)) formed by intermixing the growing film with the substrate materials, and possibly by voids. In the case of $SiN_{1.3}$ shown as example in Figure 24 and aimed for antireflective or barrier applications, *n* increases from 1.59 for PC to 1.80, while hardness increases by two orders of magnitude (from 0.2 GPa for bulk PC to about 2 GPa for the cross-linked surface layer, and up to 18 GPa for $SiN_{1.3}$). This inhomogeneity generally leads to a more uniform stress distribution at the interface, giving rise to better adhesion, tribological properties, flexibility, stretchability, and other functional characteristics suitable for coated plastics.

4. Summary – Stress in the coatings on plastic

Stress issues for coatings on polymers can lead to significant functional failures at relatively low stress levels compared to other, more rigid substrates. The manufacturing conditions for polymer web or molded polymer components can induce complex mechanical and chemical conditions at the coating/substrate interface, and for thin polymer webs, the coating may become a significant structural/mechanical component of the composite.

Successful stress management of coated polymer products depends on a thorough understanding of the interplay between material properties of the coating and substrate as well as the processing conditions, both during coating deposition as well as post-processing.

D. Effect of stress on the performance of tribological coatings for aerospace applications

Tribological coatings are employed to mitigate wear-related issues in a variety of aerospace components. The ability of coatings to meet the demands of specific applications depends many times upon the relationship between the internal coating stress and the applied contact stress. However, the relationship between stress and the tribological performance is not well understood. Yet, coatings are expected to achieve sufficient tribological performances, especially the components that experience high contact stresses. In order to illustrate this situation, in the following we describe three examples of critical applications where stress must be managed to obtain sufficient tribological characteristics, namely landing wheel bearings, rotorcraft gearbox components, and rotating elements in satellite guidance systems.

1. Landing gear bearings

Landing gears on aircraft are equipped with grease-lubricated, tapered roller bearings. Tapered roller bearings are designed to simultaneously accommodate high radial and axial loads[278]. Because of the differences between the inner and outer raceway angles, a force component is generated during operation that drives the tapered rollers against the rib face in a sliding contact.[279] At touchdown, the rotational speed of the bearings accelerates instantaneously from rest to accommodate the landing speed of the aircraft. Since the grease is usually very cold at the time of landing, the amount of lubrication from the bleed of oil out of

the grease is initially very small. When extremely large axial forces are involved in the landing, such as aircraft landing on the decks of aircraft carriers, very large loadings can be generated at the rib face/roller end sliding contact. Large contact stresses applied to a poorly lubricated, rapidly and highly loaded sliding contact brings asperities of mating surfaces (in this case the roller ends and rib face) into intimate contact and scuffing or galling type wear can ensue.

Currently, a metal-doped amorphous carbon coating is being used in some of these applications to reduce the risk of scuffing at the roller/rib contact of landing gear bearings. Specifically, the coating is a nanolaminate material consisting of nanocrystalline β-TiC precipitates in an amorphous carbon matrix, i.e., TiC/a-C.

Several application-specific requirements were considered in the selection of this coating. Because of the large shear stresses applied at the rib/roller interface during landing, the intrinsic (compressive) stress in the coating needed to be < 1 GPa, and therefore managed during deposition. The deposition process chosen to apply TiC/a-C was closed-field unbalanced MS[280], which is a process that can generate large argon ion fluxes (Φ) to the substrate during coating growth. The maximum temperature during deposition and the indentation modulus (Y') of the coating had to be compatible with the tempering point and elastic modulus of the steel, ~180°C and 210 GPa, respectively. To accommodate the shear stresses during the initial contact, the dry sliding friction coefficient of the coating was required to be small ($\mu \sim 0.06$), and the interfacial shear strength required to be large ($\tau \sim 45$ MPa)[281]. Finally, it was desirable that the coating wear rate should be as low as possible. An Archard-type wear model[282] would suggest that the coating should be as hard as possible. However, hard coatings have large elastic moduli, which are undesirable for this type of application since (a) large indentation moduli coatings can have large intrinsic stresses, and

(b) large moduli coatings tend to wear by fracture due to columnar morphologies. An alternative method to achieve low wear rates is to avoid wear by columnar fracture of the coating during sliding contact, engineer the coating to be slightly harder than its counterface, and use a coating that establishes a stable velocity accommodation mode (VAM) in the tribological contact.

Although TiC/a-C has a low indentation modulus (110 GPa), it can develop large intrinsic stresses during deposition since it does not have a columnar morphology, and as with sputter-deposited coatings, the magnitude of the intrinsic stress increases with coating thickness. It was found that a ~1 μm TiC/a-C coating had a compressive stress of ~1.2 GPa, a hardness of 8 GPa slightly larger than that of the steel rib face (~7 GPa), and a TiC/a-C/steel interface that displays an excellent VAM through the creation of a relatively thick, and durable graphitic transfer layer in dry and partially lubricated sliding contact.[281]

In a demanding field test where standard tapered roller bearings were able to achieve at most 1 or 2 landings, bearings with the TiC/a-C coating applied to the roller ends were able to exceed the target of 50 landings. The coating was able to deliver the desirable tribological performance because of its ability to inhibit scuffing through the formation of a thick and durable graphitic velocity accommodation layer, its low friction coefficient against steel, the absence of columnar fracture-type wear, and its ability to withstand large shear stresses at the roller end/rib face.

2. Oil-out protection for rotorcraft bearings and gears

A sudden loss of lubrication (oil-out) in rotorcraft gearboxes produces an increase of frictional forces and a rapid temperature rise of meshing components leading to closures of radial clearances and mechanical seizures of bearings and gears[283]. One of the strategies that is being pursued to retard temperature rise in gearboxes after a sudden loss of lubrication is

the use of tribological coatings. Unlike the sliding contact described in the previous example, bearings and gears in rotorcraft gearboxes function under rolling and mixed mode (i.e., rolling/sliding) contact with high Hertzian contact stresses. The desirable functionality of a coating to provide oil-out protection to rotorcraft bearings and gears is to reduce the frictional heating of contacting surfaces after loss of lubrication, while remaining intact during normal operation. Meshing of gear teeth, roller/cage, and roller end/rib face contacts are sources of large heat generation after an oil-out occurrence. Hence a tribological coating that is mechanically compatible with the steel components ($Y \leq 210$ GPa), with greater hardness ($H > 7$ GPa), a low deposition temperature ($T < 180$ ℃), and a small friction coefficient is a desirable candidate for bearings and gears in these applications. A survey of the literature indicates that the family of DLC coatings can satisfy these requirements.[284] Specifically, a tungsten-containing, amorphous hydrocarbon (WC/a-C:H) coating appears to be well-suited to the above coating requirements.

Similar to TiC/a-C, WC/a-C:H is a nanolaminate consisting of nanocrystalline WC precipitates in an amorphous hydrocarbon matrix, and is commonly deposited by closed field unbalanced MS. First developed by Dimigen *et al.* [285], typical WC/a-C:H coatings utilize a thin Cr layer to provide a metallurgical bond to steel, can have thicknesses of ~5 μm, are hard ($H \sim 12$ GPa), and have an indentation modulus of Y' ~ 156 GPa. A ~2.8 μm thick WC/a-C:H coating was reported to have a compressive intrinsic stress of $\sigma \sim 1.5$ GPa, and a relatively low dry friction coefficient against steel after run-in (μ ~ 0.2)[281]. Although WC/a-C:H functions very well as a wear-resistant coating in many applications, it sometimes cannot withstand the rigors of rolling and mixed mode contact under high Hertzian contact stresses. For example, Figure 25 is a cross-sectional TEM micrograph of a WC/a-C:H coating on a roller taken from a bearing after experiencing about 20 million revolutions in boundary lubrication and at 1.5 times rated load[286]. The figure shows an uneven fracture-type wear that originated in the ~150

nm size columns, which transformed the coating into an abrasive surface. The roughened coating surface abrasively removed the active profile of the bearing raceways and generated high local contact stresses, eventually leading to an infantile failure of the bearing.

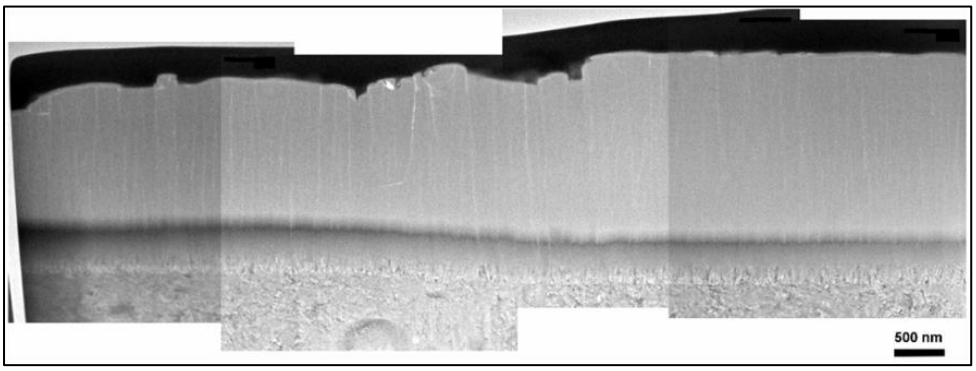

Figure 25: Cross-sectional TEM micrograph of a WC/a-C:H coating on a roller from a bearing after experiencing about 20 million revolutions in boundary lubrication and at 1.5 times rated load.

To enable the WC/a-C:H coating to withstand high cycle contact stresses, it was necessary to eliminate the columnar growth morphology. After much effort, deposition parameters were optimized that accomplished this task. Due to the absence of the columnar morphology, a maximum coating thickness of about 1 μm was required to maintain an intrinsic compressive stress less than ~1.2 GPa. Bearings with the optimized WC/a-C:H coating applied to the rolling elements are reported to have significantly longer fatigue lives in debris-containing and thin-film lubrication environments and are highly resistant to other forms of wear[287]

The tribological performance of the non-columnar WC/a-C:H coating in mixed mode contact was evaluated by Mahmoudi *et al.*[288] Figure 26 displays the Stress Cycle to Failure (S/n) performance of the coating in boundary layer lubrication and with a 2% slide to roll ratio. The open symbols denote run-outs (i.e., no failures) while the filled symbols represent the loss of coating, and the dashed line represents the estimated S/n failure criteria. Under

these test conditions, the optimized WC/a-C:H coating was able to withstand high cycle Hertzian stresses of over 2 GPa without failure.

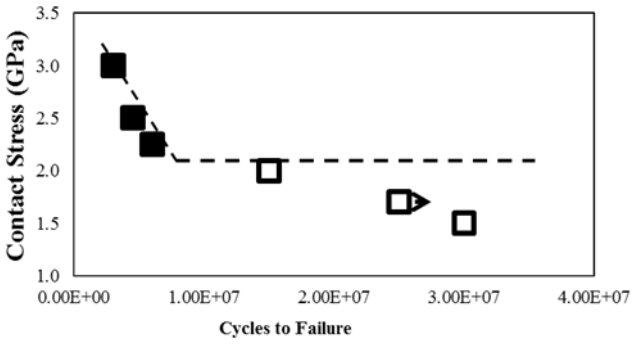

Figure 26: Stress to Cycle to Failure (S/n) performance of an optimized WC/a-C:H coating in boundary layer lubrication and a 2% slide to roll ratio. The open symbols denote run-outs (i.e., no failures) while the filled symbols represent the loss of coating, and the dashed line represents the estimated S/n failure criteria.

A WC/a-C:H coating with a non-columnar morphology that is able to withstand the high cycle Hertzian contact stresses of bearings and gears during normal operation, should therefore be able to reduce the frictional heating originating at the roller/cage, roller/rib face, and gear teeth contact during periods of loss of lubricant.

3. Ball bearings and articulating joints in space platforms

Mechanical components on space platforms normally operate their entire lifetime using a single charge of lubricant, where typical lubricant quantities are in the milligram range.[289] The lubricant films are typically thin and permit extensive contact between the mating metal surfaces. Additionally, the interaction of energetic atomic oxygen in low earth orbit (LEO) promotes a hardening of the lubricant through an oxidation-polymerization process[290] that in turn intensifies the contact between the mating metal surfaces. Without normal atmospheric oxygen, contacting asperities can easily fuse or weld together, then as the

surfaces move against each other, the welded asperities break away and form debris particles that can damage the mechanical systems. In these situations, raceways of ball bearings that are in continuous operation become severely damaged, and the bearings may not achieve their designed lifetimes. Ball bearings that undergo oscillatory motion in these environments can develop worn grooves on the raceways that are geometrically spaced with the balls. This type of wear is known as false brinelling[279], and can also lead to premature failures of the bearings. In articulating joints where linear or rotational sliding occurs, poor lubrication conditions greatly elevate the risk of fretting type wear and galling. A representation of the metal-metal contact that can ensue between balls and bearing raceways in a poorly lubricated environment is shown in Figure 27.[291]

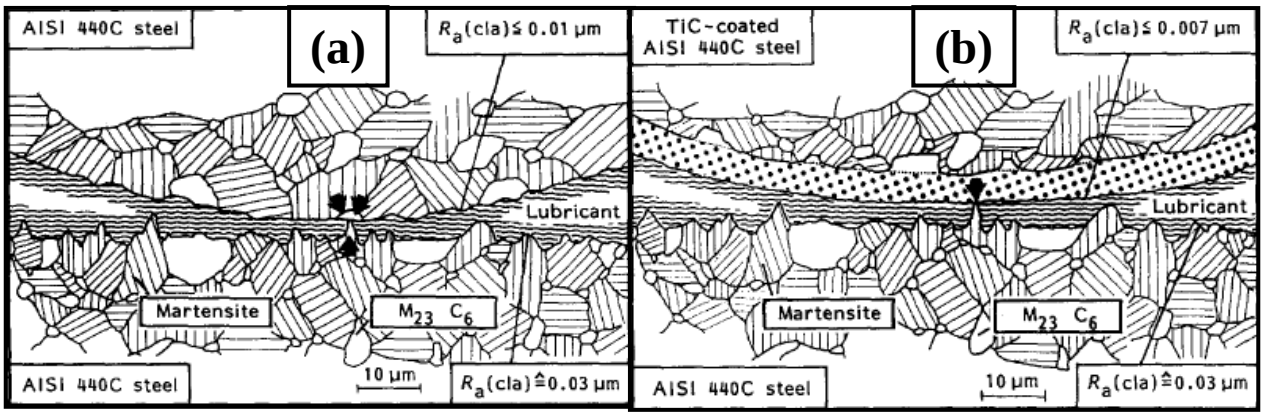

Figure 27: (a) Representation of metal-metal contact between a ball and raceway of a 440C ball bearing in a depleted lubrication condition. (b) Representation of the separation between metal-metal contact that a TiC-coated ball provides in the same depleted lubrication condition.[291] Reprinted with permission from Tribol. Int. 23, 129 (1990). Copyright 1990 Butterworth-Heinemann Ltd.

An approach that has been adopted to address the limited lubrication environment of systems in space platforms is to inhibit metal-metal contact through the use of a tribological coating. In the late 1970's, Hintermann *et al.*[292] reported on the development of a process to apply titanium carbide (TiC) to 440C bearing balls by CVD. The deposition occurred in a

reactor at 900 – 1050 °C, and the growth rate was about 1 $\mu m \cdot \mathrm{hr}^{-1}$.[293] The chemical reaction was

$$TiCl_4(g) + CH_4(g) \xrightarrow{900-1050\,^{\circ}\mathrm{C}} TiC(s) + 4HCl(g)$$

During the duration of a 4 μm deposition, diffusion of the steel into the coating occurred resulting in a metallurgical bonding and a progressive transition of physical and mechanical properties from the steel into the coating.

Because of the high deposition temperatures, a significant distortion and tempering of the 440C balls also took place. Therefore, after deposition it was necessary to retemper the 440C and polish the coated balls to the desired smoothness and sphericity values. After polishing, the surface roughness of the TiC was $R_a < 0.007$ μm. The difference in the CTE of TiC ($8 \times 10^{-6}\ \mathrm{K}^{-1}$) and 440C ($12 \times 10^{-6}\ \mathrm{K}^{-1}$) created compressive stresses in the as-deposited coatings[291]. The magnitude of the stress was found to depend upon the coating thickness. For example, coatings with a thickness of 3 and 15 μm had stresses of ~2.6 and 3.0 GPa, respectively[294]. Quenching and tempering were not found to significantly affect the intrinsic stress of the TiC on 440C. Although coatings with such large amounts of compressive stress probably could not survive the magnitude of Hertzian contact stresses (~1 GPa) required of rolling element bearings in terrestrial applications, the TiC coatings appear to work well with lightly loaded bearings utilized in the mechanical systems of space platforms.

Figure 27 illustrates the functionality of the TiC coating to separate metal contacts in poorly lubricated environments. The excellent performance of TiC coated balls in a gyro spin axis bearing has been demonstrated by McKee[289]. The review on lubricants in spacecraft[295] reported that the TiC coating is an excellent diffusion barrier and is therefore frequently used

to prevent cold-welding and fretting damage on highly stressed stationary-vibrating contacts in hold-down and release mechanisms and latches on deployables.

E. Key aspects and complementary strategies to tailor intrinsic stress

1. Stress sources

As documented in the previous sections, the stress in polycrystalline and amorphous films evolves in a complex way, being in most cases a balance between multiple, competing stress generation and relaxation mechanisms. It is important to recall that the stress generation is a result of the subsequent atomic rearrangement within the film that is constrained by its attachment to the substrate. If the film is not allowed to change structurally, but maintains its "frozen-in" structure, no stress will develop. Sources of intrinsic (growth) stress are numerous and are related to any strained regions due to microstructural/structural modifications taking place either i) within the film *bulk* (e.g., defect/impurity incorporation at lattice or GB sites, voids, recrystallization, …), ii) at the film/substrate *interface* (lattice-mismatch, intermixing, …) or iii) at the growing film *surface* (adsorption, surface diffusion, …). Dislocation motion as well as diffusion processes can operate to reduce stress in the course of film growth or during subsequent processing.[57] The stress can also evolve due to exposure to environmental media, as illustrated in Sections IV-B and IV-D, or as the result of other extrinsic effects (chemical reaction, precipitation, plastic or creep deformation, etc).

The examples provided throughout this article have shown importance of thermodynamics (miscibility between constitutive elements, chemical ordering, phase stability, phase changes); however, growth kinetics and growth energetics decisively matter in dictating the stress behavior in films obtained from condensation of vapor fluxes (which occurs under non-equilibrium conditions), especially for sputter-deposited films. Correlation between intrinsic

stress and corresponding film microstructure shows that grain size evolution, which also depends on the adatom mobility, can have a significant effect on the resulting film stress.

From these studies, different mechanisms of stress generation and relaxation have been reviewed. The kinetic model presented in Section III-A, though not complete, compares favorably with the measured dependence on the grain size for different types of growth, the dependence on the growth rate in several systems, as well as on the thickness-dependence in patterned films. An important benefit of the model is that it provides a quantitative framework with which to analyze stress evolution under different conditions. It shows how different parameters may interact so that complex behavior may possibly be understood in terms of the underlying physical mechanisms, and provides guidelines to develop stress engineering strategies to control the stress state in functional coatings and nanostructured films. Before addressing some routes to tailor intrinsic stress, let us summarize the possible sources of tensile and compressive stresses.

Tensile stresses set-in upon crystallites coalescence[31,32,136,137] (corresponding to the second stage in the CTC behavior of high-mobility materials growing in a Volmer-Weber mode) when neighboring islands form a GB segment; similarly, attractive forces at column boundaries in columnar films induce tensile stress. For low-mobility materials, this source of tensile stress may be propagated in thicker films, as the arriving atoms grow epitaxially on the already strained film. Any film densification, resulting either from grain growth,[57,130,145] annihilation of excess vacancies,[57] or phase transformation,[41,188] also contributes to tensile stress generation.

Compressive stresses usually appear at the early growth stages, as a result of capillary forces (or surface stress) acting in the surface plane of small islands rigidly bonded to the substrate.[62] The mechanisms at the origin of compressive stress during the late film formation stages (after the film continuity has been reached) are more controversial, but they are

experimental evidences that the magnitude of this compression scales with the GB density. Insertion and trapping of excess atoms into GB, either driven by kinetics[65,140] or entropic[296] effects, reasonably explain much of the experimental findings. However, departure from the morphological equilibrium of the surface profile in the presence of an atomic flux would be also a plausible source of compressive stress build-up.[297] Nonetheless, whole or part of this stress component is relieved once deposition is ceased, depending on adatom mobility. For sputter-deposited film, energetic particle bombardment (atomic peening process)[146,154] is an additional compressive stress-producing mechanism. Lattice distortion produced by entrapment of impurity atoms of a size different from the hosting crystal is also a causative source of compression.

For epitaxial systems, lattice mismatch between deposited material and substrate will induce either compressive or tensile stress, depending on the material combination and respective lattice spacing. Upon cooling or heating (during deposition or subsequent thermal cycling), tensile or compressive thermal stresses will develop. For the simple case of an elemental layer, the thermal stress may be estimated from the difference in CTE between film and substrate.[57,298] It is important to point out that CTE for nanocrystalline films may significantly differ from bulk values.[299]

In the following, we propose new insights to control and optimize the intrinsic stress in polycrystalline films, based either on developing coating synthesis strategies to minimize growth stress (by appropriate choice of the process parameters) or by employing interfacial and/or alloy design to purposely tailor film microstructure (and related stress state). Obviously, appropriate combination of substrate/coating materials (or the use of compensated layers) is, as far as possible, advisable for minimizing thermal stress.

2. Stress engineering strategies

a) Optimizing process parameters

Precise control of the intrinsic stress during thin film deposition requires a subtle and simultaneous manipulation of multiple processing parameters, rendering the task not so straightforward. As discussed above, and highlighted in the kinetic model, substrate temperature T and growth rate R can be manipulated to modify the intrinsic stress. For high-mobility metals, increasing T (or decreasing R) contributes to increase the compressive stress component while, for low-mobility metals, it will result in a tensile stress increase. This trend is generally valid for thermal evaporation and electrodeposition conditions. As a rule of thumb, deposition at T/T_m conditions higher than 0.25-0.3, where T_m is the melting point of the thin film material, will imply recovery processes that can affect both microstructure and stress state (relaxation), at the expense of enhancing thermal stress contribution.

There exist additional processes that operate under bombardment with energetic particles (ions or neutrals), like in MS discharges. In such cases, it is important to remind that for low-mobility (high T_m) metals, increasing the deposition rate favor incorporation and trapping of interstitial-type defects, leading to more compressive stress (see Fig. 10b), an opposite behavior to what is reported for high-mobility (low T_m) evaporated or electrodeposited metals (see Fig. 7a). Increasing the working pressure often results in a change from compressive to tensile stress,[25] as energetic particles will experience more and more collisions with working gas atoms (losing part of their kinetic energy) before reaching the substrate. For MS deposition, the critical pressure, corresponding to the compression-to-tension stress transition (i.e. a net zero stress), depends on the respective mass of the target material and working gas atoms (Ar, Xe, He…), as well as geometry of the deposition chamber.[146] So a proper choice of the sputtering gas can be an efficient way in adjusting the stress state in sputtered films. However, the magnitude of tensile stress is often found to decrease at very high pressures, when the films become porous, due to the collapse of the mechanical properties (elastic

moduli) of the film. Such under-dense films are prone to impurity uptake and internal oxidation upon exposure to ambient atmosphere, so that their stress state can be altered after venting (see Fig. 19). Usually, post-growth oxygen incorporation generates a compressive stress contribution.[146]

Depositions at oblique angles tend to promote tensile stresses,[25,300] as the fraction of intercolumnar voids increases with substrate tilt angles. The increase in surface roughness and self-shadowing effect also contribute to decrease the rate of adatom incorporation at the GB, which lessens the magnitude of the compressive stress component of the intrinsic stress.[300]

b) Interfacial and alloying design

As illustrated in Fig. 11, the interface chemistry plays a decisive role on the nucleation stage of polycrystalline thin films, and consequently on the microstructure (grain size, texture) morphology, and related stress state. Controlling the grain size, either through the use of template layers,[301] surfactant elements,[175] or alloying,[172,178,182] can be advantageously employed as a robust strategy to tailor the intrinsic stress. Films with coarse microstructures are recommended to minimize the contribution of defects trapping at the GB.

The combination of materials with different intrinsic stress in a multilayer geometry is also a possible way to achieve low-stress levels[41,119]. Specifically, one can tune the overall stress state by appropriate choice of the modulation period as well as individual layer thicknesses.[302] Films that remain in an amorphous state, e.g. below a critical thickness[302] or above a certain concentration threshold in the case of alloys,[188] are an interesting class of materials. Under conditions of sufficient mobility, they don't manifest any significant morphological change during growth, so that a steady-state stress is in most cases observed.[34] Therefore, one can take advantage of the disordered isotropic atomic structure to design films with smooth surface and tailored stress levels by frustrating any grain-related stress changes.

Amorphous alloys are used in many applications but their intrinsic stress evolution during growth remains yet little explored.[34,303]

c) Tuning ion energy and ion flux

IBAD can be a clever route to control the stress state in thin films. By applying a bias voltage to the substrate, or by controlling the energy (also ideally the flux) of an independent ion source, the energy of ionized species can be adjustably controlled. Increasing the bias voltage will contribute to increase the compressive stress component due to "atomic peening" through knock-on implantation processes in the growing layer. To initiate this process, the arriving particles must have energies higher than the energy threshold for atomic displacement of the thin film material, E_D. However, it is interesting to operate at relatively high bias voltages (typically > 200-300 V) to promote stress relaxation via "thermal spike" processes.[156,304] Therefore, with increasing bombardment energy, the compressive stress initially increases, goes through a maximum and then decreases. Only a few percent (1-2 %) of very energetic impacts can favorably act as a stress relief source. This effect has been capitalized by growing films using plasma immersion ion implantation (PIII), a technique which has shown to produce low-stress coatings.[305]

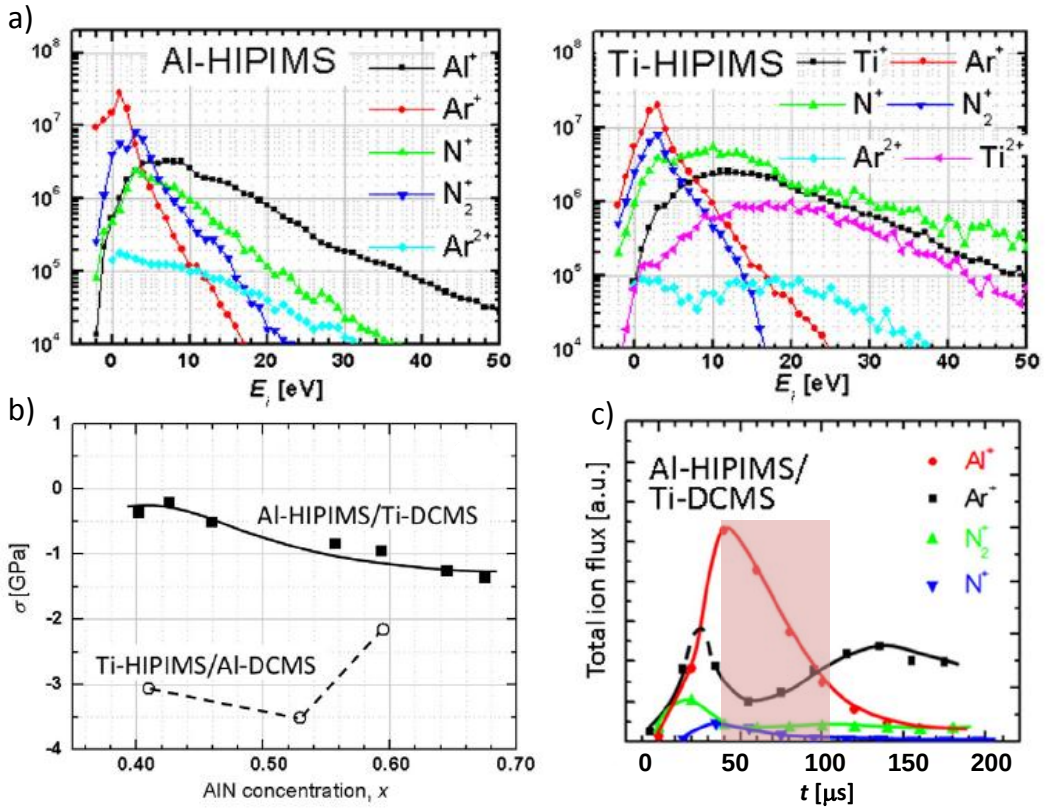

Figure 28: a) Ion energy distribution functions from Al and Ti targets operated in HiPIMS mode at 0.4 Pa under Ar+N_2 gas mixtures (values correspond to the 20-μs highest-target-current-density portions of the 200 μs pulses). b) Residual stress (corrected for thermal stress contribution) in $Ti_{1-x}Al_xN$ films grown using either Al-HiPIMS/Ti-DCMS or Ti-HiPIMS/Al-DCMS configurations. c) Time evolution of the energy-integrated flux of ions species reaching the substrate during the Al-HiPIMS/Ti-DCMS discharge (data are obtained from time-resolved mass spectrometry measurements, see ref. [43]). Reprinted with permission from Surf. Coat. Technol. 257 (2014) 15. Copyright 2014 Elsevier.

Recently, HiPIMS has proved to be a very promising route to tailor thin film microstructures and residual stresss.[43,44,306,307] By synchronizing the bias voltage to the temporal profile of the HiPIMS pulse delivered to the cathode material, it is possible to considerably reduce the compressive stress levels in TiAlN or VAlN films. Data reported in Fig. 28b clearly show that by appropriate choice of the metal-ion flux during hybrid HiPIMS/DCMS film growth, the stress can be tailored accordingly. In the case of TiAlN films, it is conclusive to operate the Al target under HiPIMS conditions, favoring an Al^+-rich incident flux compared to the DCMS case, while the opposite target configuration (Al-DCMS/Ti-HiPIMS) involves a significant fraction of Ti^{2+} ions in addition to Ti^+ ions (see Fig.

28a). As a consequence, these doubly-charged species gain an acceleration energy which is twofold that of Al^+ ions. Greczynski *et al*. have shown that these Ti^{2+} ions are at the origin of larger compressive stress as well as precipitation of wurtzite AlN phase at lower Al content due to larger values of momentum transfer.[43,306] Furthermore, these authors have shown that the compressive stress can be further decreased if one operates by synchronizing the bias voltage to the metal-rich portion (see shaded region in Fig. 28c) of the HiPIMS pulse.[307] In such a way, it is possible to select Al^+ ions as the predominant energetic species reaching the substrate, while synchronizing the bias voltage to the entire HiPIMS pulse implies an Ar^+-rich ion flux. Irradiation with energetic Ar^+ ions generates compressive stress due to creation of residual point defects, especially Ar entrapment at interstitial sites, whilst Al atoms can be primarily incorporated into the metallic lattice sites of the TiAlN film. This metal-ion bombardment also favors an extended solubility of Al in the cubic lattice of ternary nitrides.[44] Thereby, tuning the time domain of ionized fluxes during HiPIMS deposition appears as a perspective approach to produce metastable layers with controllable stress levels. Finally, Cemin *et al.*[308] reported that, contrarily to common expectations, the compressive stress magnitude in Cu HiPIMS films could be significantly reduced despite the energy increase of the bombarding particles from ~20 to ~100 eV. This behavior was attributed to ion-assisted grain growth during HiPIMS deposition which involved a large fraction of Cu^+ ions.

F. Living with cracks

In our daily experience, we often fall victims to unwanted cracks or pernicious fractures. This is especially true for thin films where residual stresses result in film cracks. Film cracking, which is often fatal for film functionality, is usually seen as a nuisance to avoid. However, it is interesting to note that film cracks frequently assume intriguing morphologies: a small sample of arresting film crack patterns is provided in Figure 29 with spiral cracks (a1),

crescent shape zig-zag cracks (a2), festooned circular blisters (b1) and an intriguing parrot ladder blister network interspersed with floppy nondescript structures (b2). All of these cracks and blisters formed spontaneously in homogeneous films.

Understanding the rationale behind such morpologies is interesting in itself, but there is more: we can build structures with cracks. Controlled crack propagation is widely used as a technological process: as examples we can mention glass cutting and wafer dicing. But these high-tech contemporary processes are by far predated (and in a sense also outperformed) by the craftmanship of paleolithic artisans who could produce such amazing artefacts as 20 cm long, millimeters thick laurel leaf blades out of flintstone by the sole use of conchoidal fracture.

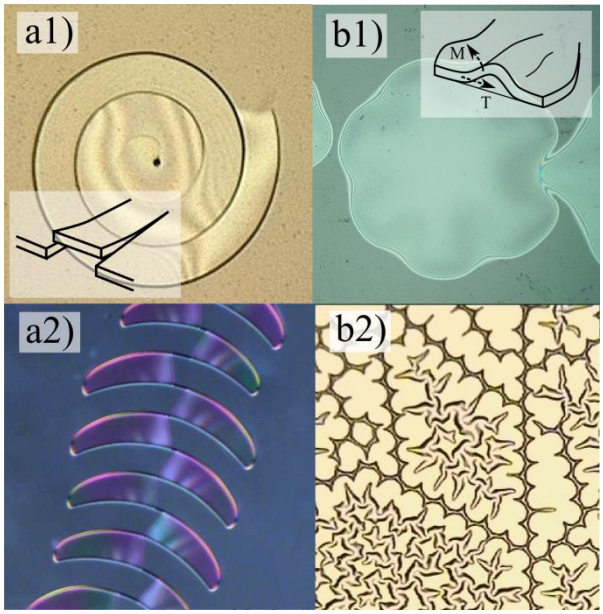

Figure 29: Various film crack patterns: spiral cracks (a1) and crescent shape zig-zag cracks (a2) (courtesy J. Marthelot, ref. [309]), festooned circular blisters (b1) (courtesy A. Benedetto) and blister network (b2) (courtesy J.-Y. Faou, ref. [310]).

It turns out that for thin films, controlled cracking is a relevant elaboration process as well. On rigid substrates, controlled cracking of films has been proposed for mask fabrication, to deposit submillimetric stochastic electrical grid.[311] The stochastic nature of the mask results

from the random process of cracking and the absence of periodicity produces interesting optical properties. In this case, no film delamination should occur, but only sharp through cracks: wet deposition of the colloidal film material and carefully controlled drying makes it possible to obtain the clean sharp crack edges and flat crack bottoms eminently suitable for subsequent metal deposition.

Another area where controlled film cracking is desirable is flexible electronics. Large deformations of a metal coating deposited on a compliant substrate can be obtained if triangular crack structures form, allowing out of plane torsion of the resulting ligaments with no further film rupture during stretching[312]. This mode is essentially an excursion from planar into more 3D deformation. The strategy can be developed further and in many cases, partial release of the thin film from the substrate (i.e., controlled interfacial cracking or delamination) is required. The film then assumes the form of a network of compliant straps that similarly allows formation of large substrate strains without unwanted film rupture[313].

In this last example, the architecture of the coating is defined by lithographic processes but we could consider carefully controlled cracking, as in the previous example. In fact, film cracking may emerge as a manufacturing tool for the fabrication of coatings with advanced architectures[314].

Can we thus think about a design with cracks? To meet this challenge, the control of crack propagation is vital. Unfortunately, it appears to be the second most difficult problem in the field of mechanics of materials, as we also know from our daily experience where getting a crack to go along a precisely defined path seems a difficult, sometimes impossible, task. Of course, there are physical laws behind film cracking, as the regularity of the patterns in Figure 29 suggests. And even though our understanding of these laws is incomplete, in this section, we will illustrate some of the fundamental ideas around film cracking.

1. Concerted film cracking

In a film, some elastic energy is stored, amounting to $e = h\sigma^2/2E$ where σ is the film stress, E the biaxial modulus, and h the film thickness. Consider one single through crack: since the film is constrained by the substrate, elastic energy is released in a region of size h on each side, and the crack can propagate if $2e > G_c$ (condition 1) where G_c is the film fracture energy.

In the inorganic sol-gel films[309] of Figure 28a the film thickness is such that condition (1) is not obeyed: one single crack cannot propagate. However, if two cracks propagate one along the other at separation W then the energy released is much larger as it now involves the full delamination width W. It is given by $We = W\Gamma + 2h\ G_c$ so that $e = \Gamma + 2(h/W)\ G_c$ (condition 2) where Γ is the interfacial rupture energy. A more in-depth analysis shows that $h/W \approx 0.04$.[315] From this low value, we find that if film adhesion Γ is moderate, condition 2 is indeed much less stringent than condition 1. Moreover, one can show that the elastic interaction between the two cracks is stabilizing. If they stray apart, the interaction brings them back, if they get closer, they are driven apart. As a result a stable concerted propagation is possible.

Due to the symmetry of the equi-biaxial stress state, the spiral morphology shown in Figure 28-a1 results from the propagation of the crack in interaction with itself, at a fixed separation W. In the zig-zag/crescent morphology a2, the crack interacts with itself as well, but when it comes to the end of a preexisting leg, it strays away to fold back onto itself. This behavior points to more subtle effects such as instabilities and bifurcations – the reason why it chose this direction can be better understood from some of the effects presented in the next section, namely the telephone cord buckle and related morphologies.

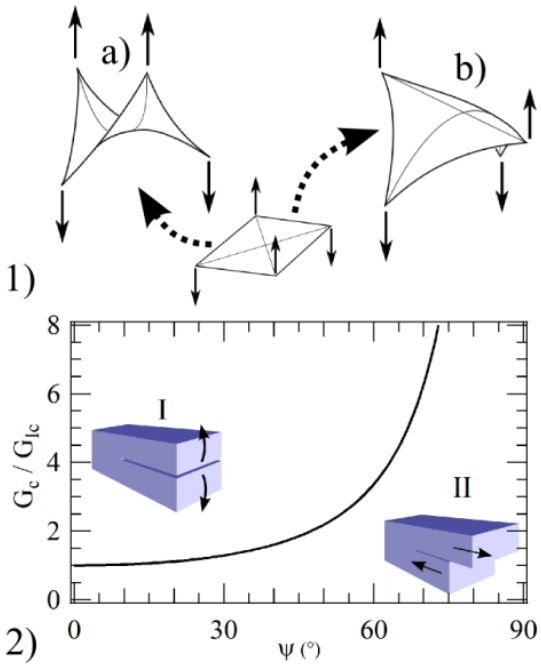

Figure 30: Complex buckle morphologies such as the ubiquitous telephone cord couple non linear plate mechanics (1), and the mode mixity dependence of interfacial fracture energy: shown here (2) is the dependence of interfacial rupture energy upon the ratio of shear to normal loading at the crack tip as quantified by the mode mixity angle η (after ref. [316]).

2. Film instabilities, festoons and branches

In the buckling delamination of compressively stressed films, as for the zig-zag concerted crack(s), the usual telephone cord and related morphologies (such as the parrot ladder - Figure 29-b2) all break the original axial symmetry.

For buckles (also called blisters) the key ingredients are twofold. First, we have to take into account the geometrical nonlinearities of plate mechanics. As a simple example of this first element of complexity, let us consider a square sheet of cardboard which is pulled apart by diagonally opposite corners (Figure 30). Contrary to expectations, the deformed state is not the symmetric shape shown in Fig. 30-1a but one of two possible configurations where the full curvature is located along one single diagonal (Figure 30-1b). This arbitrary choice of one state, out of two, signals bifurcation. But plate nonlinearities by themselves do not lead to the observed buckle morphologies. Therefore, a second element of complexity needed to

understand thin film buckles lies in the physics of the interface. When the film buckles, the interface is loaded both by the *opening moment M* due to the buckle (Figure 29-b1 inset) which pries the interface open, and the *traction T* from the partially relaxed film within the buckle, which shears the interface. The ratio between these two types of loading (quantified by the mode mixity angle η) depends upon the plate conformation, and it strongly affects the actual interfacial energy of rupture (Figure 30-2)[316]. Large shear significantly increases the rupture energy, effectively building up a pinning point. As a result, it is the coupling between plate nonlinearities and loading dependent rupture energy which gives rise to the diverse morphologies of thin film buckles.

With such a high degree of complexity, only the simplest geometries can be tackled analytically. The axi-symmetric case, i.e., the periodic destabilization of a circular blister has been calculated by Hutchinson *et al*.[317] This morphology has actually been observed (Figure 29-b1), although it is very infrequent in practice. For more complex (and more usual) morphologies, such as telephone cords and others (Figure 29-b2), one has to resort to numerical calculations. In this direction, interesting results connecting the period of the telephone cord buckles and interfacial rupture energy, or predicting branching conditions have been recently published.[310,318]

In summary, our improving ability to understand the mechanisms behind film cracking may empower crack-based fabrication processes for architectured films with advanced properties. Of course, there is still a long way to go. As with all architectured systems, one of the limits is the often imperfect match between the desired structures (when we can predict them, of course) and what is feasible. In this respect, as a final word of caution, we should stress that what has been discussed here is only crack propagation, i.e., the extension process of a preexisting crack. For architectured thin film manufacture, one would also need to control

where a crack will originate, thus calling upon *the* most difficult problem in the field of materials science: crack initiation.

V. Conclusions and outlooks

The last decade has seen remarkable progress in the understanding of stress evolution during growth and processing of thin film materials and coatings. This has been driven by the development and emergence of new evaluation methods and gaining insight in the underlying stress mechanisms. Characterization methods, such as wafer curvature and XRD, can be used *in operando* and in real-time, making it possible to achieve a fine tuning and control of the stress level for the design of novel nanostructured materials and functional coatings with enhanced performance and extended durability. Using state-of-the-art X-ray beam synchrotron facilities, location and depth-sensing of the microstructural attributes in terms of grain size, grain shape, phases, texture and residual stress profiles have become possible, with spatial resolution down to 50 nm, opening important avenues in the assessment of stress in coatings with complex microstructures and architectures, such as graded composite layers, multilayered systems, multicomponent and multiphase thin film materials.

Recent experimental findings, supported by analytical models and atomic-scale simulations, have shown the importance of grain boundaries and deposition flux in governing the intrinsic stress build-up and relaxation processes during thin film growth. While energetic particle bombardment often results in the development of compressive residual stress, controlling the ionization degree of film-forming species and temporal profile of the particle flux may be advantageously employed to mitigate and tailor the intrinsic stress in specific films and coating systems.

Besides the energetic control of the film growth through temperature and ion bombardment as well as interfacial engineering (to ensure good adhesion) and post-deposition

stress relaxation (e.g., annealing), complementary approaches to mitigate, control and manage stress are related to specific film and coating architectures; this includes the use of stressors in microelectronics and micro/nanosystems, use of new and novel coating materials (metallic glass films, hybrid organic/inorganic films), and the novel multifunctional approach consisting of implementing and optimizing both optical and thermo-mechanical (stress, component curvature, CTE) properties in optical coatings and other areas.

One of the key elements in further progress to manage stress relies on our understanding of the relationship between stress and mechanical instabilities, such as buckling or film cracking as a consequence of the stored energy dissipation. This issue clearly calls for in-depth investigations of propagation of preexisting cracks and, particularly, crack initiation, both related to the assessment of toughness. Such consideration opens up new avenues for both experimental as well as modeling and simulation studies, including assessment and control of the stress depth profiles, and crack-based fabrication processes for architectured films and coatings with advanced properties. These challenges could be used as strain engineering routes to develop nanoscale systems with innovative device-level functionalities through a careful control of the mechanical deformations and applied stresses, such as flexible, stretchable and shape adaptive devices based on atomically-thin materials (graphene, transition metal dichalcogenide monolayers, Si nano-membranes) or coatings on polymeric substrates.

Acknowledgements

The authors wish to acknowledge Dr. Jonathan Colin and Clarisse Furgeaud, University of Poitiers, and Dr. Rostislav Daniel, Montanuniversität Leoben, for their respective contribution to some of the presented work. MS would like to thank Prof. Edoardo Bemporad

(Roma TRE University) and Prof. Alexander M. Korsunsky (University of Oxford) for the extremely useful scientific discussions on residual stress depth profiling by FIB-DIC.

The work of EC was supported by the U.S. Department of Energy, Office of Science, Basic Energy Sciences, under Award # DE-SC0008799 and the NSF-DMR under Award #1602491. MS's work has received research funding from the European Union, within the large collaborative project OYSTER, Grant Agreement n. 760827. Most of FIB activities were carried out at the "Inter-Departmental Laboratory of Electron Microscopy" (LIME), University ROMA TRE (http://www.lime.uniroma3.it). GBT recognizes the support of the Army Research Office, grant W911NF1310436, Dr. Michael Bakas program manager. Examples of the results from Polytechnique Montréal have been obtained from the work supported by the Natural Sciences and Engineering Research Council (NSERC) of Canada through numerous university-industry research partnership grants, most recently the NSERC Multisectorial Industrial Research Chair in Coatings and Surface Engineering.

Finally, the authors particularly acknowledge the support of the two cooperating organizations, namely the Society of Vacuum Coaters (SVC), and the Advanced Surface Engineering Division (ASED) of the American Vacuum Society (AVS).

Appendix: list of abbreviations

ALD	atomic layer deposition
APT	atom probe tomography
AR	anti-reflective
ASED	Advanced Surface Engineering Division
AVS	American Vacuum Society
BEM	boundary element method
BMG	bulk metal glasses
BOPET	biaxially oriented polyethylene terephthalate
CAD	cathodic arc deposition
CCD	charge-coupled device
CMOS	complementary metal oxide semiconductor
CTC	compressive-tensile-compressive
CTE	coefficient of thermal expansion
CVD	chemical vapor deposition
DCMS	direct current magnetron sputtering
DIC	digital image correlation
DIBS	dual ion beam sputtering
DLC	Diamond-like carbon
EBSD	electron backscattered diffraction
EBE	electron beam evaporation
FE	finite element
FET	field effect transistor
FIB	focused ion beam
FWHM	full width at half maximum
GB	grain boundary
GIXRD	glancing-incidence x-ray diffraction
HiPIMS	high-power impulse magnetron sputtering
IBA-CVD	ion beam assisted chemical vapor deposition
IBAD	ion beam assisted deposition
IBS	ion beam sputtering
ILR	ion beam layer removal
MD	molecular dynamics

MEMS	micro -electro-mechanical systems
MOSS	multiple-beam optical stress sensor
MS	magnetron sputtering
NEMS	nano-electro-mechanical systems
OC	optical coating
OIF	optical interference filters
PC	polycarbonate
PECVD	plasma enhanced chemical vapor deposition
PET	polyethylene terephthalate
PMMA	polymethyl methacrylate
PVD	physical vapor deposition
SDRS	surface differential reflectance spectroscopy
SEM	scanning electron microscopy
SOI	Silicon on insulator
SVC	Society of vacuum coaters
SZM	Structure zone model
TEM	transmission electron microscopy
UHV	ultrahigh vacuum
TSV	Trough Silicon Vias
VAM	velocity accommodation mode
XRD	X-ray diffraction
XRR	X-ray reflection

Figure Captions

Figure 1: (Color online) a) Schematic showing the distribution of stress throughout the thickness of a film on a substrate. b) Evolution of stress-thickness during electron-beam deposition of Ag on SiO_2. The slope of the line from the origin to the solid circle at h_f is proportional to the average stress. The slope of the tangent line is proportional to the incremental stress. c) Evolution of the stress-thickness when the deposition is terminated.

Figure 2: (Color online) A schematic view of position-resolved X-ray nanodiffraction experiment carried out in transmission diffraction geometry on CrN coating with a thickness ξ deposited on Si(100) substrate prepared as lamella with a thickness *e*. The sample is moved along the *z* axis with a step of the X-ray beam size and the diffraction data are collected using a CCD detector. The beam is aligned parallel to the interface using the φ axis movement. A CrN *hkl* Debye–Scherrer ring represents diffraction from CrN crystallites for which the diffraction vectors $\boldsymbol{Q}_{\theta\delta}^{hkl}$ are located on a bold line representing schematically Debye-Scherrer ring depicted in the stereographic projection in the top left. The orientation of the diffraction vector can be specified by angles θ, ψ and δ. Reprinted with permission from Scripta Mater. 67, 748 (2012). Copyright 2012 Elsevier.

Figure 3: (Color online) Schematic representation of the FIB-DIC method (ring-core) for residual stress assessment at the micro scale. (a) SEM image acquired before FIB milling and definition of a grid of markers, (b) FIB incremental milling and acquisition of one (or more) SEM images after each milling step, (c) DIC to map relaxation strain and (d) extraction of the relaxation strain as a function of milling depth. (e-f) the typical size of the milled trench can vary between 1 and 20 µm.

Figure 4: (Color online) Synthetic description of the main experimental and modeling issues related to FIB-DIC residual stress measurement techniques

Figure 5: (Color online) Complementary results from X-ray nanodiffraction and FIB-DIC analyses of residual stresses in 3µm thick CrN thin film sputtered in steps using three bias voltages of −40, −120, −80 V (a). A FIB incremental milling of a micro-pillar (b) using a current of 48 pA resulted in a relaxation of the strain profile (c), which was used to determine

the FIB-DIC stress depth profile (d). For comparison, a stress profile evaluated from X-ray nanodiffraction with a sampling step of 15 nm is presented. Results presented here demonstrate that both nanodiffraction and FIB-DIC profiling techniques have become robust methods for stress profiling with sub-micrometer spatial resolution, for which standardization and industrialization routes could be open

Figure 6: (Color online) Schematic of a section of thin film around a GB illustrating kinetic processes that can influence stress. Reprinted with permission from Thin Solid Films **516**, 1 (2012). Copyright 2012 Elsevier.

Figure 7: (Color online) a) Evolution of stress-thickness in electrodeposited Ni at different growth rates indicated in figure. b) Steady-state stress as a function of growth rate determined from the data in (a). c) Evolution of stress-thickness in evaporated Ni at different growth rates indicated in figure, from Ref. [144].

Figure 8: (Color online) a) Evolution of the stress-thickness during sputter-deposition of Ta films at different Ar working pressure (0.12-0.75 Pa range) and bias voltage (ground, –60 and –190 V). Note that grounded (0 V bias) substrate conditions correspond to lines without mention of bias voltage and values given in parenthesis correspond to the average energy per deposited atom, E_{dep} (see text). b) Evolution of the (compressive) steady-state stress with E_{dep}, determined from the data in (a). Data are taken from Ref. [158].

Figure 9: (Color online) Energy distribution (obtained from SIMTRA calculations) for a) sputtered Ta atoms and b) backscattered Ar at two different Ar working pressures: 0.12 and 0.75 Pa.

Figure 10: (Color online) a) Schematic of the defect creation and annihilation processes due to energetic particle bombardment considered in the stress model. b) Evolution of the steady-state stress of sputtered Ta films with different grain-size versus deposition rate. Symbols refer to experimental data obtained from real-time MOSS and solid lines are fits to the model described in the text.

Figure 11: (Color online) a) Real-time evolution of the film force per unit width during thermal evaporation of Ag films on *a*-SiO_2 and *a*-Ge surfaces at a growth rate R=0.035 nm/s,

graph adapted from Ref. [175]. b) Real-time evolution of the film force per unit width during sputter-deposition of Cu films on *a*-SiO_2, *a*-Ge, *a*-Si, *a*-SiN_x and *a*-C surfaces at a growth rate R= 0.065 nm/s.

Figure 12: (Color online) *In situ* growth response of Ti on Nb. Note the slight positive or tensile stress response of Ti up to 2 nm where upon it transitions to a negative or compressive stress for larger layer thicknesses. This thickness represented the change from bcc to hcp Ti. Figure adapted from Ref. [184].

Figure 13: (Color online) Time-dependent evolution of a) the stress thickness product measured by MOSS, b) the integrated XRD intensity of the (110) peak and c) the surface roughness determined from XRR, during sputter-deposition of $Mo_{1-x}Si_x$ alloys. [188] Reprinted with permission from ACS Appl. Mater. Interfaces 8, 34888 (2016). Copyright 2016 American Chemical Society.

Figure 14: The stress versus annealing behavior under various transformations (a) NiTi film grown at 0.8 mTorr (b) NiTi film grown at 3.2 mTorr and (c) for different compositions of NiTi films.[194] Reprinted with permission from Surf. Coat. Technol. 167, 120 (2003). Copyright 2003 Elsevier.

Figure 15: (Color online) Experimental results collected using cross-sectional X-ray nanodiffraction approach from a 15 μm thick CrN nanocrystalline coating on a Si(100) substrate. (a) SEM image from the film deposited at bias voltages of −40 and −120 V. (b) Diffraction scans collected at different depths reveals the presence of three sublayers with different lattice parameters and crystallographic texture gradient. A map (c) of diffraction intensities for CrN 200 reflection demonstrates smooth transitions of fiber textures across the coating. FWHMs of CrN 111 reflection (d) demonstrate the complex microstructural development with three nucleations zones. Coating depth dependent in-plane residual stresses (e) correlate with the microstructural evolution (a-d) and process conditions.

Figure 16: (Color online) Comparison of measured curvatures induced in Si substrates of different crystallographic orientation by blanket silicon nitride films to calculated values.[213] The Si (011) wafer possesses two independent radii of curvature, where greater curvature is exhibited along the more compliant direction {100} than along {011}. Reprinted with

permission from J. Appl. Phys. 104, 103509 (2008). Copyright 2008 American Institute of Physics.

Figure 17: (Color online) (a) Cross-sectional TEM image of 0.84 μm wide Si_3N_4 stressor feature patterned on a silicon-on-insulator (SOI) layer and (b) comparison of measured out-of-plane strain in the SOI layer as a function of position underneath the stressor feature to mechanical modeling simulations based on the boundary element method (BEM) and an anisotropic edge-force model. [221] Reprinted with permission from Thin Solid Films 530, 85 (2013). Copyright 2013 Elsevier.

Figure 18: (Color online) Stress gradients measured in a $SiC_xN_yH_z$ capped Cu film using GIXRD. (a) Two stress distributions displayed as a function of depth, where the parameters were determined by least-squares fitting of the (b) measured (220) x-ray reflection as a function of incidence angle. [230] Reprinted with permission from Appl. Phys. Lett. 104, 081920 (2014). Copyright 2014 American Institute of Physics.

Figure 19: (Color online) Variation of stress in a typical optical film (SiO_2) during the fabrication process consisting of EBE, degassing, venting, and exposure to the ambient atmosphere (modified after Ref.[234]).

Figure 20: (Color online) Comparison of (optimized) residual stress in low index (SiO_2) and high index (Ta_2O_5) films prepared by different complementary methods including IBAD, pulsed DCMS, DIBS, and PECVD (according to ref. [253]). The values for films prepared by HiPIMS are taken from ref. [254].

Figure 21: (Color online) Variation of the total stress in two types of optical films (inorganic SiO_2 and hybrid silica-like organic-inorganic SiOCH) during the purge with dry nitrogen, venting, and exposure to the ambient atmosphere after ref.[256]).

Figure 22: Spatial distribution of the central wavelength measured in reflection. The filter size is 1.4 mm x 1.4 mm. The vertical scale represents the shift of the filter's central wavelength: the contour lines are spaced at 0.2 nm. The cylinder on the top indicates the size of the light beam: (a) typical 100 GHz bandwidth filter produced with standard process, and (b) a 100 GHz filter fabricated with the ultra-low-stress process.[259] Reprinted with permission from Appl. Opt. 45, 1364 (2006). Copyright 2006 Optical Society of America.

Figure 23: Qualitative composite stress profiles in roll-to-roll web coatings as a result of superposition of web-handling- and sputter-coating-induced stress profiles (example: compressive dielectric sputter coating).

Figure 24: Illustration of a structured interfacial region (interphase) between a plasma-deposited film (here $SiN_{1.3}$ and a polymer substrate (PC). Schematic illustration of the $n(z)$ profile in the interfacial region shows: (i) a crosslinked layer formed by plasma pretreatment attributed mainly to polymer interaction with energetic VUV emitted light, and (ii) a transition layer obtained after $SiN_{1.3}$ deposition (modified after ref. [275]).

Figure 25: Cross-sectional TEM micrograph of a WC/a-C:H coating on a roller from a bearing after experiencing about 20 million revolutions in boundary lubrication and at 1.5 times rated load.

Figure 26: Stress to Cycle to Failure (S/n) performance of an optimized WC/a-C:H coating in boundary layer lubrication and a 2% slide to roll ratio. The open symbols denote run-outs (i.e., no failures) while the filled symbols represent the loss of coating, and the dashed line represent the estimated S/n failure criteria.

Figure 27: (a) Representation of metal-metal contact between a ball and raceway of a 440C ball bearing in a depleted lubrication condition. (b) Representation of the separation between metal-metal contact that a TiC-coated ball provides in the same depleted lubrication condition.[291] Reprinted with permission from Tribol. Int. 23, 129 (1990). Copyright 1990 Butterworth-Heinemann Ltd.

Figure 28: (Color online) a) Ion energy distribution functions from Al and Ti targets operated in HiPIMS mode at 0.4 Pa under $Ar+N_2$ gas mixtures (values correspond to the 20-μs highest-target-current-density portions of the 200 μs long pulses). b) Residual stress (corrected for thermal stress contribution) in $Ti_{1-x}Al_xN$ films grown using either Al-HiPIMS/Ti-DCMS or Ti-HiPIMS/Al-DCMS configurations. c) Time evolution of the energy-integrated flux of ions species reaching the substrate during the Al-HiPIMS/Ti-DCMS discharge (data are obtained from time-resolved mass spectrometry measurements, see ref. [43]). Reprinted with permission from Surf. Coat. Technol. 257 (2014) 15. Copyright 2014 Elsevier.

Figure 29: (Color online) Various film crack patterns: spiral cracks (a1) and crescent shape zig-zag cracks (a2) (courtesy J. Marthelot, ref. [309]), festooned circular blisters (b1) (courtesy A. Benedetto) and blister network (b2) (courtesy J.-Y. Faou, ref. [310]).

Figure 30: (Color online) Complex buckle morphologies such as the ubiquitous telephone cord couple non- linear plate mechanics (1) and the mode mixity dependence of interfacial fracture energy: shown here (2) is the dependence of interfacial rupture energy upon the ratio of shear to normal loading at the crack tip as quantified by the mode mixity angle η (after ref. [316]).

References

[1] M. George, C. Coupeau, J. Colin, and J. Grilhé, Acta Mater. **53**, 411 (2005).

[2] V.M. Marx, F. Toth, A. Wiesinger, J. Berger, C. Kirchlechner, M.J. Cordill, F.D. Fischer, F.G. Rammerstorfer, and G. Dehm, Acta Mater. **89**, 278 (2015).

[3] C. Coupeau, Thin Solid Films **406**, 190 (2002).

[4] M.W. Moon, J.W. Chung, K.R. Lee, K.H. Oh, R. Wang, and A.G. Evans, Acta Mater. **50**, 1219 (2002).

[5] R. Boijoux, G. Parry, J.-Y. Faou, and C. Coupeau, Appl. Phys. Lett. **110**, 141602 (2017).

[6] J.-Y. Faou, S. Grachev, E. Barthel, and G. Parry, Acta Mater. **125**, 524 (2017).

[7] E. Bemporad, M. Sebastiani, F. Casadei, and F. Carassiti, Surf. Coatings Technol. **201**, 7652 (2007).

[8] S. Schmidt, T. Hänninen, J. Wissting, L. Hultman, N. Goebbels, A. Santana, M. Tobler, and H. Högberg, J. Appl. Phys. **121**, 171904 (2017).

[9] S. Djaziri, P.-O. Renault, E. Le Bourhis, P. Goudeau, D. Faurie, G. Geandier, C. Mocuta, and D. Thiaudière, J. Appl. Phys. **116**, 093504 (2014).

[10] Y. Zhang, W.H. Wang, and A.L. Greer, Nat. Mater. **5**, 857 (2006).

[11] L. Martinu, O. Zabeida, and J.E. Klemberg-Sapieha, in *Handb. Thin Film Depos. Technol.*, edited by P.M. Martin, Elsevier (Amsterdam, 2010), pp. 394–467.

[12] D. Vogel, ;E. Auerswald, J. Auersperg, P. Bayat, R.D. Rodriguez, D.R.T. Zahn, S. Rzepka, and B. Michel, Microelectron. Reliab. **54**, 1963 (2014).

[13] H.D. Espinosa, B.C. Prorock, and M. Fischer, J. Mech. Phys. Solids **51**, 47 (2003).

[14] I.A. Blech, J. Appl. Phys. **47**, 1203 (1976).

[15] E. Chason, N. Jadhav, F. Pei, E. Buchovecky, and A. Bower, Prog. Surf. Sci. **88**, 103 (2013).

[16] A.B. Horsfall, J.M.M. Dos Santos, S.M. Soare, N.G. Wright, A.G. O Neill, S.J. Bull, A.J.

Walton, A.M. Gundlach, and J.T.M. Stevenson, Semicond. Sci. Technol. **18**, 992 (2003).

[17] E. Chason, J. Vasquez, F. Pei, N. Jain, and A. Hitt, J. Electron. Mater. 1 (2017).

[18] A. Fluri, A. Marcolongo, V. Roddatis, A. Wokaun, D. Pergolesi, N. Marzari, and T. Lippert, Adv. Sci. **4**, 1700467 (2017).

[19] K.V.L. V Narayanachari, H. Chandrasekar, A. Banerjee, K.B.R. Varma, R. Ranjan, N. Bhat, and S. Raghavan, J. Appl. Phys. **119**, 014106 (2016).

[20] D. Sander, Reports Prog. Phys. **62**, 809 (1999).

[21] D. Sander, Z. Tian, and J. Kirschner, J. Phys. Condens. Matter **21**, 134015 (2009).

[22] M.L. Lee, E.A. Fitzgerald, M.T. Bulsara, M.T. Currie, and A. Lochtefeld, J. Appl. Phys. **97**, 011101 (2005).

[23] E. Chason and P.R. Guduru, J. Appl. Phys. **119**, 191101 (2016).

[24] E.J. Mills, Proc. Roy. Soc. Lon. **26**, 504 (1877).

[25] J.A. Thornton and D.W. Hoffman, Thin Solid Films **171**, 5 (1989).

[26] K.L. Chopra, *Thin Film Phenomena*, McGrow-Hil (New York, 1969).

[27] G. Gore, *The Art of Electro-Metallurgy*, Longmans, (London, 1890).

[28] G.G. Stoney, Proc. Roy. Soc. Lon. **82**, 172 (1909).

[29] E. Klokholm and B.S. Berry, J. Electrochem. Soc. **115**, 823 (1968).

[30] F.M. D'Heurle, Metall. Trans. **1**, 725 (1970).

[31] F.A. Doljack and R.W. Hoffman, Thin Solid Films **12**, 71 (1972).

[32] R. Abermann, R. Kramer, and J. Mäser, Thin Solid Films **52**, 215 (1978).

[33] J.A. Floro, S.J. Hearne, J.A. Hunter, P. Kotula, E. Chason, S.C. Seel, and C. V. Thompson, J. Appl. Phys. **89**, 4886 (2001).

[34] U. Geyer, U. von Hülsen, and H. Kopf, J. Appl. Phys. **83**, 3065 (1998).

[35] R. Koch, Surf. Coatings Technol. **204**, 1973 (2010).

[36] G. Abadias, A. Fillon, J.J.J. Colin, A. Michel, and C. Jaouen, Vacuum **100**, 36 (2014).

[37] D. Depla and B.R. Braeckman, Thin Solid Films **604**, 90 (2016).

[38] M. Kapoor and G.B. Thompson, Curr. Opin. Solid State Mater. Sci. **19**, 138 (2015).

[39] T. Kaub, R. Anthony, and G.B. Thompson, J. Appl. Phys. **122**, 225302 (2017).

[40] B. Fu, W. An, C.H. Turner, and G.B. Thompson, Phys. Rev. Lett. **105**, 1 (2010).

[41] A. Fillon, G. Abadias, A. Michel, C. Jaouen, and P. Villechaise, Phys. Rev. Lett. **104**, 096101 (2010).

[42] F. Cemin, D. Lundin, C. Furgeaud, A. Michel, G. Amiard, T. Minea, and G. Abadias, Sci. Rep. **7**, 1655 (2017).

[43] G. Greczynski, J. Lu, J. Jensen, S. Bolz, W. Kölker, C. Schiffers, O. Lemmer, J.E. Greene, and L. Hultman, Surf. Coatings Technol. **257**, 15 (2014).

[44] G. Greczynski, S. Mráz, H. Ruess, M. Hans, J. Lu, L. Hultman, and J.M. Schneider, J. Appl. Phys. **122**, 025304 (2017).

[45] L. Martinu, J.E. Klemberg-Sapieha, O.M. Kuttel, A. Raveh, and M.R. Wertheimer, J. Vac. Sci. Technol. A **12**, 1360 (1994).

[46] R. Daniel, A. Zeilinger, T. Schöberl, B. Sartory, C. Mitterer, and J. Keckes, J. Appl. Phys. **117**, 235301 (2015).

[47] M. Hÿtch, F. Houdellier, F. Hüe, and E. Snoeck, Nature **453**, 1086 (2008).

[48] F. Ahmed, K. Bayerlein, S.M. Rosiwal, M. Göken, and K. Durst, Acta Mater. **59**, 5422 (2011).

[49] A.J. Wilkinson, G. Meaden, and D.J. Dingley, Ultramicroscopy **106**, 307 (2006).

[50] R. Koch, in *Growth Prop. Ultrathin Ep. Layers*, edited by D.A. King and D.P. Woodruff (Elsevier B.V., 1997), pp. 448–489.

[51] H. Ibach, Surf. Sci. Rep. **35**, 71 (1999).

[52] O.O. Brovko, D.I. Bazhanov, H.L. Meyerheim, D. Sander, V.S. Stepanyuk, and J. Kirschner, Surf. Sci. Rep. **69**, 159 (2014).

[53] A. Fluri, C.W. Schneider, and D. Pergolesi, in *Met. Oxide-Based Thin Film Struct.*, edited by N. Pryds and V. Esposito (Elsevier Inc., 2018), pp. 109–132.

[54] L. Martinu and D. Poitras, J. Vac. Sci. Technol. A **18**, 2619 (2000).

[55] L. Martinu and J.E. Klemberg-Sapieha, in *Opt. Interf. Filters*, edited by N. Kaiser and H. Pulker (Springer-Verlag, Berlin, 2004), pp. 460–489.

[56] G. Strauss, in *Opt. Interf. Filters*, edited by N. Kaiser and H. Pulker, Springer-V (Berlin, 2004), pp. 207–229.

[57] M.F. Doerner and W.D. Nix, Crit. Rev. Solid State Mater. Sci. **14**, 225 (1988).

[58] R. Koch, J. Phys. Condens. Matter **6**, 9519 (1994).

[59] L.B. Freund and S. Suresh, *Thin Film Materials*, Cambridge (2003).

[60] E. Vasco and C. Polop, Phys. Rev. Lett. **119**, 256102 (2017).

[61] Y.-L.L.Y. -L. Shen, S. Suresh, and I.A. Blech, J. Appl. Phys. **80**, 1388 (1996).

[62] R.C. Cammarata, Prog. Surf. Sci. **46**, 1 (1997).

[63] J. Floro and E. Chason, Appl. Phys. Lett. **69**, 3830 (1996).

[64] O. Thomas, P. Müller, P. Gergaud, and S. Labat, J. Appl. Phys. **91**, 2951 (2002).

[65] E. Chason, B.W. Sheldon, L.B. Freund, J. a Floro, and S.J. Hearne, Phys. Rev. Lett. **88**, 156103 (2002).

[66] R. Koch, H. Leonhard, G. Thurner, and R. Abermann, Rev. Sci. Instrum. **61**, 3859 (1990).

[67] C. Friesen and C. V. Thompson, Phys. Rev. Lett **89**, 126103 (2002).

[68] S.G. Mayr and R.S. Averback, Phys. Rev. B **68**, 214105 (2003).

[69] E. Klokholm, Rev. Sci. Instrum. **40**, 1054 (1969).

[70] A.J. Rosakis, R.P. Singh, Y. Tsuji, E. Kolawa, and N.R. Moore Jr., Thin Solid Films **325**, 42 (1998).

[71] O.E. Kongstein, U. Bertocci, and G.R. Stafford, J. Electrochem. Soc. **152**, C116 (2005).

[72] A. Schell-Sorokin and R. Tromp, Phys. Rev. Lett. **64**, 1039 (1990).

[73] J.A. Floro, E. Chason, S.R. Lee, R.D. Twesten, R.Q. Hwang, and L.B. Freund, J. Electron. Mater. **26**, 969 (1997).

[74] Q. Van Overmeere, J.F. Vanhumbeeck, and J. Proost, Rev. Sci. Instrum. **81**, 045106 (2010).

[75] C.-H. Chen, E. Chason, and P.R. Guduru, J. Electrochem. Soc. **164**, A574 (2017).

[76] B.D. Cullity, *Elements of X-Ray Diffraction*, 2nd ed. (Addison Wesley, Reading, MA, 1978).

[77] I.C. Noyan and J.B. Cohen, *Residual Stress Measurement by Diffraction and Interpretation* (Springer-Verlag, New York, 1987).

[78] V. Hauk, *Structural and Residual Stress Analysis by Nondestructive Methods* (Elsevier B.V., Amsterdam, 1997).

[79] M. Birkholz and C. Genzel, in *Thin Film Anal. by X-Ray Scatt.*, edited by M. Birkholz (Wiley-VCH Verlag GmbH, Weinheim, 2006), pp. 239–296.

[80] J. Keckes, J. Appl. Crystallogr. **38**, 311 (2005).

[81] U. Welzel, M. Leoni, and E.J. Mittemeijer, Philos. Mag. **83**, 603 (2003).

[82] A. Reuss, Z. Angew. Math. Mech. **9**, 49 (1929).

[83] W. Voigt, *Lehrbuch Der Kristallphysik* (Teubner, Leipzig, 1928).

[84] H. Neerfeld, Mitt. K.-Wilh.-Inst. Eisenforschg **24**, 61 (1942).

[85] R. Hill, Proc. Phys. Soc. A **65**, 349 (1952).

[86] G. Cornella, S.-H. Lee, W.D. Nix, and J.C. Bravman, Appl. Phys. Lett. **71**, 2949 (1997).

[87] A. Debelle, G. Abadias, A. Michel, and C. Jaouen, Appl. Phys. Lett. **84**, 5034 (2004).

[88] U. Welzel, J. Ligot, P. Lamparter, A.C. Vermeulen, and E.J. Mittemeijer, J. Appl. Crystallogr. **38**, 1 (2005).

[89] C. Genzel, Phys. Status Solidi A **159**, 283 (1997).

[90] B.M. Clemens and J.A. Bain, MRS Bull. **17**, 46 (1992).

[91] P.F. Willemse, B.P. Naughton, and C.A. Verbraak, Mater. Sci. Eng. **56**, 26 (1982).

[92] H.U. Baron and V. Hauk, Zeitschrift Für Met. **79**, 127 (1988).

[93] Y.-W. Kim, J. Moser, I. Petrov, J.E. Greene, and S.M. Rossnagel, J. Vac. Sci. Technol. A **12**, 3169 (1994).

[94] C. Genzel, Mater. Sci. Technol. **21**, 10 (2005).

[95] C. Genzel and M. Klaus, in *Neutrons Synchrotron Radiat. Eng. Mater. Sci. From Fundam. to Appl.*, edited by P. Staron, A. Schreyer, H. Clemens, and S. Mayer (Wiley-VCH, 2017), pp. 161–177.

[96] J. Keckes, M. Bartosik, R. Daniel, C. Mitterer, G. Maier, W. Ecker, J. Vila-Comamala, C. David, S. Schoeder, and M. Burghammer, Scr. Mater. **67**, 748 (2012).

[97] M. Stefenelli, J. Todt, A. Riedl, W. Ecker, T. Müller, R. Daniel, M. Burghammer, and J. Keckes, J. Appl. Crystallogr. **46**, 1378 (2013).

[98] A. Zeilinger, J. Todt, C. Krywka, M. Müller, W. Ecker, B. Sartory, M. Meindlhumer, M. Stefenelli, R. Daniel, C. Mitterer, and J. Keckes, Sci. Rep. **6**, 22670 (2016).

[99] T. Valente, C. Bartuli, M. Sebastiani, and A. Loreto, J. Therm. Spray Technol. **14**, 462 (2005).

[100] K.J.J. Kang, N. Yao, M.Y.Y. He, and A.G.G. Evans, Thin Solid Films **443**, 71 (2003).

[101] N. Sabaté, D. Vogel, A. Gollhardt, J. Keller, C. Cane, I. Gracia, J.R. Morante, and B. Michel, J. Microelectromechanical Syst. **16**, 365 (2007).

[102] A.M. Korsunsky, M. Sebastiani, and E. Bemporad, Mater. Lett. **63**, 1961 (2009).

[103] A.M. Korsunsky, M. Sebastiani, and E. Bemporad, Surf. Coatings Technol. **205**, 2393 (2010).

[104] M. Sebastiani, C. Eberl, E. Bemporad, and G.M. Pharr, Mater. Sci. Eng. A **528**, 7901 (2011).

[105] X. Song, K.B. Yeap, J. Zhu, J. Belnoue, M. Sebastiani, E. Bemporad, K. Zeng, and A.M. Korsunsky, Thin Solid Films **520**, 2073 (2012).

[106] M. Sebastiani, G. Bolelli, L. Lusvarghi, P.P. Bandyopadhyay, and E. Bemporad, Surf. Coatings Technol. **206**, 4872 (2012).

[107] M. Sebastiani, E. Bemporad, G. Melone, L. Rizzi, A.M. Korsunsky, E. Zschech, S. Ogawa, and P.S. Ho, AIP Conf. Proc. **1300**, 120 (2010).

[108] M. Sebastiani, F. Massimi, G. Merlati, and E. Bemporad, Dent. Mater. **31**, 1396 (2015).

[109] B. Winiarski and P.J. Withers, Exp. Mech. **52**, 417 (2012).

[110] M. Krottenthaler, C. Schmid, J. Schaufler, K. Durst, and M. Göken, Surf. Coatings Technol. **215**, 247 (2013).

[111] E. Bemporad, M. Brisotto, L.E. Depero, M. Gelfi, A.M. Korsunsky, A.J.G. Lunt, and M. Sebastiani, Thin Solid Films **572**, 224 (2014).

[112] M. Sebastiani, C. Eberl, E. Bemporad, A.M. Korsunsky, W.D. Nix, and F. Carassiti, Surf. Coatings Technol. **251**, 151 (2014).

[113] C. Mansilla, V. Ocelík, and J.T.M. De Hosson, Microsc. Microanal. **20**, 1625 (2014).

[114] A.J. Lunt, N. Baimpas, E. Salvati, I.P. Dolbnya, T. Sui, S. Ying, H. Zhang, A.K. Kleppe, J. Dluhoš, and A.M. Korsunsky, J. Strain Anal. Eng. Des. **50**, 426 (2015).

[115] N. Baimpas, A.J.G. Lunt, I.P. Dolbnya, J. Dluhos, and A.M. Korsunsky, Carbon N. Y. **79**, 85 (2014).

[116] A.J.G. Lunt and A.M. Korsunsky, Surf. Coatings Technol. **283**, 373 (2015).

[117] M. Sebastiani, K. Johanns, E.G. Herbert, F. Carassiti, and G.M. Pharr, Philos. Mag. **95**, 1928 (2015).

[118] M. Sebastiani, K. Johanns, E.G. Herbert, and G.M. Pharr, Curr. Opin. Solid State Mater. Sci. **19**, 324 (2015).

[119] M. Renzelli, M.Z. Mughal, M. Sebastiani, and E. Bemporad, Mater. Des. **112**, 162 (2016).

[120] A.M. Korsunsky, E. Salvati, T. Sui, A.G.J. Lunta, Z. Mughal, R. Daniel, J. Keckes, E. Bemporad, and M. Sebastiani, Mater. Des. in press (2018).

[121] A.M. Korsunsky, J. Mech. Mater. Struct. **1**, 259 (2006).

[122] E. Salvati, T. Sui, and A.M. Korsunsky, Int. J. Solids Struct. **87**, 61 (2016).

[123] A.M. Korsunsky, J. Guénolé, E. Salvati, T. Sui, M. Mousavi, A. Prakash, and E. Bitzek, Mater. Lett. **185**, 47 (2016).

[124] G.C.A.M. Janssen, M.M. Abdalla, F. van Keulen, B.R. Pujada, and B. van Venrooy, Thin Solid Films **517**, 1858 (2009).

[125] M. Ghidelli, M. Sebastiani, C. Collet, and R. Guillemet, Mater. Des. **106**, 436 (2016).

[126] I. Petrov, P.B.B. Barna, L. Hultman, and J.E.E. Greene, J. Vac. Sci. Technol. A **21**, S117 (2003).

[127] G. Abadias, L. Simonot, J.J. Colin, A. Michel, S. Camelio, and D. Babonneau, Appl. Phys. Lett. **107**, 183105 (2015).

[128] R. Abermann, Vacuum **41**, 1279 (1990).

[129] R. Koch, D. Hu, and A.K. Das, Phys. Rev. Lett. **94**, 146101 (2005).

[130] A.M. Engwall, Z. Rao, and E. Chason, Mater. Des. **110**, 616 (2016).

[131] A.L. Shull and F. Spaepen, J. Appl. Phys. **80**, 6243 (1996).

[132] C. Friesen, S.C. Seel, and C. V. Thompson, J. Appl. Phys. **95**, 1011 (2004).

[133] J. Leib and C. V. Thompson, Phys. Rev. B - Condens. Matter Mater. Phys. **82**, 1 (2010).

[134] H.Z. Yu, J.S. Leib, S.T. Boles, and C. V. Thompson, J. Appl. Phys. **115**, 043521 (2014).

[135] J. Leib, R. Mönig, and C. V. Thompson, Phys. Rev. Lett. **102**, 256101 (2009).

[136] R.W. Hoffman, Thin Solid Films **34**, 185 (1976).

[137] W.D. Nix and B.M. Clemens, J. Mater. Res. **14**, 3467 (1999).

[138] L.B. Freund and E. Chason, J. Appl. Phys. **89**, 4866 (2001).

[139] F. Spaepen, Acta Mater. **48**, 31 (2000).

[140] E. Chason, J.W. Shin, S.J. Hearne, and L.B. Freund, J. Appl. Phys. **111**, (2012).

[141] E. Chason, Thin Solid Films **526**, 1 (2012).

[142] E. Chason, J.W. Shin, C.H. Chen, A.M. Engwall, C.M. Miller, S.J. Hearne, and L.B. Freund, J. Appl. Phys. **115**, (2014).

[143] E. Chason, A.M. Engwall, C.M. Miller, C.H. Chen, A. Bhandari, S.K. Soni, S.J. Hearne, L.B. Freund, and B.W. Sheldon, Scr. Mater. **97**, 33 (2015).

[144] H.Z. Yu and C. V. Thompson, Acta Mater. **67**, 189 (2014).

[145] P. Chaudhari, J. Vac. Sci. Technol. **9**, 520 (1972).

[146] H. Windischmann, Crit. Rev. Solid State Mater. Sci. **17**, 547 (1992).

[147] J.A. Thornton, J. Vac. Sci. Technol. **14**, 164 (1977).

[148] J.A. Thornton, Thin Solid Films **40**, 355 (1977).

[149] D.W. Hoffman and J.A. Thornton, Thin Solid Films **45**, 387 (1977).

[150] D.W. Hoffman and J.A. Thornton, J. Vac. Sci. Technol. **20**, 355 (1982).

[151] J.A. Thornton and D.W. Hoffman, J. Vac. Sci. Technol. A **3**, 576 (1985).

[152] D.W. Hoffman and J.A. Thornton, J. Vac. Sci. Technol. **17**, 380 (1980).

[153] J.A. Thornton, J. Tabock, and D.W.W. Hoffman, Thin Solid Films **64**, 111 (1979).

[154] F.M. D'Heurle and J.M.E. Harper, Thin Solid Films **171**, 81 (1989).

[155] J. Dalla Torre, G.H. Gilmer, D.L. Windt, R. Kalyanaraman, F.H. Baumann, P.L. O'Sullivan, J. Sapjeta, T. Díaz de la Rubia, and M. Djafari Rouhani, J. Appl. Phys. **94**, 263 (2003).

[156] C.A. Davis, Thin Solid Films **226**, 30 (1993).

[157] P. Sigmund, *Topics in Applied Physics: Sputtering by Particle Bombardment I* (Springer-Verlag, Berlin, 1981).

[158] J.J.J.J. Colin, G. Abadias, A. Michel, and C. Jaouen, Acta Mater. **126**, 481 (2017).

[159] K. Van Aeken, S. Mahieu, and D. Depla, J. Phys. D. Appl. Phys. **41**, 205307 (2008).

[160] V. Kouznetsov, K. Macak, J.M. Schneider, U. Helmersson, and I. Petrov, Surf. Coatings Technol. **122**, 290 (1999).

[161] K. Sarakinos, J. Alami, and S. Konstantinidis, Surf. Coatings Technol. **204**, 1661 (2010).

[162] A. Anders, J. Appl. Phys. **121**, 171101 (2017).

[163] D. Depla, S. Mahieu, and J.E. Greene, in *Handb. Depos. Technol. Film. Coatings* (Elsevier Ltd., 2010), pp. 253–296.

[164] J.F. Ziegler, J.P. Biersack, and U. Littmark, *The Stopping and Range of Ions in Matter* (Pergamon Press, New York, 1985).

[165] P. Lucasson, in *Fundam. Asp. Radiat. Damage Met.* (1975), p. 42.

[166] J.-D. Kamminga, T.H. de Keijser, R. Delhez, and E.J. Mittemeijer, J. Appl. Phys. **88**, 6332 (2000).

[167] A. Fillon, G. Abadias, A. Michel, and C. Jaouen, Thin Solid Films **519**, 1655 (2010).

[168] D. Magnfält, G. Abadias, and K. Sarakinos, Appl. Phys. Lett. **103**, 051910 (2013).

[169] G. Abadias and Y.Y. Tse, J. Appl. Phys. **95**, 2414 (2004).

[170] E. Chason, M. Karlson, J.J. Colin, D. Magnfält, K. Sarakinos, and G. Abadias, J. Appl. Phys. **119**, 145307 (2016).

[171] J.J. Colin, PhD Thesis, Université de Poitiers, 2015.

[172] B. Fu and G.B. Thompson, J. Appl. Phys. **108**, 043506 (2010).

[173] G. Abadias, L.E.E. Koutsokeras, P. Guerin, and P. Patsalas, Thin Solid Films **518**, 1532 (2009).

[174] G.H. Gilmer, H. Huang, and C. Roland, Comput. Mater. Sci. **12**, 354 (1998).

[175] D. Flötotto, Z.M. Wang, L.P.H. Jeurgens, E. Bischoff, and E.J. Mittemeijer, J. Appl. Phys. **112**, 043503 (2012).

[176] C. Furgeaud, *Private Communication* (n.d.).

[177] M. Pletea, H. Wendrock, R. Kaltofen, O.G. Schmidt, and R. Koch, J. Phys. Condens. Matter **20**, 255215 (2008).

[178] T.M. Kaub, P. Felfer, J.M. Cairney, and G.B. Thompson, Scr. Mater. **113**, 131 (2016).

[179] C. Furgeaud, L. Simonot, A. Michel, C. Mastail, and G. Abadias, Mater. Des. submitted (n.d.).

[180] H.Z. Yu and C. V Thompson, J. Vac. Sci. Technol. A **33**, 021504 (2015).

[181] X. Zhou, T. Kaub, R.L. Martens, and G.B. Thompson, Thin Solid Films **612**, 29 (2016).

[182] X. Zhou, X.-X. Yu, T. Kaub, R.L. Martens, and G.B. Thompson, Sci. Rep. **6**, 34642 (2016).

[183] B. Fu and G.B. Thompson, Appl. Surf. Sci. **257**, 1500 (2010).

[184] L. Wan, X.-X. Yu, and G.B. Thompson, Acta Mater. **80**, 490 (2014).

[185] L. Wan, X.-X. Yu, X. Zhou, and G. Thompson, J. Appl. Phys. **119**, 245302 (2016).

[186] S. Bajt, D.G. Stearns, and P.A. Kearney, J. Appl. Phys. **90**, 1017 (2001).

[187] S.A. Dregia, R. Banerjee, and H.L. Fraser, Scr. Mater. **39**, 217 (1998).

[188] B. Krause, G. Abadias, A. Michel, P. Wochner, S. Ibrahimkutty, and T. Baumbach, ACS Appl. Mater. Interfaces **8**, 34888 (2016).

[189] A. Mineo, A. Matsuda, T. Kurosu, and M. Kikuchi, Solid State Commun. **13**, 329 (1973).

[190] R.L. Chapman, J.C.C. Fan, H.J. Zeiger, and R.P. Gale, Appl. Phys. Lett. **37**, 292 (1980).

[191] K. Ohdaira and H. Matsumura, J. Cryst. Growth **362**, 149 (2013).

[192] T.P. Leervard Pedersen, J. Kalb, W.K. Njoroge, D. Wamwangi, M. Wuttig, and F. Spaepen, Appl. Phys. Lett. **79**, 3597 (2001).

[193] L.A. Clevenger, A. Mutscheller, J.M.E. Harper, C. Cabral, and K. Barmak, J. Appl. Phys. **72**, 4918 (1992).

[194] Y. Fu, H. Du, and S. Zhang, Surf. Coatings Technol. **167**, 120 (2003).

[195] Y.G. Shen, Y.W. Mai, D.R. McKenzie, Q.C. Zhang, W.D. McFall, and W.E. McBride, J. Appl. Phys. **88**, 1380 (2000).

[196] S.M. Rossnagel, I.C. Noyan, and C. Cabral, J. Vac. Sci. Technol. B Microelectron. Nanom. Struct. **20**, 2047 (2002).

[197] M.J. O'Keefe and J.T. Grant, J. Appl. Phys. **79**, 9134 (1996).

[198] D.A. Young, *Phase Diagram of the Elements* (University of California Press, Berkeley, 1991).

[199] J.-S. Lee, J. Cho, and C.-Y. You, J. Vac. Sci. Technol. A Vacuum, Surfaces, Film. **34**, 021502 (2015).

[200] T. Kaub and G.B. Thompson, J. Appl. Phys. **122**, 085301 (2017).

[201] C.M. Soukoulis and M. Wegener, Nat. Photonics **5**, 523 (2011).

[202] D. Hisamoto, L. W.-C., J. Kedzierski, H. Takeuchi, K. Asano, C. Kuo, E. Anderson, T.-J. King, J. Bokor, and C. Hu, IEEE Trans. Elect. Dev. **47**, 2320 (2000).

[203] P.-C. Wang, G.S. Cargill, I.C. Noyan, and C.K. Hu, J. Appl. Phys. **72**, 1296 (1998).

[204] J. Bardeen and W. Schockley, Phys. Rev. **80**, 72 (1950).

[205] C.S. Smith, Phys. Rev. **94**, 42 (1954).

[206] S.E. Thompson, M. Armstrong, C. Auth, S. Cea, R. Chau, G. Glass, T. Hoffman, J. Klaus, Z. Ma, B. Mcintyre, A. Murthy, B. Obradovic, L. Shifren, S. Sivakumar, S. Tyagi, T. Ghani, K. Mistry, M. Bohr, and Y. El-Mansy, IEEE Electron Device Lett. **25**, 191 (2004).

[207] K.-W. Ang, K.-J. Chui, V. Bliznetsov, C.-H. Tung, A. Du, N. Balasubramanian, G. Samudra, M.F. Li, and Y.-C. Yeo, Appl. Phys. Lett. **86**, 093102 (2005).

[208] S. Ito, H. Namba, T. Hirata, K. Ando, S. Koyama, N. Ikezawa, T. Suzuki, T. Saitoh, and T. Horiuchi, Microelectron. Reliab. **42**, 201 (2002).

[209] S. Timoshenko, J. Opt. Soc. Am. **11**, 233 (1925).

[210] J.F. Nye, *Physical Properties of Crystals*, Oxford Uni (Oxford, 1957).

[211] Q. Ouyang, A. Madan, N. Klymko, J. Li, R. Murphy, H. Wildman, R. Davis, C. Murray, J. Holt, S. Panda, M. Ieong, and C.-Y. Sung, Mater. Res. Soc. Symp. Proc. **913**, 13 (2006).

[212] K. Akarvardar, C.D. Young, M.O. Baykan, I. Ok, T. Ngai, K.-W. Ang, M.P. Rodgers, S. Gausepohl, P. Majhi, C. Hobbs, P.D. Kirsch, and R. Jammy, IEEE Electron Device Lett. **33**, 351 (2012).

[213] C.E. Murray and K.L. Saenger, J. Appl. Phys. **104**, 103509 (2008).

[214] I. DeWolf, H. Norström, and H.E. Maes, J. Appl. Phys. **74**, 4490 (1993).

[215] C. Georgi, M. Hecker, and E. Zschech, J. Appl. Phys. **101**, 123104 (2007).

[216] F. Hüe, M. Hÿtch, H. Bender, F. Houdellier, and A. Claverie, Phys. Rev. Lett. **100**, 156602 (2008).

[217] P.G. Evans, P.P. Rugheimer, M.G. Lagally, C.H. Lee, A. Lal, Y. Xiao, B. Lai, and Z. Cai, J. Appl. Phys. **97**, 103501 (2005).

[218] C.E. Murray, H.-F. Yan, I.C. Noyan, Z. Cai, and B. Lai, J. Appl. Phys. **98**, 013504 (2005).

[219] C.E. Murray, K.L. Saenger, O. Kalenci, S.M. Polvino, I.C. Noyan, B. Lai, and Z. Cai, J. Appl. Phys. **104**, 013530 (2008).

[220] C.E. Murray, J. Appl. Phys. **100**, 103502 (2006).

[221] C.E. Murray, S.M. Polvino, I.C. Noyan, Z. Cai, J. Maser, and M. Holt, Thin Solid Films **530**, 85 (2013).

[222] C.E. Murray, Z. Ren, A. Ying, S.M. Polvino, I.C. Noyan, and Z. Cai, Appl. Phys. Lett. **94**, 063502 (2009).

[223] R. Rosenberg and L. Berenbaum, Appl. Phys. Lett. **12**, 201 (1968).

[224] C.-K. Hu, D. Canaperi, S.T. Chen, L.M. Gignac, B. Herbst, S. Kaldor, M. Krishnan, E. Liniger, D.L. Rath, D. Restaino, R. Rosenberg, J. Rubino, S.-C. Seo, A. Simon, S. Smith, and W.-T. Tseng, in *2004 IEEE Int. Reliab. Phys. Symp. Proc.* (IEEE, 2004), pp. 222–228.

[225] C.-K. Hu, D. Canaperi, S.T. Chen, L.M. Gignac, S. Kaldor, M. Krishnan, S.G. Malhotra, E. Liniger, J.R. Lloyd, D.L. Rath, D. Restaino, R. Rosenberg, J. Rubino, S.-C. Seo, A. Simon, S. Smith, and W.-T. Tseng, Thin Solid Films **504**, 274 (2006).

[226] C.E. Murray, P.R. Besser, C. Witt, and J.L. Jordan-Sweet, Appl. Phys. Lett. **93**, 221901 (2008).

[227] L.G. Parratt, Phys. Rev. **95**, 359 (1954).

[228] H. Dosch, Phys. Rev. **35**, 2137 (1987).

[229] M.F. Doerner and S. Brennan, J. Appl. Phys. **63**, 126 (1988).

[230] C.E. Murray, Appl. Phys. Lett. **104**, 081920 (2014).

[231] C. Genzel, Phys. Status Solidi A **156**, 353 (1996).

[232] N. Kaiser and H. Pulker, editors , *Optical Interference Filters*, Springer (Berlin, 2004).

[233] A. Piegari and F. Flory, editors , *Optical Thin Films and Coatings: From Materials to Applications* (Woodhead Publishing Limited, UK, 2013).

[234] K. Scherer, L. Nouvelot, P. Lacan, and R. Bosmans, Appl. Opt. **35**, 5067 (1996).

[235] E.H. Hirsch, J. Phys. D. Appl. Phys. **13**, 2081 (1980).

[236] L. Martinu, B. Hichwa, and J.E. Klemberg-Sapieha, in *50th Anniversary Book, Society of Vacuum Coaters* (Albuquerque, NM, 2007), pp. 56–69.

[237] C. Mahodaux, H. Rigneault, H. Giovannini, L. Escoubas, and P. Morreti, Microsc. Microanal. Microstruct. **8**, 251 (1997).

[238] J.S. Kim, K.W. Paik, and S.H. Oh, J. Appl. Phys. **86**, 5474 (1999).

[239] R. Thielsch, A. Gatto, and N. Kaiser, Appl. Opt. **41**, 3211 (2002).

[240] E. Çetinörgü, B. Baloukas, O. Zabeida, J.E. Klemberg-Sapieha, and L. Martinu, Appl. Opt. **48**, 4536 (2009).

[241] M. Caron, O. Zabeida, J.E. Klemberg-Sapieha, and L. Martinu, Surf. Coatings Technol. **314**, 131 (2017).

[242] T. Poirié, T. Schmitt, E. Bousser, L. Martinu, and J.-E. Klemberg-Sapieha, Tribol. Int. **109**, 355 (2017).

[243] B.A. Movchan and W.V. Demchishin, Phys. Met. Met. **28**, 83 (1969).

[244] J.A. Thornton, J. Vac. Sci. Technol. A Vacuum, Surfaces, Film. **4**, 3059 (1986).

[245] R. Messier, A.P. Giri, and R.A. Roy, J. Vac. Sci. Technol., A **2**, 500 (1984).

[246] S.M. Rossnagel, J.J. Cuomo, and W.D. Westwood, editors , *Handbook of Plasma Processing Technology* (Noyes Publication, Park Ridge, NJ, 1990).

[247] A. Anders, Thin Solid Films **518**, 4087 (2010).

[248] J.E. Klemberg-Sapieha, L. Martinu, M.R. Wertheimer, P. Günther, R. Schellin, C. Thielemann, and G.M. Sessler, J. Vac. Sci. Technol. A Vacuum, Surfaces, Film. **14**, 2775 (1996).

[249] A. Amassian, R. Vernhes, J.E. Klemberg-Sapieha, P. Desjardins, and L. Martinu, Thin Solid Films **469-470**, 47 (2004).

[250] R. Vernhes, J.E. Klemberg-Sapieha, and L. Martinu, Sensors Actuators B Chem. **185**, 504 (2013).

[251] L. Martinu, A. Raveh, D. Boutard, S. Houle, D. Poitras, N. Vella, and M.R. Wertheimer, Diam. Relat. Mater. **2**, 673 (1993).

[252] J. Houska, J.E. Klemberg-Sapieha, and L. Martinu, Surf. Coatings Technol. **203**, 3770 (2009).

[253] J.E. Klemberg-Sapieha, J. Oberste-Berghaus, L. Martinu, R. Blacker, I. Stevenson, G. Sadkhin, D. Morton, S. McEldowney, R. Klinger, P.J. Martin, N. Court, S. Dligatch, M. Gross, and R.P. Netterfield, Appl. Opt. **43**, 2670 (2004).

[254] M. Hála, R. Vernhes, O. Zabeida, J.-E. Klemberg-Sapieha, and L. Martinu, J. Appl. Phys. **116**, 213302 (2014).

[255] M. Hála, R. Vernhes, O. Zabeida, E. Bousser, J.E. Klemberg-Sapieha, R. Sargent, and L. Martinu, Surf. Coatings Technol. **241**, 33 (2014).

[256] O. Zabeida, R. Vernhes, T. Poirié, S. Chiarotto, K. Scherer, T. Schmitt, V. Marushka, J.E. Klemberg-Sapieha, and L. Martinu, in *Opt. Interf. Coatings* (OSA, Washington, D.C., 2013), p. ThA.4.

[257] T.C. Begou, C. Hecquet, F. Lemarchand, and M. Lequime, in *Opt. Interf. Coatings* (OSA, Washington, D.C., 2013), p. PTE.6.

[258] M.-M. de Denus-Baillargeon, T. Schmitt, S. Larouche, and L. Martinu, Appl. Opt. **53**, 2616 (2014).

[259] G.J. Ockenfuss and R.E. Klinger, Appl. Opt. **45**, 1364 (2006).

[260] N.A. O'Brien, M.J. Cumbo, K.D. Hendrix, R.B. Sargent, and M.K. Tilsch, in *44th Tech. Conf. Proc.* (Society of Vacuum Coaters, New Mexico, 2001), pp. 255–261.

[261] A. Bergeron and R.B. Sargent, *Irreversible Effects of Annealing on Magnetron-Sputtered Tantalum Pentoxide Films, Private Communication* (2008), and S.E. Solberg and B.J. Pond, US Patent 5930046A (1999)

[262] C. Bishop, *Vacuum Deposition onto Webs, Films and Foils*, Elsevier (2015).

[263] D.J. Mcclure, in *Proc. 50th SVC Tech. Conf.* (Louisville, KY, 2007).

[264] D.J. Mcclure, in *Proc. 53rd SVC Tech. Conf.* (Orlando, FL, 2010).

[265] D. Roisum, in *Proc. AIMCAL Web Coat. Handl. Conf. Eur.* (Dresden, 2016).

[266] M. Helgesen, J.E. Carlé, B. Andreasen, M. Hösel, K. Norrman, R. Søndergaard, and F.C. Krebs, Polym. Chem. **3**, 2649 (2012).

[267] T. Neubert and M. Vergöhl, in *Opt. Thin Film. Coatings*, edited by A. Piegari and F. Flory (Woodhead Publishing, 2013), pp. 427–449.

[268] T. Neubert, A. Gaida, W. Huwer, and M. Vergöhl, in *Conf. Proc. Opt. Syst. Des.* (Marseille, France, 2011).

[269] J.S. Lewis and M.S. Weaver, IEEE J. Sel. Top. Quantum Electron. **10**, 45 (2004).

[270] K. Kogler, *Selection of Plastics for Optical Applications* (2016).

[271] P. Munzert, U. Schulz, and N. Kaiser, Surf. Coatings Technol. **174-175**, 1048 (2003).

[272] P. Munzert, U. Schulz, and N. Kaiser, Plasma Process. Polym. **4**, S1036 (2007).

[273] W.-B. Young, Appl. Math. Model. **29**, 955 (2005).

[274] K. Pfeiffer, S. Shestaeva, A. Bingel, P. Munzert, L. Ghazaryan, C. van Helvoirt, W.M.M. Kessels, U.T. Sanli, C. Grévent, G. Schütz, M. Putkonen, I. Buchanan, L. Jensen, D. Ristau, A. Tünnermann, and A. Szeghalmi, Opt. Mater. Express **6**, 660 (2016).

[275] A. Bergeron, J.E. Klemberg-Sapieha, and L. Martinu, J. Vac. Sci. Technol. A **16**, 3227 (1998).

[276] J.E. Klemberg-Sapieha, L. Martinu, N.L.S. Yamasaki, and C.W. Lantman, Thin Solid

Films **476**, 101 (2005).

[277] J.E. Klemberg-Sapieha, D. Poitras, L. Martinu, N.L.S. Yamasaki, and C.W. Lantman, J. Vac. Sci. Technol. A **15**, 985 (1997).

[278] G. Doll, R.D. Evans, and C.R. Ribaudo, in *Surf. Eng. Mater. Sci. III* (Minerals, Metals and Materials Society, TMS, San Francisco, CA, 2005), pp. 153–162.

[279] T.A. Harris and M.N. Kotzalas, editors , *Essential Concepts of Bearing Technology* (Taylor & Francis Group, CRC Press, Boca Raton, FL, 2007).

[280] D.P. Monaghan, D.G. Teer, P.A. Logan, I. Efeoglu, and R.D. Arnell, Surf. Coatings Technol. **60**, 525 (1993).

[281] T.W. Scharf and I.L. Singer, Tribol. Lett. **36**, 43 (2009).

[282] J.F. Archard and W. Hirst, Proc. Roy. Soc. Lon. A **236**, 397 (1956).

[283] G. Gasparini, N. Motta, A. Gabrielli, and D. Colombo, *Gearbox Loss of Lubrication Performance: Myth, Art or Science?* (2014).

[284] A. Erdemir and C. Donnet, J. Phys. D. Appl. Phys. **39**, R311 (2006).

[285] H. Dimigen, H. Hübsch, and R. Memming, Appl. Phys. Lett. **50**, 1056 (1987).

[286] Y.S. Kang, R.D. Evans, and G.L. Doll, in *Proc. STLE/ASME 2008 Int. Jt. Tribol. Conf.* (American Society of Mechanical Engineers, 2008), pp. 745–747.

[287] M. Eckels, M.N. Kotzalas, and G.L. Doll, Tribol. Trans. **56**, 410 (2013).

[288] B. Mahmoudi, C.H. Hager, and G.L. Doll, Surf. Coatings Technol. **283**, 96 (2015).

[289] F.B. Mckee, Surf. Coatings Technol. **33**, 401 (1987).

[290] S.M. Hsu and E.E. Klaus, A S L E Trans. **21**, 201 (1978).

[291] H.J. Boving and H.E. Hintermann, Tribol. Int. **23**, 129 (1990).

[292] Hintermann, H. E., H. Boving, and W. Hänni, Wear **48**, 225 (1978).

[293] H.J. Boving and H.E. Hintermann, Thin Solid Films **153**, 253 (1987).

[294] L. Chollet, H. Boving, and H.E. Hintermann, J. Mater. Energy Syst. **6**, 293 (1985).

[295] H.M. Briscoe, in *Proc. Int. Symp. Spacecr. Mater. Sp. Envrionment* (ESA SP-178, 1982), pp. 27–34.

[296] A. Saedi and M.J. Rost, Nat. Commun. **7**, 10733 (2016).

[297] H.Z. Yu and C. V. Thompson, Appl. Phys. Lett. **104**, 141913 (2014).

[298] W.D. Nix, in *Met. Film. Electron. Opt. Magn. Appl.*, edited by K. Barmak and K. Coffey (Woodhead Publishing Limited, 2014), pp. 353–421.

[299] R. Daniel, D. Holec, M. Bartosik, J. Keckes, and C. Mitterer, Acta Mater. **59**, 6631 (2011).

[300] H.Z. Yu and C. V. Thompson, Acta Mater. **77**, 284 (2014).

[301] D. Magnfält, A. Fillon, R.D. Boyd, U. Helmersson, K. Sarakinos, and G. Abadias, J. Appl. Phys. **119**, 055305 (2016).

[302] Q. Guo, L. Wan, X.-X. Yu, F. Vogel, and G.B. Thomspon, Acta Mater. **132**, 149 (2017).

[303] S. Dina, U. Geyer, and G. v. von Minnigerode, Ann. Phys. **1**, 164 (1992).

[304] M.M.M. Bilek, M. Verdon, L. Ryves, T.W.H. Oates, C.T. Ha, and D.R. McKenzie, Thin Solid Films **482**, 69 (2005).

[305] M.M.M. Bilek and D.R. McKenzie, Surf. Coatings Technol. **200**, 4345 (2006).

[306] G. Greczynski, J. Lu, J. Jensen, I. Petrov, J.E. Greene, S. Bolz, W. Kölker, C. Schiffers, O. Lemmer, and L. Hultman, Thin Solid Films **556**, 87 (2014).

[307] G. Greczynski, J. Lu, J. Jensen, I. Petrov, J.E. Greene, S. Bolz, W. Kölker, C. Schiffers, O. Lemmer, and L. Hultman, J. Vac. Sci. Technol. A **30**, 61504 (2012).

[308] F. Cemin, G. Abadias, T. Minea, C. Furgeaud, F. Brisset, D. Solas, and D. Lundin, Acta Mater. **141**, 120 (2017).

[309] J. Marthelot, B. Roman, J. Bico, J. Teisseire, D. Dalmas, and F. Melo, Phys. Rev. Lett. **113**, 22 (2014).

[310] J.Y. Faou, G. Parry, S. Grachev, and E. Barthel, J. Mech. Phys. Solids **75**, 93 (2015).

[311] G. Zagdoun, B. Nghiem, E. Valentin, and S. Tchakarov, US Patent 8697186 B2 (2014).

[312] S.P. Lacour, D. Chan, S. Wagner, T. Li, and Z. Suo, Appl. Phys. Lett. **88**, 204103 (2006).

[313] D.-H. Kim, J.-H. Ahn, W.M. Choi, H.-S. Kim, T.-H. Kim, J. Song, Y.Y. Huang, Z. Liu, C. Lu, and J.A. Rogers, Science (80-.). **320**, 507 (2008).

[314] M. Kim, D.-J. Kim, D. Ha, and T. Kim, Nanoscale **8**, 9461 (2016).

[315] J. Marthelot, J. Bico, F. Melo, and B. Roman, J. Mech. Phys. Solids **84**, 214 (2015).

[316] J.W. Hutchinson and Z. Suo, Adv. Appl. Mech. **29**, 63 (1992).

[317] J.W. Hutchinson, M.D. Thouless, and E.G. Liniger, Acta Metall. Mater. **40**, 295 (1992).

[318] J.-Y. Faou, G. Parry, S. Grachev, and E. Barthel, Phys. Rev. Lett. **108**, 116102 (2012).